Faculty of Engineering Science, Department of Civil Engineering
Building Physics and Sustainable Design
Kasteelpark Arenberg 40, 3001 Leuven, Belgium

dangxinyuan1994@gmail.com
https://www.kuleuven.be/wieiswie/en/person/00149958
https://orcid.org/0000-0002-0113-4962

Heat and moisture are fundamental forces shaping both the natural and built environments,
yet their interaction remains intricate and nuanced.
Standing on the shoulders of giants,
this research has taken a small step toward deepening our understanding of this dynamic.

Science is never truly complete —
assumptions invite reevaluation,
mechanisms require refinement,
and uncertainties remain worthy of exploration.

I will continue questioning, striving and seeking knowledge as I have been doing.
Moving forward with the same spirit:
to learn as a beginner,
to dream without hesitation,
and to welcome new challenges with an open heart.

Here's to whatever comes next.

Scan for my updates

Researchgate | LinkedIn | Google Scholar

Xinyuan Dang

Quality Assessment of Heat, Air and Moisture (HAM) Models to Predict the Hygrothermal Response of Building Components

December 2025

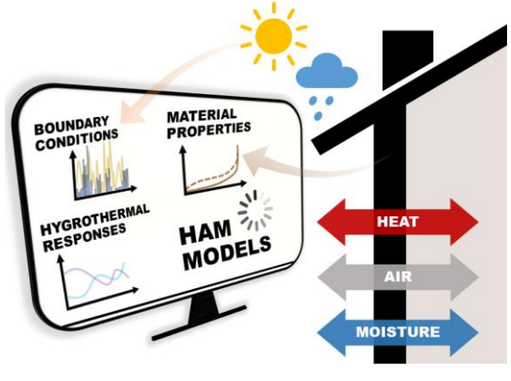
KU LEUVEN

Arenberg Doctoral School
Faculty of Engineering Science

Quality Assessment of Heat, Air and Moisture (HAM) Models to Predict the Hygrothermal Response of Building Components

Xinyuan Dang

Supervisors:
Prof. Staf Roels
Prof. Hans Janssen



Dissertation presented in partial fulfillment of the requirements for
the degree of Doctor of Engineering Science (PhD): Civil Engineering

Knowledge knows no end

QUALITY ASSESSMENT OF HEAT, AIR AND MOISTURE (HAM) MODELS TO PREDICT THE HYGROTHERMAL RESPONSE OF BUILDING COMPONENTS

Xinyuan DANG

Supervisors:

Prof. Staf Roels (KU Leuven, Belgium)
Prof. Hans Janssen (KU Leuven, Belgium)

Members of the Examination Committee:

Prof. Krista De Jonge (Chair; KU Leuven, Belgium)
Prof. Özlem Cizer (KU Leuven, Belgium)
Prof. Shuichi Hokoi (Southeast University, China)
Prof. Evy Vereecken (Secretary; KU Leuven and KIK-IRPA, Belgium)
Prof. Martin Tenpierik (TU Delft, The Netherlands)

Dissertation presented in partial fulfilment of the requirements for the degree of **Doctor of Engineering Science (Civil Engineering)**

© 2025 XINYUAN DANG
Uitgegeven in eigen beheer, XINYUAN DANG, Leuven

Alle rechten voorbehouden. Niets uit deze uitgave mag worden vermenigvuldigd en/of openbaar gemaakt worden door middel van druk, fotokopie, microfilm, elektronisch of op welke andere wijze ook zonder voorafgaandelijke schriftelijke toestemming van de uitgever.

All rights reserved. No part of the publication may be reproduced in any form by print, photoprint, microfilm, electronic or any other means without written permission from the publisher.

Scientific abstract

Accurately predicting the hygrothermal behavior of building components remains a major challenge in building physics. This difficulty stems largely from how simulation tools represent material properties, boundary conditions and related factors. The PhD thesis begins by revisiting the fundamental equations governing heat, air and moisture (HAM) transport, then evaluates the limitations of existing model assessment studies in their scopes, methodologies and benchmarks. To address these issues, the study introduces a stepwise and comprehensive methodology for evaluating the quality of HAM models, particularly WUFI and DELPHIN. Uncertainties related to material properties are examined through a benchmark dataset derived from controlled in-lab experiments. This dataset involves detailed measurements of hygrothermal material properties, boundary conditions, surface transport coefficients and hygrothermal responses. It supports a round robin validation campaign, revealing that variations in the implemented hygric properties can result in significant discrepancies in simulated outcomes. Supplementary comparative simulations further quantify these implementation differences and examine their implications under diverse hygrothermal transport dynamics. The study then shifts focus to boundary conditions, explored through in-situ configurations using real-world climate data. It compares semi-empirical methods for calculating wind-driven rain (WDR) as implemented in WUFI and DELPHIN, uncovering how specific assumptions and simplifications can systematically over- or underestimate WDR loads, resulting in substantial discrepancies in the predicted hygrothermal responses. By integrating theoretical analysis with empirical evidence, the research underscores the risks of relying on default parameters and oversimplified representations. It calls for closer alignment between simulation models and observed reality, concluding with recommendations for enhancing the reliability and robustness of HAM modeling practices.

Popularized summary

Buildings are in constant exchange with their surroundings: heat, air and moisture (HAM) move through walls and roofs, influencing among others their durability and energy efficiency. To predict how building components respond to these environmental changes, numerical HAM models are often used. However, even widely adopted tools can yield deviating results depending on how they are configured. This study examines two prevalent models, WUFI and DELPHIN, and investigates underlying reasons for their differing predictions. A closer look reveals that much of the divergence stems from how each tool processes material data and environmental conditions. To explore these discrepancies, the study integrates data from controlled lab experiments with on-site field monitoring. In the lab, materials are tested under well-defined conditions to create a reference dataset. This enables direct comparison of how each model interprets the same material property data. In the field, the study focuses on how different models estimate wind-driven rain (WDR), a major source of moisture exposures, and finds that even small differences in calculation methods can lead to significant variations in predicted performance. The findings underscore a broader concern: relying too heavily on default settings or simplified assumptions can result in inaccurate predictions. This has practical implications for building design, renovation strategies and long-term resilience. By showing how simulation outcomes depend on implementation strategies, the research calls for closer alignment between modeling results and real-world observations. Ultimately, it offers a path toward improving the reliability and robustness of HAM models.

Nomenclature

English

$\boldsymbol{A}$	capillary absorption coefficient [kg/(m·s$^{0.5}$)] or area [m^2]
$\boldsymbol{C}$	volumetric specific heat capacity [J/(K·m^3)]
$\boldsymbol{c}$	specific heat capacity [J/(kg·K)]
$\boldsymbol{C_T}$	topography coefficient [-]
$\boldsymbol{C_R}$	terrain surface roughness coefficient [-]
$\boldsymbol{D}$	diffusivity [m^2/s, (under the gradient of moisture content)]
$\boldsymbol{F_D}$	rain deposition factor [-]
$\boldsymbol{F_E}$	rain exposure factor [-]
$\boldsymbol{F_L}$	empirical constant [kg·s/(m^3·mm)]
$\boldsymbol{f}$	wind-dependent factor [J/(m^3·K)]
$\boldsymbol{g}$	moisture flux [kg/(m^2·s)]
$\boldsymbol{H}$	enthalpy density [J/m^3]
$\boldsymbol{HF}$	heat flux [J/(m^2·s)]
$\boldsymbol{K}$	permeability [kg/(m·s·Pa)] or [s]
$\boldsymbol{L}$	latent heat [J/kg]
$\boldsymbol{m}$	mass [kg]
$\boldsymbol{O}$	obstruction factor [-]
$\boldsymbol{P}$	pressure [Pa]
$\boldsymbol{q}$	heat flux [J/(m^2·s)]
$\boldsymbol{R}$	rain [L/(m^2·h)] or reduction factor or constant
$\boldsymbol{T}$	temperature [K]
$\boldsymbol{t}$	time [s]
$\boldsymbol{U}$	wind velocity [m/s]
$\boldsymbol{u}$	moisture content by mass [kg/kg] or specific internal energy [J/kg]
$\boldsymbol{W}$	wall factor [-]
$\boldsymbol{w}$	moisture content [kg/m^3]
$\boldsymbol{x}$	distance [m] or water vapor ratio, [kg/kg]
$\boldsymbol{y}$ or $\boldsymbol{z}$	distance [m]

Greek

$\boldsymbol{\alpha}$	surface heat transport coefficient [W/(m^2·K)] or wind-driven rain coefficient [s/m]

$\boldsymbol{\beta}$	surface moisture transport coefficient [kg/(m²·s·Pa)]
Δ	derivative [-]
$\boldsymbol{\delta}$	permeability [kg/(m·s·Pa)] or [s]
$\boldsymbol{\theta}$	temperature [°C] or moisture content [m³/m³] or degree [°]
$\boldsymbol{\kappa}$	wind-driven rain coefficient [s/m]
$\boldsymbol{\lambda}$	thermal conductivity [W/(m·K)]
$\boldsymbol{\mu}$	vapor diffusion resistance factor [-]
$\boldsymbol{\rho}$	density or concentration [kg/m³]
$\boldsymbol{\varphi}$	relative humidity [%]
$\boldsymbol{\Psi}$	porosity [m³/m³]

Subscripts

$\boldsymbol{a}$	air
$\boldsymbol{ab}$	absorption
$\boldsymbol{avg}$	average
$\boldsymbol{c}$	capillary or center
$\boldsymbol{cap}$	capillary saturation
$\boldsymbol{cond}$	conduction
$\boldsymbol{conv}$	convection
$\boldsymbol{de}$	desorption
$\boldsymbol{dry}$	dry
$\boldsymbol{e}$	exterior or edge
$\boldsymbol{eq}$	equivalent
$\boldsymbol{f}$	free
$\boldsymbol{g}$	gas
$\boldsymbol{hor}$	horizontal
$\boldsymbol{i}$	interior
$\boldsymbol{it}$	interface
$\boldsymbol{l}$	liquid water
$\boldsymbol{max}$	maximum
$\boldsymbol{min}$	minimum
$\boldsymbol{rad}$	radiation
$\boldsymbol{ref}$	reference
$\boldsymbol{P25}$	25 % percentile
$\boldsymbol{P75}$	75 % percentile
$\boldsymbol{s}$	surface
$\boldsymbol{se}$	exterior surface
$\boldsymbol{si}$	interior surface
$\boldsymbol{sat}$	saturation
$\boldsymbol{tot}$	total
$\boldsymbol{T}$	under temperature gradient

$\boldsymbol{v}$	water vapor
$\boldsymbol{va}$	water vapor in air
$\boldsymbol{w}$	water or under moisture content gradient
$\boldsymbol{\varphi}$	under relative humidity gradient

Acronyms

CS	calcium silicate board
CFD	computational fluid dynamics
D1	DELPHINI's approach 1 for WDR calculation
EPS	expanded polystyrene
HAM	heat, air and moisture
HB-CB	hot box-cold box (setup/experiment)
HF	heat flux
MB	the main building of TU/e (Eindhoven University of Technology)
MIP	mercury intrusion porosimetry
MM	moisture mass [kg/m^2]
MW	mineral wool
NMR	nuclear magnetic resonance
PVC	polyvinyl chloride
R	reference
RH	relative humidity [%]
RR	round robin
TEM	temperature
VB	vapor barrier
VL	KU Leuven VLIET experimental building
VOC	volatile organic compounds
V&V	verification and validation
W1	WUFI's approach 1 for WDR calculation
W2	WUFI's approach 2 for WDR calculation
WA	wall assembly
WD	wetting-drying process
WDR	wind-driven rain
WF	wood fiber board
WW	pure wetting process
XPS	extruded polystyrene

List of contents

Scientific abstract ..... **I**

Popularized summary ..... **II**

Nomenclature ..... **III**

List of contents ..... **VI**

Chapter 1 Introduction **1**

1.1 Problem statement 1

1.2 Research questions 7

1.3 Thesis outline 8

Part I State-of-the-art **10**

Chapter 2 History and challenges of HAM modeling **11**

2.1 Formulation of governing equations 11

2.2 General classification of uncertainties 14

2.3 Implementation of material properties 16

2.3.1 Heat storage and transport properties 17

2.3.2 Moisture storage properties 17

2.3.3 Moisture transport properties 18

2.4 Implementation of boundary conditions 22

Chapter 3 Quality assessment of HAM models **25**

3.1 Scope and target of quality assessment 25

3.2 Previous quality assessment studies 26

Chapter 4 Summary **34**

Part II Under controlled boundary conditions **35**

Chapter 5 The in-lab experimental setup and datasets **36**

5.1 The HB-CB experimental setup 36

5.2 Material characterization tests and results 41

5.3 Surface transport coefficient measurement and results 45
5.4 Measured hygrothermal responses and validity assessment 47
Chapter 6 Extensive round robin validation campaign 51
6.1 Project overview and methodology 51
6.1.1 Research scheme 51
6.1.2 Participation overview 53
6.1.3 Performance indicators 54
6.2 Overall assessment 55
6.3 Impact of uncertainties in material properties on predicted hygrothermal responses 64
6.3.1 Implementation of material properties in stage 1 64
6.3.2 Implementation of material properties in stage 2 67
6.3.3 Impact of input uncertainties on output accuracies in stages 1 and 2 71
6.3.4 Insights from model fine-tuning in stage 3 74
Chapter 7 Assessing the implementation of material properties in WUFI and DELPHIN 75
7.1 Problem statement and research scheme 75
7.2 Implementation approaches for liquid transport properties 78
7.3 Integral versus separate implementation approaches for vapor and liquid transport properties 86
7.4 Implementation approaches for moisture storage properties 96
Chapter 8 Summary 104
***Part III Towards real-life applications* 105**
Chapter 9 The in-situ experimental setups and datasets 106
9.1 The WDR experimental setups and datasets 106
9.2 Geometric configuration 108
Chapter 10 Assessing the implemented semi-empirical methods for WDR calculation in WUFI and DELPHIN 109
10.1 Impact on WDR loads 109
10.2 Impact on hygrothermal responses 111
10.2.1 Integrated moisture masses and moisture content profiles 112
10.2.2 Heat losses 114

10.2.3 Mold growth risks ... 115
10.2.4 Frost damage risks ... 116
Chapter 11 Summary ... 117
Part IV Conclusion **... 118**
Chapter 12 Key contributions and insights ... 119
12.1 Scientific contributions ... 119
12.1.1 Methodological synthesis and assessment showcase ... 120
12.1.2 Benchmark datasets and round robin validation efforts ... 120
12.2 Practical insights ... 121
12.2.1 Uncertainties in implementing material properties ... 121
12.2.2 Uncertainties in implementing WDR ... 125
12.2.3 Uncertainties related to model biases ... 125
12.2.5 Summary reflection ... 126
Chapter 13 Limitations and outlook ... 127
13.1 Geometry and material heterogeneity ... 127
13.2 Initial and surface conditions ... 127
13.3 Algorithmic trade-offs behind the interfaces ... 128
13.4 Towards a shared infrastructure for HAM model advancement ... 129
Bibliography ... 130
Acknowledgement ... 151
Curriculum Vitae ... 155
Author Declarations ... 159
Declaration of use of generative AI ... 159
Cite this thesis ... 159
Declaration of research data management ... 159

Chapter 1 Introduction

1.1 Problem statement

The hygrothermal performance of building components is critical to their durability and resilience, yet its accurate prediction is hindered by limitations in representing geometric configurations, material properties, boundary conditions and other factors. Numerical heat, air and moisture (HAM) models have emerged as effective alternatives to traditional laboratory and field measurements. Many commercially available models incorporate explicit datasets for required inputs, offering improved calculation stability and user-friendliness. Fig. 1.1 shows the HAM modeling workflow, complemented by interface screenshots from two prevalent HAM models, WUFI and DELPHIN. However, concerns persist about the reliability and robustness of these models, as discrepancies often arise between simulation outcomes and established benchmarks, such as EN 15026 (2004) and EU HAMSTAD ("*Determination of liquid water transfer properties of porous building materials and development of numerical assessment methods*") (Adan et al. 2004; Hagentoft et al. 2004). Notably, when different models are applied to simulate common scenarios, significant deviations are frequently observed, particularly in cases involving complex geometric configurations, material properties, and boundary conditions (Dang et al. 2025a, 2025b). This thesis aims to assess uncertainties stemming from two primary sources: **intrinsic limitations** of the models and **user impact**. The former includes dependencies on model-specific numerical treatments, while the latter refers to input uncertainties primarily in material properties and boundary conditions.

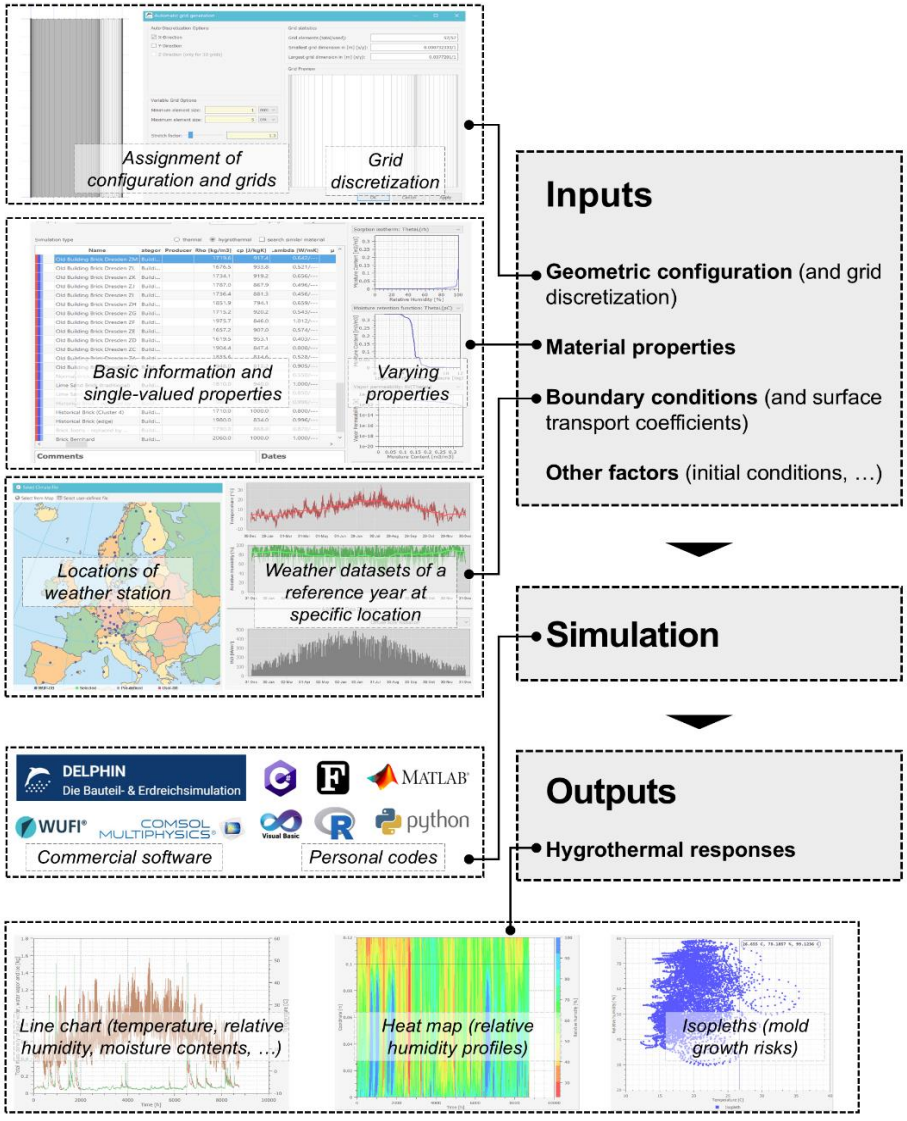


Fig. 1. 1 The workflow of HAM modeling.

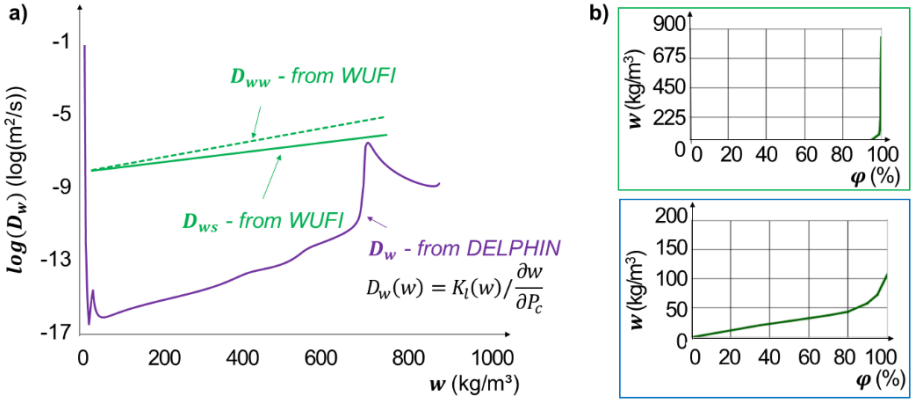
Intrinsic limitations refer to uncertainties arising from various assumptions, simplifications and approximations primarily implemented by model developers. These assumptions may include homogenizing material properties, ignoring local defects and idealizing construction workmanship, etc. Simplifications may include averaging adsorption and desorption isotherms or moisture retention curves to disregard sorption hysteresis, assuming a uniform distribution of wind-driven rain (WDR) loads on walls and applying simplified formulas for material properties that are either untested or

typically derived indirectly (e.g., moisture diffusivity and permeability). Approximations may involve constant-value assignment or inter-/extrapolation to enable mathematical continuation.

User impact encompasses preferences, biases and mistakes in selecting predefined materials or data series from databases or customizing the implementations. For instance, although users generally select material entries with hygrothermal properties that approximate those of the actual construction, the criteria for determining "similarity" can vary considerably — ranging from matching density, thermal conductivity or saturation moisture content to choosing those from the same manufacturer or production batch (Dang et al. 2025a). For surface transport coefficients and solar absorption/reflective rates, users often rely on recommended values from standards or arbitrarily enter values, which may also introduce biases.

To highlight the intrinsic model limitations and user impact regarding material properties, Fig. 1.2 presents two illustrative examples. In Fig. 1.2a, liquid diffusivities obtained from different methods are compared. The purple curve shows values translated from liquid permeability of a calcium silicate (CS) board in DELPHIN's material database (calculated by dividing the slope of the moisture retention curve). In contrast, the green curves, liquid diffusivities for suction D_{ws} [m^2/s] and for redistribution D_{ww} [m^2/s], are calculated based on Künzel's formula (the recommended approach in WUFI, Künzel 1995) using its capillary absorption coefficient A_w [$kg/(m \cdot s^{0.5})$] and free saturation moisture content w_f [kg/m^3] (Dang et al. 2023a). Figs. 1.2b&c demonstrate that material entries with similar names ("wood fibre board") in WUFI's databases differ significantly in hygrothermal properties. This further highlights a broader modeling challenge: the selected entry may not accurately represent the material used in the actual construction, potentially affecting simulation outcomes. While users tend to choose entries that align with technical sheets provided by manufacturers, apparent similarity in one property may mask substantial discrepancies in others (Dang et al. 2025a). Similar uncertainties exist in boundary conditions and other factors.

Evidence from a recent round robin test titled "*Empirical validation of HAM-models based on a dedicated HB-CB experiment*" highlights (the effect) of uncertainties and deviations in inputs and hygrothermal predictions due to both models and users (Dang et al. 2025b). In this exercise, multiple HAM models are used to simulate the same hygrothermal transport process in simple wall assemblies under controlled boundary conditions.



c)

Source	Material Name		Bulk den... [kg/m³]	Porosity [m³/m³]	Heat Cap. [J/kgK]	Therm. C... [W/mK]	Vap.Res. [-]
Fraunhofer-IBP	wood fibre softboard #3		159	0.89	1400	0.04	2.6
Fraunhofer-IBP	wood fibre softboard #2		165	0.999	1400	0.04	2.9
MASEA Database, Germany	Wood-Fibre Insulation Board 1	MASEA	168	0.88	1400	0.0381	3.3
Fraunhofer-IBP	Wood-Fibre Insulation Board		155	0.981	1400	0.042	3
LTH Lund University, Sweden	Woodfibreboard, soft		270	0.83	1700	0.06	6.25
NTNU Norwegian Universi...	Wood fibre board, hard - wind barrier		800	0.8	1700	0.18	9
NTNU Norwegian Universi...	Woodfibre board, hard		800	0.8	1700	0.18	48
LTH Lund University, Sweden	Woodfibreboard, hard		959	0.41	1700	0.13	227

Fig. 1. 2 Uncertainties related to material properties: a) translated liquid diffusivity of one calcium silicate (CS) board in DELPHIN's database and calculated liquid diffusivities based on Künzel's formula, b) & c) sorption isotherms and basic parameters of different "wood fibre board" entries in WUFI's material database.

Fig. 1.3 illustrates simulation results for a specific wall assembly, comparing outputs from WUFI, DELPHIN and other HAM models. Despite using identical measured data as inputs (Dang et al. 2024b, 2024c), the predicted hygrothermal responses vary significantly. While heat-related predictions remain relatively consistent, moisture-related results exhibit considerable divergence. This highlights how variations in the implemented (particularly hygric) material properties can significantly influence the simulation outcomes. These discrepancies primarily arise from: (1) different assumptions, simplifications and approximations in the formulation of moisture transport and storage within HAM models, and (2) users' preferences, biases and errors in selecting, processing and implementing material properties. This case exemplifies the core concerns addressed in this thesis: the critical need to systematically evaluating input-related uncertainties and to develop guidelines that enhance the **reliability** and **robustness** of model predictions.

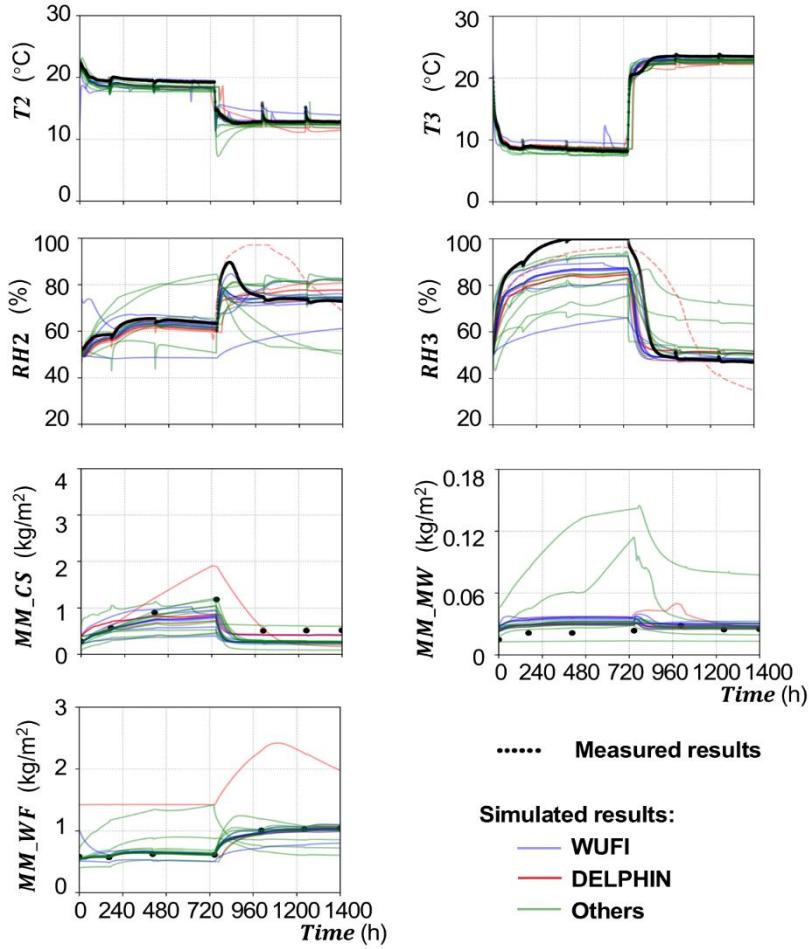


Fig. 1. 3 Simulated hygrothermal responses of the first wall assembly compared with the measured data in the round robin test (T: temperature; RH: relative humidity; MM: moisture mass; CS: calcium silicate board; MW: mineral wool board; WF: wood fiber board; the numbers after the indicators refer to the locations of the interfaces; cf. Chapter 6).

Reliability refers to the degree of dependability in delivering expected results under determined conditions. When measured values are assigned to inputs, a reliable simulation should exhibit good agreement and coherence with measured datasets and/or predictions by other models.

Robustness typically refers to the plasticity of a system to maintain its desired performance under "uncertain" conditions, which in this context means certain variability in the implemented inputs and actual characteristics. Deviations primarily arise from two sources: (1) the use of entries from databases of material properties, weather conditions and surface transport

coefficients, which may differ from the reality, and (2) the implementation of measured data as inputs, which may still carry inherent mismatch risks between observations and reality due to human factors and technical constraints. A robust simulation ensures that overall trends and patterns of the results remain consistent with reality, regardless of reasonable variability of these factors. Note that there is no universally accepted quantitative definition of reliability and robustness. The distinction here is just made on the inputs — whether they are measured and determined (in "reliability tests") or varied and undetermined (in "robustness tests").

Fig. 1.4 outlines the stepwise research scheme for HAM model quality assessment, which forms the core task of this thesis. Experimental datasets used in previous validation studies often fall short in capturing the complexity of real-world conditions, thereby limiting their representativeness. Similarly, inter-model comparisons based solely on hypothetical scenarios reduce their effectiveness. Given the shortcomings of both approaches, this thesis advocates for an integrated analysis rather than relying exclusively on either method. To this end, the research combines **experimental validation** with **inter-model comparison** using two sets of benchmark datasets, each characterized by different spatial scales, complexity levels and boundary conditions. One set, with controlled boundary conditions, focuses on uncertainties in material property implementation. The other set, reflecting real-life applications, targets uncertainties in boundary condition settings. WUFI and DELPHIN are selected for the assessment procedure, while other HAM models may be included for broader evaluation.

While neither model predictions nor reference data can fully replicate reality, both provide valuable insights when carefully interpreted. Even verified HAM models remain vulnerable to developer-induced errors and biases. Similarly, experimental data are not absolute ground truth, since both the inputs (e.g., material properties, boundary conditions) and outputs (e.g., hygrothermal responses) are subject to manual handling errors and instrumental inaccuracies. These limitations necessitate a closer examination of how uncertainties in inputs propagate into output deviations. While systematic biases and measurement variability are inevitable, this thesis aims to isolate input-driven effects through controlled, stepwise comparisons.

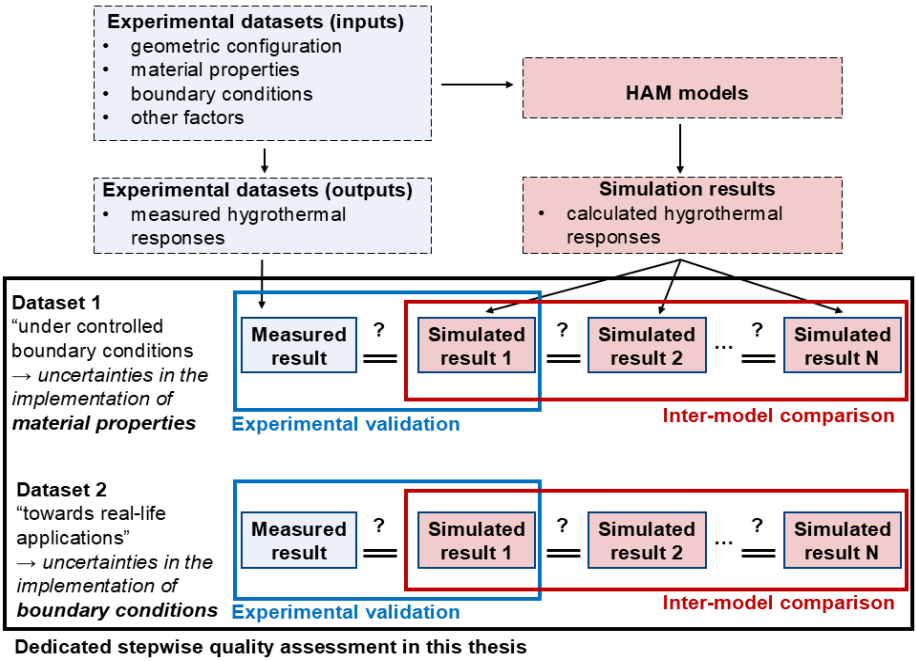


Fig. 1. 4 Logic and objectives of the stepwise quality assessment of HAM models.

1.2 Research questions

While HAM models have been extensively employed to predict the hygrothermal behavior of building components, their reliability and robustness are significantly influenced by the uncertainties arising from intrinsic model limitations and user impact on inputs. This PhD research starts with identifying key factors contributing to discrepancies in simulated hygrothermal responses. Subsequently, the influence of these uncertainties on simulation accuracy is evaluated through a stepwise and comprehensive methodology.

Question 1: what factors are responsible for the deviations in simulated hygrothermal responses? This thesis first formulates the governing equations and categorizes the limitations arising from specific assumptions, simplifications and approximations in the implementation of material properties, boundary conditions, etc.

Question 2: how sensitive are the simulated hygrothermal responses to the uncertainties in inputs? This thesis investigates the sensitivity of HAM model outputs to uncertainties in material properties and boundary conditions, using two dedicated experimental datasets. The first —

under controlled boundary conditions — examines deviations in material data between model databases and experimental measurements, including discrepancies from different characterization and processing methods. The second — towards real-life applications — focuses on exterior boundary conditions, particularly WDR, comparing semi-empirical estimation methods and their implementation assumptions. By confronting simulated responses with experimental results and inter-model predictions, the study identifies key sources of deviation and evaluates HAM models' sensitivity to input variability.

Question 3: how can implementations be adjusted to improve the accuracy of outputs? Multiple strategies for implementing material properties are tested across scenarios. Approaches yielding close agreement with measured datasets are identified as optimal solution. Based on these outcomes and observed limitations, practical recommendations are proposed.

1.3 Thesis outline

Given the multiple uncertainties involved in input variations and output accuracies, a stepwise research scheme is developed for model quality assessment, integrating experimental validation and inter-model comparison to systematically evaluate the reliability and robustness of HAM models. The PhD thesis first revisits the evolution of HAM modeling algorithms, the primary sources of simulation errors and the limitations in previous model assessment studies. A multi-method analysis then examines how uncertainties in material properties (under controlled conditions) and in WDR estimation (under real climates) contribute to deviations in hygrothermal predictions. Finally, it offers insights for improving model consistency and validity.

This current **Chapter 1 (Introduction)** discussed the challenges in HAM modeling and defined the three main research questions: identifying the responsible factors for the reliability and robustness of simulated responses, assessing the sensitivity of these outcomes to model and input uncertainties, and exploring ways to improve their dependability.

Part I (State-of-the-art) contextualizes the primary challenges in HAM modeling, providing the foundation for understanding the necessity and relevance of this research. **Chapter 2 (History and challenges of HAM modeling)** elaborates on the formulation of governing equations for HAM models, and subsequently categorizes the modeling uncertainties, emphasizing the importance of accurate data and the challenges involved in their implementation.

Chapter 3 (Quality assessment of HAM models) revisits previous practices, highlighting their limitations in scopes, methodologies and benchmarks. A stepwise and comprehensive methodology is subsequently proposed, employing dedicated benchmark datasets to evaluate the impact of material properties and boundary conditions on predicted hygrothermal responses.

Part II (Under controlled boundary conditions) primarily deals with the implementation of material properties as main uncertainty based on an in-lab experimental benchmark dataset. **Chapter 5 (The in-lab experimental setup and datasets)** describes the experimental setups and measured results of material properties, boundary conditions, surface transport coefficients and hygrothermal responses. **Chapter 6 (Extensive round robin validation campaign)** summarizes an extensive and intensive round robin validation campaign based on this dataset. **Chapter 7 (Assessing the implementation of material properties in WUFI and DELPHIN)** presents an in-depth assessment of implementation strategies for material properties in two prevalent HAM models, WUFI and DELPHIN.

Part III (Towards real-life applications) moves towards the implementation of boundary conditions (specifically WDR), based on in-situ experimental benchmark datasets. **Chapter 9 (The in-situ experimental setups and datasets)** introduces the experimental setups and measured results. **Chapter 10 (Assessing the implemented semi-empirical methods for WDR calculation in WUFI and DELPHIN)** compares the impact of different semi-empirical methods on simulated WDR loads and the resulting simulated hygrothermal responses in WUFI and DELPHIN.

Part IV (Conclusion) concludes the thesis. **Chapter 12 (Key contributions and insights)** summarizes the main contributions of the research, and highlights the key findings and their implications for HAM modeling. **Chapter 13 (Limitations and outlook)** examines the limitations of this study and suggests potential directions for future research.

The final chapters of each part, **Chapters 4, 8 and 11 (Summary)**, summarize the key takeaways.

Part I State-of-the-art

This part formulates the governing equations in heat, air and moisture (HAM) modeling and the implementation approaches of material properties and boundary conditions. It reviews previous efforts and identifies limitations in previous studies of HAM models quality assessment. It then introduces the systematic methodology in this research, which combines experimental validation and inter-model comparison to stepwise evaluate the impact of implemented material properties and boundary conditions on predicted hygrothermal responses.

This part is partially based on Dang et al. (2023a, 2023b, 2024a, 2024b, 2025a, 2025b, 2025c, 2025d, 2025e, 2026).

Chapter 2 History and challenges of HAM modeling

This chapter first revisits the general formulation of the governing equations using two typical derivation methods that guide two advanced and representative heat, air and moisture (HAM) models: WUFI and DELPHIN. It then elaborates on the implementations of two primary input factors: material properties and boundary conditions, emphasizing the uncertainties arising from different strategies in their determination and implementation, which may result in deviations in the simulated hygrothermal responses.

2.1 Formulation of governing equations

Building on Glaser's one-dimensional steady-state vapor diffusion model (1958), Philip and de Vries' coupled heat-and-moisture transfer model (1957) and Luikov's continuity conditions (1964), recent decades have witnessed the profound evolution and the increasing complexity of HAM models in predicting the hygrothermal responses of building components. In these, a multitude of hygric driving potentials, and their corresponding hygrothermal material properties, have been introduced to represent moisture flow (Straube and Burnett 2001; Hens 2007; Janssen et al. 2007; Funk et al. 2008; Janssen 2011). These driving potentials and corresponding material properties can be interconverted through mathematical or physical relationships (Hagentoft 2002). Meanwhile, considerable efforts have been focused on measuring and processing material properties (Roels et al. 2004, 2010; Jerman et al. 2019; Ren et al. 2019; Feng et al. 2020; Feng and Janssen 2021; Zhou et al. 2022), boundary conditions (Blocken and Carmeliet 2004, 2006, 2010a; Carbonez et al. 2015; Gholamalipour et al. 2022), and specific moisture sources and effects, including wind-driven rain (WDR) (Abuku 2009), interstitial condensation (Ramos et al. 2009) and rising damp (Franzoni 2014).

Throughout the years, numerous HAM models have been developed (reviews can be found in Hens 1996; Canada Mortgage and Housing Corporation 2003; Delgado et al. 2010, 2012). Most models, however, were only reported

by their developers in references without easy public access, including MATCH (Pedersen 1990, 1992), LATENITE (Karagiozis 1993; Salonvaara and Karagiozis 1994), MOIST (Burch et al. 1996), UMIDUS (Mendes et al. 1999, 2003), 1D-HAM (Hagentoft and Blomberg 2000), MOISTURE-EXPERT (Karagiozis 2001), HAMFEM (Janssen et al. 2007), hygIRC (Defo 2018), etc. On the other hand, **WUFI** (Künzel 1995) and **DELPHIN** (Häupl and Fechner 2003) have recently emerged as the two prevalent HAM models, available for public use and suitable for transient component-scale hygrothermal simulation (Brambilla and Sangiorgio 2021). These two models incorporate built-in databases of typical weather conditions and material properties as well as dedicated outputs of moisture-related risk metrics, such as mold growth isopleths (Sedlbauer 2001; Nicolai et al. 2007) and VTT model (Hukka and Viitanen 1999).

WUFI has been developed by the Department of Hygrothermics at Fraunhofer Institute in Building Physics stemming from the PhD research of Künzel H. M. (1995). This model addresses transient heat and moisture transport. The software suite consists of several individual applications tailored to different dimensions: WUFI Pro (one-dimensional components), WUFI 2D (two-dimensional components), WUFI Plus and WUFI Passive (whole buildings).

DELPHIN has been developed at the Dresden University of Technology originating from the PhD research of Häupl P. and Stopp H. (1987). Through multiple iterations (Grunewald 1997; Nicolai et al. 2007), the latest version, DELPHIN 6, has evoked to simulate the transport of heat, air, moisture, salt and VOC. While existing as a single software package, it can handle one-, two-, rotationally symmetric three- and full three-dimensional assemblies.

This study mainly focuses on one-dimensional hygrothermal simulation through WUFI Pro 6.7 and DELPHIN 6.1, while neglecting air, salt and VOC transport considered by DELPHIN. The following paragraphs describe the standard description of the moisture and heat equations in HAM modeling.

Regarding the moisture balance, the moisture mass change in each control volume over time should always equal the total amount of all incoming and outgoing moisture flows. Vapor and liquid transport follow Fick's law (Fick 1995) and Darcy's law (Darcy 1856), respectively. General formulations of 1D moisture balance are formulated in Eqs. 2.1 and 2.2, derived using two different driving potentials for liquid transport: relative humidity (RH) φ [%] (WUFI's choice) and capillary pressure P_c [Pa] (DELPHIN's default choice).

$$\frac{\partial w}{\partial t} = -\nabla(g_v + g_l) = \nabla(\delta_v \nabla P_v + D_w \nabla w) \tag{2.1}$$

$$= \nabla\left(\delta_v \nabla P_v + D_w \frac{\partial w}{\partial \varphi} \nabla \varphi\right)$$

$$= \nabla\left(\delta_v\left(P_{vsat}\nabla\varphi + \varphi\frac{\partial P_{vsat}}{\partial T}\nabla T\right) + D_w\frac{\partial w}{\partial\varphi}\nabla\varphi\right) \text{ [as } P_v = \varphi\cdot P_{vsat}(T)\text{]}$$

$$= \nabla\left(\left[\delta_v\varphi\frac{\partial P_{vsat}}{\partial T}\right]\boldsymbol{\nabla T} + \left[\delta_v P_{vsat} + D_w\frac{\partial w}{\partial\varphi}\right]\boldsymbol{\nabla\varphi}\right)$$

$$\frac{\partial w}{\partial t} = -\nabla(g_v + g_l) = \nabla(\delta_v\nabla P_v + K_l\nabla P_c) \tag{2.2}$$

$$= \nabla\left(\delta_v\left(P_{vsat}\nabla\varphi + \varphi\frac{\partial P_{vsat}}{\partial T}\nabla T\right) + K_l\nabla P_c\right) \text{ [as } P_v = \varphi\cdot P_{vsat}(T)\text{]}$$

$$= \nabla\left(\delta_v\left(P_{vsat}\left(\frac{\partial\varphi}{\partial P_c}\nabla P_c + \frac{\partial\varphi}{\partial T}\nabla T\right) + \varphi\frac{\partial P_{vsat}}{\partial T}\nabla T\right) + K_l\nabla P_c\right) \text{ [as } \varphi = f(P_c, T)\text{]}$$

$$= \nabla\left(\delta_v\left(P_{vsat}\left(\left(\frac{\varphi}{\rho_w R_v T}\right)\nabla P_c + \left(\frac{-P_c\varphi}{\rho_w R_v T^2}\right)\nabla T\right) + \varphi\frac{\partial P_{vsat}}{\partial T}\nabla T\right) + K_l\nabla P_c\right) \text{ [as } \varphi = e^{\frac{P_c}{\rho_w R_v T}}\text{]}$$

$$= \nabla\left(\left[\delta_v\varphi\frac{\partial P_{vsat}}{\partial T} - \frac{\delta_v P_{vsat}P_c\varphi}{\rho_w R_v T^2}\right]\boldsymbol{\nabla T} + \left[K_l + \frac{\delta_v\varphi P_{vsat}}{\rho_w R_v T}\right]\boldsymbol{\nabla P_c}\right)$$

where w [kg/m^3] is moisture content; t [s] is time; g_v and g_l [kg/(m^2·s)] are vapor and liquid fluxes respectively; δ_v [kg/(m·s·Pa)] is vapor permeability; P_v and P_{vsat} [Pa] are vapor pressure and saturation vapor pressure respectively; D_w [m^2/s] is liquid diffusivity; x [m] is distance; T [K] is temperature; K_l [kg/(m·s·Pa)] is liquid permeability; ρ_w [kg/m^3] is the density of water; R_v [J/(kg·K)] is the water vapor constant.

For the heat balance, similarly, the enthalpy change in each control volume over time should always equal to the total amount of all the incoming and outgoing heat flows. The conduction part is expressed as in Fourier's law (Fourier 1878), while the convection part consists of latent and sensible components, as shown in Eq. 2.3.

$$\frac{\partial H}{\partial T}\frac{\partial T}{\partial t} + \frac{\partial H}{\partial w}\frac{\partial w}{\partial t} = \left(c_{dry}\rho_{dry} + c_l w_l + c_v w_v\right)\frac{\partial T}{\partial t} \tag{2.3}$$

$$= -\nabla(q_{cond} + q_{conv})$$

$$= \nabla(\lambda\nabla T + (L_v + c_v T)g_v + c_l T g_l)$$

where c [J/(kg·K)] is specific heat capacity, with subscripts dry, l and v corresponding to dry material, liquid water and water vapor respectively; H [J/m^3] is enthalpy density; q_{cond} and q_{conv} [J/(m^2·s)] are conductive and convective heat fluxes respectively; L_v [J/kg] is the latent heat of evaporation; g_v and g_l [kg/(m^2·s)] are vapor and liquid fluxes respectively; ρ [kg/m^3] is density.

By substituting the moisture flux expressions from Eqs. 2.1 and 2.2 into Eq. 2.3, the equation can be further expanded into Eqs. 2.4 and 2.5, respectively.

$$\nabla(\lambda\nabla T + (L_v + c_v T)g_v + c_l T g_l) \tag{2.4}$$

$$= \nabla\left(\lambda\nabla T + (L_v + c_v T)\cdot\delta_v\left(P_{vsat}\nabla\varphi + \varphi\frac{\partial P_{vsat}}{\partial T}\nabla T\right) + c_l T\cdot D_w\frac{\partial w}{\partial\varphi}\nabla\varphi\right)$$

$$= \nabla\left(\left[\lambda + \delta_v\varphi(L_v + c_vT)\frac{\partial P_{vsat}}{\partial T}\right]\boldsymbol{\nabla T} + \left[c_lTD_w\frac{\partial w}{\partial \varphi} + \delta_vP_{vsat}(L_v + c_vT)\right]\boldsymbol{\nabla\varphi}\right)$$

$$\nabla(\lambda\nabla T + (L_v + c_vT)g_v + c_lTg_l) \tag{2.5}$$
$$= \nabla\left(\lambda\nabla T + (L_v + c_vT)\cdot\delta_v\left(P_{vsat}\left(\left(\frac{\varphi}{\rho_wR_vT}\right)\nabla P_c + \left(\frac{-P_c\varphi}{\rho_wR_vT^2}\right)\nabla T\right) + \varphi\frac{\partial P_{vsat}}{\partial T}\nabla T\right) + c_lT\cdot K_l\nabla P_c\right)$$
$$= \nabla\left(\left[\lambda - \frac{\delta_vP_c\varphi(L_v+c_vT)}{\rho_wR_vT^2}\right]\boldsymbol{\nabla T} + \left[c_lTK_l + \frac{\delta_vP_{vsat}\varphi(L_v+c_vT)}{\rho_wR_vT}\right]\boldsymbol{\nabla P_c}\right)$$

On the right of Eqs. 2.1 – 2.5, the partial derivatives are the driving potential gradients, and the front parts in square brackets are the corresponding material properties and associated hygrothermal variables.

The moisture balance equations, which involve vapor diffusion and liquid transport (Eqs. 2.1 and 2.2), are completely implemented in both WUFI and DELPHIN. The heat balance in DELPHIN remains consistent with Eqs. 2.3 and 2.5. However, in WUFI, the advection of sensible heat due to liquid flow or vapor transport is neglected; specifically, the components "$c_vTg_v + c_lTg_l$" on the right side of Eq. 2.3 are omitted.

2.2 General classification of uncertainties

The reliability and robustness of simulation results are influenced by various factors. While HAM models are generally mathematically and physically equivalent, their complexity can vary significantly (Galbraith 1992; Janssen et al. 2007; Funk et al. 2008; Dos Santos et al. 2009; Janssen and Carmeliet 2015; Berger et al. 2017; Hamdaoui et al. 2021). Generally, incorporating more considerations leads to a more comprehensive model, albeit at the cost of increased demands for experiments and data processing (Chang and Weng 2002). Moreover, accurately determining all parameters, particularly in practical engineering applications, is challenging. Therefore, a compromise must be made between efficiency and complexity. HAM models may disregard factors such as sorption hysteresis (Lelievre et al. 2014; Issaadi et al. 2015; Zhang et al. 2016) and the temperature dependency of moisture storage capacity (Colinart and Glouannec 2016). As different assumptions, simplifications and approximations in implementing material properties (Grint et al. 2020; Marincioni et al. 2018) and boundary conditions (Defraeye et al. 2013; Chung and Wen 2019; Aude et al. 2000) contribute to discrepancies in predictions across different models (Busser et al. 2018), it is essential to assess their impact

throughout the HAM models' workflow. The basic workflow consists of four stages: **basic customizations**, **implementation of material properties and boundary conditions**, **simulation** and **outputs**.

First, users customize the geometry, estimate the initial conditions, and select the optimal discretization, time step, etc. Most models assume structures to be ideally "regular and uniform", neglecting local defects and variations in construction quality. This assumption generally does not pose significant problems unless there are considerable discontinuities in geometry or material properties, such as in deteriorated historical structures, corners or edges that cannot be homogenized. The impact of initial conditions can be mitigated by repeating the simulation and selecting the results from pre-runs. Although the discretization in space and time affects accuracy, it can be improved with finer spatial and temporal grids.

Second, the implementation of material properties, boundary conditions (including surface transport coefficients) should be determined by user-defined values, data series or entries from built-in databases.

Variability in implemented material properties is a primary reason for discrepancies among simulation results from different models. Observed differences among characterization tests (Feng and Janssen 2021) suggest that certain assumptions may be involved in interpreting material properties. For example, moisture storage curves derived from mercury intrusion porosimetry (MIP) frequently differ from those obtained through the desiccator test in the hygroscopic range, while adsorption and desorption curves exhibit hysteresis-induced discrepancies. Moreover, some properties cannot be directly measured but are instead inferred from other parameters. For instance, liquid diffusivity can be indirectly obtained from measured moisture profiles using Boltzmann transformation (Roels et al. 2003) or estimated via simplified alternatives with varying degrees of accuracy (Ren et al. 2019). Translating liquid diffusivity into liquid permeability introduces further process-dependent deviations (Dang et al. 2023a). While this study does not explicitly examine uncertainties stemming from material heterogeneity, instrumental limitations or tester-induced variability (Feng et al. 2015), it operates under the practical assumption that the measured material properties are representative sufficiently for modeling purposes. The focus is placed on how different strategies of assumption, simplification and approximation from measurement data to model inputs affect hygrothermal predictions. In addition to differences in how measured data are implemented, further deviations arise from the practices of model users who do not perform material characterization and often rely on material databases or technical sheets. While such selections aim to

match materials with "similar" properties to those used in actual construction, they do not always yield comparable hygrothermal responses, especially when choices are based on material names or brands rather than physical characteristics (see Fig. 1.2b&c).

Uncertainties in implemented boundary conditions arise from model-specific assignments and mismatches between prescribed and actual environmental conditions. For example, semi-empirical methods integrated in HAM models to estimate wind-driven rain (WDR) are based on similar but not identical assumptions, such as uniform distribution across a facade or consistent exposure at a given height. Additional adjustments are often introduced during model implementation to accommodate specific contexts (Dang et al. 2024a). Discrepancies may also occur when relying on standard meteorological data from weather stations, which may not accurately reflect site-specific conditions (Blocken and Carmeliet 2010a; Hens 2015).

Similarly, the reference values for surface transport coefficients defined in standards may not accurately reflect the actual behavior. Ideally, the implementation should account for both spatial and temporal transience, but this is often impossible due to practical restrictions and computational demands. Fixed-value assignments are commonly applied to improve calculation efficiency but may come at the expense of accuracy and physical validity.

After running the simulation, the model produces hygrothermal responses as outputs. Rather than immediately analyzing results, it is important to first understand how and to what extent they are shaped by underlying uncertainties. While many users of HAM models may not routinely engage in such analysis due to practical constraints, it is a central focus of this study.

As factors such as grid discretization, time step and initial conditions are recognized as "manageable" through iterative adjustment., the study specifically focuses on the uncertainties in the implementation of material properties and boundary conditions and their impact on simulation outcomes.

2.3 Implementation of material properties

Both WUFI and DELPHIN provide built-in material databases and support user-defined entries, provided they meet the model-specific requirements, such as ensuring monotonicity. This section outlines the approaches for characterizing, estimating, processing and implementing material properties. Variability of these properties — such as thermal conductivity (Holm and

Künzel 2002), sorption isotherms (Salonvaara et al. 2001), vapor resistance factor (Zhao et al. 2011) and liquid permeability (Defraeye et al. 2013) — constitutes a major source of uncertainty in hygrothermal predictions.

2.3.1 Heat storage and transport properties

Specific heat c [J/(kg·K)] represents heat storage capacity. For actual calculation, volumetric specific heat C [J/(K·m³)] is derived by multiplying c with density ρ [kg/m³]. In WUFI, approximate values of 850 J/kg·K and 1500 J/kg·K are assigned to mineral and organic materials respectively. Internal energy (approximating the enthalpy under isobaric conditions in most building physical scenarios) can be expressed as a temperature dependent function $u(T)$ [J/kg] for modeling heat transport in phase-change materials in DELPHIN (Nicolai and Grunewald 2006). Similarly, WUFI can define enthalpy as a $H(T)$ function [J/m³] (Dieckmann and Heinrich 2008).

For heat transport modeling, the thermal conductivity λ [W/(m·K)] is expressed as a function of moisture content $\lambda(w)$ or $\lambda(\theta_l)$ in WUFI and DELPHIN (Eqs. 2.6 and 2.7, respectively), where b is a supplement factor, ranging from 1.5 to 8, predefined on the material bulk density (e.g., wood: 1.5; concrete and lime silica brick: 8). An optional dependency of $\lambda(T)$ is available in WUFI as Eq. 2.8. When both dependent functions are provided, WUFI employs linear interpolation as a binary function to estimate values between the given data points. Likewise, if both functions are present, DELPHIN normalizes them according to Eq. 2.9 (i.e., $\lambda(T)|_{293.15\,\mathrm{K}} = \lambda(\theta_l)|_{0\,\mathrm{m^3/m^3}} = 1$).

$$\lambda(w) = \lambda_{dry} + \frac{\lambda_{dry} \cdot b}{\rho} w \tag{2.6}$$

$$\lambda(\theta_l) = \lambda_{dry} + 0.56\theta_l \tag{2.7}$$

$$\lambda(T) = \lambda|_{283.15\mathrm{K}} + 0.0002(T - 283.15) \tag{2.8}$$

$$\lambda(T_0, \theta_l) = \lambda_{dry} \cdot \lambda(T)|_{T_0 - 293.15} \cdot \lambda(\theta_l)|_{\theta_l} \tag{2.9}$$

2.3.2 Moisture storage properties

The moisture storage capacity, represented as either sorption isotherm $w(\varphi)$ in WUFI or moisture retention curve $w(P_c)$ in DELPHIN (where $w(\varphi)$ function can be alternatively used), describes the equilibrium between moisture contents and moisture potentials in porous materials. Within the hygroscopic range, the moisture storage function can be determined using the

gravimetric desiccator method (ISO 12571), which involves storing and weighing samples exposed to different relative humidity (RH) conditions. In the over-hygroscopic range, the moisture storage function can be derived from the pressure plate test (ISO 11274), MIP test (ISO 15901-1), etc.

While Kelvin's law (Eq. 2.10) facilitates the conversion between the two functions, inherent experimental limitations often result in discrepancies, such as the substantial underestimation of MIP outcomes than the desiccator results in the hygroscopic range (Good and Mikhail 1981; Cook and Hover 1993; Diamond 2000). Note that sorption isotherm and moisture retention curve are more appropriate for describing the hygroscopic and over-hygroscopic ranges respectively, though some overlap between the two exists. Additionally, it is recommended to fit the raw data of (different, if any) characterization test(s) (Feng and Janssen 2021). Various fitting functions have been suggested for sorption isotherm curve (Oswin 1946; Henderson 1952; Caurie 1970; Van den Berg and Bruin 1978; Freiesleben-Hansen 1985; Peleg 1993; Kumaran et al. 1994; Furmaniak et al. 2005; Feng et al. 2013), and WUFI can alternatively generate a fitting curve based on the assigned moisture contents at 0 %, 80 % and 100 % RH (Eq. 2.11). By contrast, moisture retention curve can be also fitted (Grunewald et al. 2003), for instance, using the classic Van Genuchten model (Van Genuchten 1980) (Eq. 2.12). WUFI and DELPHIN both impose a strict monotonicity requirement and exclude sorption hysteresis.

$$P_c = \rho_w \cdot R_v \cdot T \cdot ln\varphi \tag{2.10}$$

$$w(\varphi) = w_f \cdot \frac{(b-1)\cdot\varphi}{b-\varphi} \tag{2.11}$$

$$w(P_c) = w_{cap} \cdot \sum_{i=1}^{n} \left(l_i \cdot (1 + (m_i \cdot log_{10} P_c)^{n_i})^{\frac{1-n_i}{n_i}} \right) \tag{2.12}$$

where free saturation moisture content w_f [kg/m^3] indicates capillary saturation moisture content w_{cap} [kg/m^3]; l, m, n are the fitting parameters.

2.3.3 Moisture transport properties

Apart from some budding numerical techniques to determine the moisture permeability K_l [s] (Islahuddin and Janssen 2019), the main approach is to experimentally derive the moisture diffusivity D_w [m^2/s]. It starts with the Boltzmann transformation (Eq. 2.13) of transient moisture content profiles $w\left(x/\sqrt{t}\right)$ obtained via X-ray attenuation or nuclear magnetic resonance (NMR) during a capillary absorption process (Carmeliet et al. 2004; Roels and Carmeliet 2006) (Fig. 2.1a). While these imaging methods enable precise

moisture profiling (Wolter and Krus 2005), they are not always accessible. Alternatives, including the ruler method (Evangelides et al. 2010, 2018), the multi-step method (Bianchi Janetti 2018) and Künzel's formula (Künzel 1995), can be applied with different accuracies (Fig. 2.1b). Among them, the ruler method seems to provide results closest to X-ray attenuation but is limited to materials with a distinct waterfront, while the multi-step method is applicable to most porous materials but requires extensive sample conditioning and complex data processing (Ren et al. 2019). Künzel's formula is the simplest approach while lacking consistent accuracy. As shown in Eq. 2.14, it is dependent on the capillary absorption coefficient A_w [kg/(m·s$^{0.5}$)] and the "free" saturation moisture content w_f [kg/m^3] (equivalent to w_{cap} obtained in a capillary absorption test, ISO 15148). Moisture diffusivity can be converted into permeability via the slope of the moisture retention curve (Eq. 2.15).

$$D_w = -\frac{\int_{w(0)}^{w(x/\sqrt{t})}(x/\sqrt{t})dw}{2\cdot\frac{\partial w}{\partial(x/\sqrt{t})}} \tag{2.13}$$

$$D_{ws} = 3.8\cdot\left(\frac{A_w}{w_f}\right)^2\cdot 1000^{\frac{w}{w_f}-1} \tag{2.14}$$

$$K_l = D_w\cdot\frac{\partial w}{\partial P_c} \tag{2.15}$$

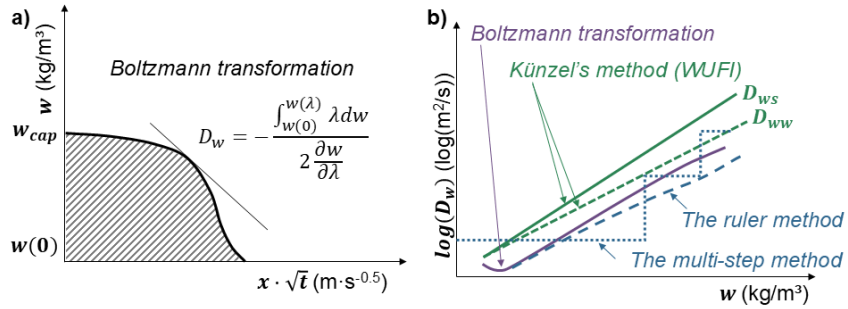


Fig. 2. 1 Schematic illustration of the characterization, processing and implementation of liquid diffusivity: a) Boltzmann transformation, b) schematic comparison between liquid diffusivities obtained from measurement and other simplification methods.

Fig. 2.2 illustrates the notable deviations in liquid diffusivities D_w and corresponding translated liquid permeabilities K_l of the same calcium silicate (CS) material, using the ruler method (Evangelides et al. 2010, 2018) and Künzel's formula (Eq. 2.14) (Dang et al. 2025b).

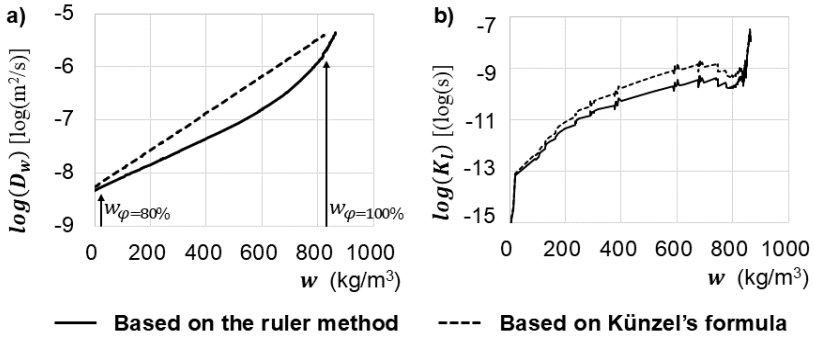


Fig. 2. 2 Liquid transport coefficients of a CS material derived via the ruler method and Künzel's formula: a) liquid diffusivities and b) liquid permeabilities.

WUFI only supports the $D_w(w)$ function and it distinguishes between two variants: D_{ws} for liquid suction and D_{ww} for liquid redistribution (Wufi-Wiki1). The former describes capillary water uptake when the imbibing surface is fully wetted, while the latter describes the redistribution of absorbed water once wetting ceases. WUFI requires both functions but dynamically selects which function to apply at each computational time step depending on whether the WDR boundary condition is non-zero (Künzel and Kiessl 1996). This selection applies uniformly across the entire material domain, disregarding spatial variations in moisture sorption. WUFI treats the moisture diffusivity as liquid-dominated and activates it only when RH reaches 80 %. Künzel's formula (Eq. 2.14) is the default solution for the $D_{ws}(w)$ function in WUFI, requiring two values at 80 % and 100 % RH for logarithmic interpolation. The $D_{ww}(w)$ function is derived analogously, interpolated between D_{ws} at 80 % RH and 0.1 times D_{ws} at 100 % RH, reflecting the assumption that moisture redistribution within the material is significantly slower than suction-driven moisture uptake (Kießl 1983; Künzel 1995). In DELPHIN, $K_l(w)$ function appears as default function, while $D_w(w)$ function can be used alternatively. Unlike WUFI's flexibility, DELPHIN requires both curves to be monotonic.

Note that the aforementioned approaches typically capture the absorption process; however, moisture diffusivity in lower moisture content range remain uncertain and must be supplemented with additional tests to account for vapor transport contribution (Roels et al. 2003). Dry (or wet) cup tests (ISO 12572) are commonly used to determine the vapor-dominated moisture transport properties under specific RH conditions. These properties are expressed as vapor diffusion coefficient δ_v [s] (under the gradient of vapor pressure P_v) or vapor diffusion resistance factor μ [-] (defined as the ratio of vapor diffusion coefficient in air δ_a [s] and that in material δ_v [s]). In WUFI, a $\mu(\varphi)$ function is applicable; in DELPHIN, either $\mu(\varphi)$ function or the vapor

permeability $K_v(w)$ function can be assigned. Specifically, K_v [s] (under the gradient of capillary pressure P_c) can be mathematically converted from vapor diffusion coefficient δ_v [s] (under the gradient of vapor pressure P_v). The vapor diffusion coefficient in air δ_a [s] is determined by the ratio of vapor diffusivity in air D_{va} [m^2/s] and the product of water vapor constant R_v [J/(kg·K)] and temperature T [K]. The three parameters are internally fixed as constants by DELPHIN (Vogelsang et al. 2013): T = 293.15 K, R_v = 462 J/(kg·K), D_{va}= 26.1×10^{-6} m^2/s. Since liquid water partially fills the pores in the wet cup tests, vapor transport is affected by the saturation and air entrapment (Fukui and Takada 2024). To account for this, a reduction in vapor transport properties can be considered, for instance, using a non-linear reduction approach as adopted in the HAMSTAD benchmark exercise (Adan et al. 2004; Hagentoft et al. 2004). Eq. 2.16 formulates vapor permeability as a function of capillary pressure (since it is the actual driving potential in DELPHIN), $K_v(P_c)$, incorporating this reduction approach. In this case, the vapor resistance factor measured in the dry cup test μ_{dry} [-] is utilized.

Another key uncertainty is whether to treat vapor and liquid transport terms separately or integrally. Vapor transport is dominant in the low moisture content range, and therefore the μ_{dry} is assumed to represent the pure vapor transport term. In contrast, wet cup tests also comprise the liquid transport contribution, which can be quantified as the difference between the total and the vapor transport terms (Eq. 2.17). When applying the reduction for the vapor transport term, e.g., the factor $\frac{1-\frac{w}{w_{sat}}}{0.503\cdot\left(1-\frac{w}{w_{sat}}\right)^2+0.497}$ in Eq. 2.16, the vapor transport term $\frac{\delta_a}{\mu_{dry}}$ in Eq. 2.17 should likewise be reduced to ensure consistency. However, cup tests do not capture the over-hygroscopic range, where liquid-dominant moisture transport properties must instead be characterized through alternative approaches. Therefore, one solution is to separately implement the vapor and liquid transport properties from different sources. For instance, WUFI's developers suggest using a constant μ_{dry} value, paired with an $D_w(w)$ function (WUFI forum1). The other solution, particularly when liquid transport is not dominant, is to treat vapor and liquid transport terms integrally purely based on the cup tests. This involves using a $\mu(\varphi)$ function without explicitly implementing liquid diffusivity. For DELPHIN, since the $K_v(w)$ function is based on μ_{dry} as obtained from the dry cup test, the vapor transport term is exclusively characterized, while the $K_l(w)$ function solely represent the liquid transport term. There are two major errors commonly made in the implementation. The first is "redundant consideration", where both a $\mu(\varphi)$ function and a $D_w(w)$ function are implemented that incorporate liquid transport term repeatedly in the low moisture range. The second is

"insufficient consideration", where only a $\mu(\varphi)$ function is assigned particularly when simulating an over-hygroscopic sorption process. Even when a fitting curve of the cup test results may be extrapolated into the over-hygroscopic range, the reliability remains uncertain (Dang et al. 2025c, 2025d). The impact of these errors is reported in Dang et al. 2025b.

$$K_v(P_c) = \left(\delta_v \cdot \frac{1-\frac{w}{w_{sat}}}{0.503\cdot\left(1-\frac{w}{w_{sat}}\right)^2+0.497}\right)\cdot\frac{\nabla P_c}{\nabla P_v} = \left(\frac{D_{va}}{\mu_{dry}R_vT}\cdot\frac{1-\frac{w}{w_{sat}}}{0.503\cdot\left(1-\frac{w}{w_{sat}}\right)^2+0.497}\right)\cdot\frac{P_v}{\rho_w R_v T} \tag{2.16}$$

$$K_l(P_c) = \left(\frac{\delta_a}{\mu(\varphi)}-\frac{\delta_a}{\mu_{dry}}\right)\cdot\frac{P_v}{\rho_w R_v T} \tag{2.17}$$

2.4 Implementation of boundary conditions

The exterior boundary conditions for moisture transfer mainly include vapor convection and WDR. For heat transfer, the primary boundary conditions are thermal convection, solar and long-wave radiation, and two components associated with moisture transfer: heat transfer due to vapor convection and sensible heat due to WDR (Janssen et al. 2007). These two thermal components and four hygric components are detailed in Eqs. 2.18 and 2.19. The interior boundary conditions are simpler, mainly involving thermal convection, long-wave radiation and vapor convection.

$$g_{es} = \beta_e \cdot \left(P_{v,e} - P_{v,es}\right) + R_{WDR} \tag{2.18}$$

$$q_{es} = \alpha_e \cdot (T_e - T_{es}) + q_{rad} + h_v \cdot \left[\beta_e \cdot \left(P_{v,e} - P_{v,es}\right)\right] + h_l \cdot R_{WDR} \tag{2.19}$$

where β [kg/(m²·s·Pa)] and α [W/(m²·K)] are surface moisture and heat transport coefficients; R_{WDR} [L/(m²·h)] is WDR load; subscripts e, es and rad refer to exterior air, exterior surface and radiation respectively.

There are no significant implementation differences in boundary conditions except for WDR. For instance, solar radiation in the two models is both calculated according to VDI Guideline 3789, with similar predefined absorptivity values for different surface conditions (Wufi-Wiki2; Fechner 2020b). Surface transport coefficients can either be arbitrarily entered or selected from the prescribed values in DELPHIN's interface. The implementation of surface heat transport coefficients α [W/(m²·K)] is similar, but surface moisture transport coefficients β [kg/(m²·s·Pa)] in WUFI are automatically derived from the α through the Lewis relation (Lewis 1922; Künzel 1995) (Eq. 2.20). In DELPHIN, β can be specified manually or calculated via the Lewis relation

(the conversion rate is 6.1×10^{-9} instead of 7×10^{-9} as applied by WUFI). WUFI can optionally account for wind dependency by assuming a simplified linear relationship with wind velocity U [m/s] (Eq. 2.21) and coefficients for windward $f_{windward}$ (from the direction perpendicular to the surface, or within ± 90° of this direction, default value: 1.6) or leeward conditions $f_{leeward}$ (from behind, default value: 0.33) in addition to convective and radiative heat transfer coefficients, α_{conv} and α_{rad} [W/(m²·K)].

$$\beta = 7 \times 10^{-9} \cdot \alpha_{conv} \tag{2.20}$$

$$\alpha_{overall} = \alpha_{conv} + \alpha_{rad} + f \cdot U \tag{2.21}$$

The WDR calculation in WUFI and DELPHIN relies on semi-empirical methods, specifically the "cosine projection method" (Blocken and Carmeliet 2006). The basic assumption is that raindrops of the same size, driven by horizontally homogeneous wind, strike an ideal vertical wall (Hoppestad 1955). WDR load R_{WDR} [L/(m²·h)] depends on wind velocity at standard meteorological height of 10 m, U_{10} [m/s], horizontal rain intensity R_{hor} [L/(m²·h)], the WDR coefficient α [s/m] and the angle θ [°] between the wind direction and the normal to the facade in a horizontal plane (Eq. 2.22). However, the WDR coefficient α [s/m] is formulated differently to account for spatial and topographical variations in subsequently developed standards (Blocken and Carmeliet 2010a). The ISO standard (ISO 15927-3, Eq. 2.23) and the ASHRAE standard (ASHRAE 160, Eq. 2.24) provide the two dominant semi-empirical methods, as implemented in DELPHIN and WUFI respectively. The ISO method adopts four correction factors to represent the WDR coefficient α [s/m] in Eq. 2.22, including the terrain surface roughness coefficient C_R [-], topography coefficient C_T [-], obstruction factor O [-] and wall factor W [-]. The AHSRAE method eliminates the power 0.88 of horizontal rain intensity and applies similar correction factors: the exposure factor F_E [-], deposition factor F_D [-] and an empirical constant F_L [kg·s/(m³·mm)]. An alternative (Eq. 2.25) is available in WUFI, using reduction factors R_1 and R_2, ranging from 0.05 to 0.2 s/m according to the building height and the position of the wall section, with recommended values pre-calculated in a computational fluid dynamics (CFD) benchmark (Karagiozis et al. 1997). Alternatively, users can input imposed fluxes directly in both models. Table 2.1 compares the five solutions for WDR calculation in WUFI and DELPHIN.

$$R_{WDR} = \boldsymbol{\alpha} \cdot U_{10} \cdot R_{hor}^{0.88} \cdot cos\theta \tag{2.22}$$

$$R_{WDR} = \left(\frac{2}{9} C_R \cdot C_T \cdot O \cdot W\right) \cdot U_{10} \cdot R_{hor}^{0.88} \cdot cos\theta \tag{2.23}$$

$$R_{WDR} = (F_E \cdot F_D \cdot F_L) \cdot U_{10} \cdot R_{hor} \cdot cos\theta \tag{2.24}$$

$$R_{WDR} = (R_1 + R_2 \cdot U) \cdot R_{hor} \cdot cos\theta \tag{2.25}$$

Table 2. 1 WDR calculation methods in WUFI and DELPHIN.

<table>
<tr><th></th><th>WUFI 1 (ASHRAE)</th><th>WUFI 2 (Alternative)</th><th>WUFI 3 (Imposed flux)</th><th>DELPHIN 1 (ISO)</th><th>DELPHIN 2 (Imposed flux)</th></tr>
<tr><td>Eq.</td><td>Eq. 2.24</td><td>Eq. 2.25</td><td>User-assigned</td><td>Eq. 2.23</td><td>User-assigned</td></tr>
<tr><td>Effective absorption</td><td colspan="2">Splashed raindrops are excluded by using an adhering fraction factor.</td><td colspan="2">Raindrops prevented by sheltering are excluded by using an exposure coefficient.</td><td></td></tr>
<tr><td>Vertical positions on the facades</td><td>-</td><td>-</td><td rowspan="4">Not applicable</td><td rowspan="2">Wall factor W</td><td rowspan="4">Not applicable</td></tr>
<tr><td>Building height</td><td rowspan="2">Exposure factor F_E and deposition factor F_D as correction coefficients depending on building heights and roof types</td><td>Location factor R_1 and R_2</td></tr>
<tr><td>Roof shape and slope</td><td>-</td><td>-</td></tr>
<tr><td>Adjacent obstacles and terrain types</td><td>Exposure factor F_E</td><td>-</td><td>Topography coefficient C_T, obstruction factor O, and terrain surface roughness coefficient C_R</td></tr>
</table>

Chapter 3 Quality assessment of HAM models

This chapter first describes the objectives and methodologies of quality assessment for heat, air and moisture (HAM) models. It subsequently reviews previous studies on assessing uncertainties related to the implementation of material properties and boundary conditions. For the former, the main limitation lies in the lack of representativeness in existing benchmarks (Dang et al. 2024b). For the latter, studies often overlook model-specific assumptions and simplifications, as well as the impact on the hygrothermal response predictions. These insights lay the foundation for introducing the advantages of the dedicated benchmark experimental datasets and the comprehensive methodology proposed in the subsequent chapters.

3.1 Scope and target of quality assessment

While HAM models have been extensively used to analyze the hygrothermal behavior of building components, their results can sometimes be inaccurate or incorrect. It is vital to comprehensively understand the strengths and limitations of these tools. To ensure accurate reproduction of mathematical equations and physical phenomena, significant efforts have been dedicated to verification and validation (V&V) processes (Cornick et al. 2009). Additionally, inter-model comparison and sensitivity analyses can be included as assessment approaches, as they also evaluate the predictive capabilities of HAM models. Verification aims to evaluate whether the governing equations of the physical model are correctly implemented. The typical approach is to compare simulation results with analytical solutions, as exemplified in EN 15026 (2004) and HAMSTAD Benchmark 2 (Adan et al. 2004; Hagentoft et al. 2004). Validation ensures that the model appropriately represents real-world physical phenomena. By using measured material properties and boundary conditions as inputs, the simulated results are compared against measured hygrothermal responses. A model is deemed reliable if it exhibits similar trends and only minor deviations. When mathematical or experimental results are unavailable, an alternative evaluation approach is inter-model comparison. Simulation results from different models serve as a form of “peer review”.

Some researchers classify this approach as part of verification (Cornick et al. 2009), but it should be considered independent, as uncertainties in both algorithms and implementations may contribute to the deviations. In addition, sensitivity analysis (e.g., on material properties) can indicate the model's robustness by showing how inputs affect outputs (Panico et al. 2023; Janssens et al. 2024; Vandemeulebroucke et al. 2023, 2024; Gan et al. 2025).

3.2 Previous quality assessment studies

The uncertainties in component-scale HAM modeling are primarily related to the implementation of material properties and boundary conditions. Previous quality assessment studies have mostly focused on the former under controlled boundary conditions, comparing simulation outcomes with experimental results or predictions from other models. The main limitation is the lack of representativeness in existing benchmark datasets or even the absence of such datasets (relying instead on pure inter-model comparison). Studies on the latter are relatively limited and typically involve only direct comparisons of the calculated wind-driven rain (WDR) using different methods, without analyzing their impact on hygrothermal predictions (Dang et al. 2024a).

There is currently no universally recognized standard for the comprehensive quality assessment of component-scale HAM models. Nevertheless, various benchmarks have been employed for experimental validation and inter-model comparison. Notable among these are the benchmarks of EN 15026 (2004) and of the HAMSTAD project (Adan et al. 2004; Hagentoft et al. 2004), which have been applied to test e.g., WUFI (2015), DELPHIN (Sontag et al. 2013) and COMSOL (Van Schijndel et al. 2016, 2017). However, these benchmarks always suffer from limitations. The primary issues include the small scale of employed configurations, which predominantly focus on "sample" scale rather than "component" or "building" scales (Colinart and Glouannec 2016), and the restricted diversity of materials, often limited to a single material or materials with similar hygric properties (Talukdar et al. 2007a; Rafidiarison et al. 2015; Salonvaara et al. 2020). Another limitation is the oversimplification of hygrothermal transport processes, even based on simple material characterization tests (James et al. 2010) rather than comprehensively long-term hygrothermal transport processes (Desta et al. 2011). Lastly, many datasets lack fully established and documented inputs and outputs, impairing the usability and applicability of the datasets and thus constraining the representativeness and broader utility of these benchmarks.

It is unrealistic to expect a single benchmark to evaluate all potential uncertainties in HAM models. A rigorous assessment process (Künzel and Karagiozis 2010) involves three key steps to assess: (I) the correct implementation of physical relationships through comparisons with analytical solutions (verification), (II) the correct reproduction of laboratory tests using well-characterized material data and boundary conditions (validation), and (III) the model's capability to simulate dynamic hygrothermal responses of building envelopes under real-world climate conditions (validation).

Table 3.1 summarizes the available dedicated benchmark datasets as reported in the references. The boundary conditions can be classified into "dynamic" (dynamic fluctuations including real climate data), "pulse" (square/ sine/ triangle/ sawtooth waves), and "fixed" (fixed constant values) by shapes and amplitudes, or categorized into "monitoring" (in- lab or in-situ) and "prescribed" (virtually assigned values) by generation approaches. The configurations are described from "exterior" (the cold side) to "interior" (the warm side). Nearly all available benchmarks are in-lab controlled conditions, as in-situ measurement is more challenging due to difficulties in regulating boundary conditions, deciphering construction quality and material characteristics, and the extended observation periods required to capture authentic responses. The limitations of the experimental datasets are classified as scale restrictions ("SR"), material monotony ("MM"), simplified hygrothermal processes ("SP") and incomplete documentation ("ID").

Table 3.2 summarizes recent assessment studies. The simulation results were compared with analytical solutions ("AS"), experimental datasets ("ED") and/or predictions from other models. The tick (√) and crossing (×) indicate whether a comparison exists or not, respectively. For studies lacking analytical solutions and experimental datasets, inter-model comparison is typically the only alternative. While such comparison can build confidence if consistent trends are observed, the absence of "correct answers" may obscure critical sources of deviation (Dang et al. 2023a, 2025a, 2025b). Most studies have focused on uncertainties related to the implementation of material properties, whereas the discrepancies from different calculation methods for boundary conditions remain insufficiently addressed, even when real climatic conditions are used in some studies.

Table 3. 1 Benchmark datasets for HAM model assessment reported in the references.

References	Boundary conditions		Configurations	Limitations
	Exterior	Interior		
HAMSTAD (Hagentoft et al. 2004)	Pulse & prescribed	Pulse & prescribed	Unspecified load-bearing material 100 mm + insulation 50 mm	MM, ID
	Fixed & prescribed	Fixed & prescribed	Unspecified material 200 mm	MM, ID
	Pulse & prescribed	Pulse & prescribed	Unspecified material 200 mm	MM, ID
	Pulse & prescribed	Pulse & prescribed	Unspecified load-bearing material 100 mm + insulation 20 mm	MM, ID
	Pulse & prescribed	Pulse & prescribed	Brick 365 mm + mortar 15 mm + insulation 40 mm	ID
EN 15026 (2004)	Fixed & prescribed	Fixed & prescribed	Unspecified semi-infinite material	MM, SP, ID
Talukdar et al. (2007a)	Pulse & monitoring	Pulse & monitoring	Spruce plywood 9 mm × 3 / cellulose Insulation 300 mm	MM, SP
James et al. (2010)	Pulse & monitoring	Pulse & monitoring	Gypsum board 12.5 mm × 3	MM, SP
Desta et al. (2011)	Dynamic & monitoring	Fixed & monitoring	Multiplex 18 mm + air cavity 25 mm + sheathing WF board 18 mm + insulation WF board 200 mm + finishing layer (= wooden board 12.5 mm/ or = VB + air cavity 25 mm + gypsum board 12.5 mm/ or = gypsum board 12.5 mm)	ID
Rafidiarison et al. (2015)	Pulse & monitoring	Pulse & monitoring	WF 80 mm/ WF 80 mm × 2/ lime plaster 7 mm + WF board 80 mm × 2/ lime plaster 7 mm + WF 80 mm × 2 + OSB 10 mm	MM
Ferroukhi et al. (2016)	Fixed & monitoring	Fixed & monitoring	Red brick 30 mm + expanded polystyrene 10 mm (or plaster 10 mm)/ or chipboard 30 mm + expanded polystyrene 10 mm (or plaster 10 mm)	SR, MM, SP

Table 3. 2 Quality assessment studies on uncertainties related to the implementation of material properties reported in the references.

References	Boundary conditions		Configurations	Comparisons with		
	Exterior	Interior		AS	ED	Other models
Künzel and Kiessl (1996)	Fixed & reference	Fixed & reference	Brick 240 mm + mortar 15 mm	×	√	WUFI
Budaiwi et al. (1999)	Fixed & monitoring	Fixed & monitoring	Outdoor film + gypsum board 10 mm + WF insulation 90 mm + WF board 10 mm + indoor film	×	√	Personal codes
Roels et al. (1999)	Pulse & monitoring	Pulse & monitoring	Composite roofs 420 - 790 mm with MW + fiber cement + perlite board/ or MW + wood wool cement (WWC) board + fiber cement/ or WWC board + perlite board + fiber cement/ or fiber cement + WWC board + perlite board	×	√	Personal codes
Nofal et al. (2001)	Dynamic & reference	Pulse & reference	Stucco 19 mm + building paper 0.2 mm + oriented strand board (OSB) 12 mm + spruce (bottom & top plate) 39 mm × 89 mm with glass fiber in stud space 89 mm + polyethylene sheet 0.2 mm + gypsum board 12 mm	×	×	DIM/ DELPHIN, hygIRC, MOIST and WUFI
Kalamees and Vinha (2003)	Pulse & monitoring	Pulse & monitoring	Boarding 22 mm + air gap 25 mm + wood fiber board 25 mm + insulation with air & vapor barrier (= mineral wool 173 mm with plastic sheet/ or = cellulose board 173 mm + bitumen paper/ or = sawdust 173 mm + bitumen paper) + gypsum board 13 mm	×	√	1D-HAM, MATCH and WUFI
HAMSTAD (Hagentoft et al. 2004)	Hagentoft et al. (2004)			√/ ×	×	Personal codes
Talukdar et al. (2007b)	Talukdar et al. (2007a)			√	√	Personal codes

Qin et al. (2009, 2010)	Fixed & monitoring	Fixed & monitoring	Masoned wall with sandstone and mortar 100 mm	×	√	Personal codes
Delgado et al. (2010)	Dynamic & reference	Fixed & reference	Acrylic stucco 5mm + extruded polystyrene (XPS) 40 mm + aerated concrete 200 mm + cement plaster & stucco 15 mm	×	×	hygIRC and WUFI
James et al. (2010)	James et al. (2010)			×	√	Personal codes
Steeman et al. (2010)	Pulse & monitoring	Pulse & monitoring	MW 95 mm with embedded plywood 15 mm + CS board 100 mm	×	√	BES-HAM personal codes
Van Belleghem et al. (2011)	Pulse & monitoring	Pulse & monitoring		×	√	CFD-HAM and BES-HAM personal codes
Guo et al. (2012)	Dynamic & monitoring	Fixed & monitoring	Cement mortar 20 mm + cement brick/XPS 240 mm + cement plaster 20 mm	×	√	Personal codes
Corcoran et al. (2013)	Dynamic & Reference	Pulse & Reference	brick 100 mm + air cavity 50 mm + insulation (= breather membrane + OSB 11 mm + MW 140 mm with vapor barrier + plasterboard 12.5 mm; or = breather membrane + MW 140 mm with vapor barrier + OSB 11 mm + plasterboard 12.5 mm; or = soft WF board 35 mm + WF board 140 mm + OSB 15 mm + service void 25 mm + plasterboard 12.5 mm)	×	×	DELPHIN and WUFI
Sassi et al. (2013)	Dynamic & monitoring	Fixed & Reference	Brick 90 mm + air gap 25 mm + spun bonded polyolefin (SBP) membrane 0.2mm + plywood 12.7 mm + fiberglass 140 mm + polyethylene membrane 1 mm + gypsum board 12.5 mm	×	×	HAM-Tools and WUFI
McClung et al. (2014)	Dynamic & monitoring	Fixed & monitoring	Fiber cement 16 mm + air gap 19 mm + MW/EPS 76 mm with moisture barrier + cross-laminated timber (CLT) panel 89 - 131 mm (with/without polyethylene) + stud space 89 - 131 mm + gypsum board 9.5 mm	×	√	WUFI

Carbonez et al. (2015)	Pulse & monitoring	Fixed & monitoring	Wood framed wall with OSB 12.7 mm + polyethylene oil & gypsum board 13 mm	×	√	DELPHIN and WUFI
Colinart et al. (2016), Colinart and Glouannec (2016)	Pulse & monitoring	Pulse & monitoring	Hemp concrete 360 mm with lime-sand plaster 10 mm & lime-hemp plaster as finishing layers	×	√	Personal codes
Ferroukhi et al. (2016)	Ferroukhi et al. (2016)			×	√	Personal codes
Alioua et al. (2019)	Dynamic & Reference	Dynamic & Reference	Concrete 150 mm	×	×	WUFI and COMSOL
Hejazi et al. (2019)	Dynamic & Reference	Fixed & Reference	Brick/ light concrete/ plaster 280 mm	×	×	DELPHIN and WUFI
Chung et al. (2020)	Dynamic & Reference	Fixed & Reference	Exterior cladding (= brick 92.08 mm + air gap 25 mm, or wood siding 9.53 mm + air gap 5 mm) + SBP membrane + plywood 15.88 mm + insulation 139.7 mm (= fiberglass or ccSPF) + vapor retarder + gypsum board 12.7 mm	×	×	HAM-Tools and WUFI
Dong et al. (2020)	Rafidiarison et al. (2015)			×	√	Personal codes
Salonvaara et al. (2020)	Fixed & monitoring	Fixed & monitoring	concrete masonry units + permeable water resistive barrier (WRB)/air barrier + XPS 38 mm + air gap 19 mm + gypsum board 12.5 mm / vinyl siding + air gap 19 mm + WRB+ structural insulated panel 108 mm+ gypsum board 12.5 mm + OSB 11 mm + expanded polystyrene (EPS)	×	√	WUFI
Asli et al. (2021)	Pulse & monitoring	Pulse & monitoring	WF board	×	√	Personal codes
Defo et al. (2022)	Dynamic & Reference	Pulse & Reference	Wood framed wall with stucco 19 mm/ brick veneer 90 mm/ WF board with vinyl coating on one major surface 10.5 mm/ vinyl 1.1 mm)	×	×	COMSOL, DELPHIN, hygIRC and WUFI
Schroderus et al. (2022)	Fixed & monitoring	Fixed & monitoring	Windshield 12 mm + MW 200 mm + air & vapor barrier 0.2 mm + MW 50 mm + gypsum board 13 mm	×	√	Personal codes

Amorim et al. (2024)	Fixed & monitoring	Fixed & monitoring	Solid brick 110 mm + MW 50 mm + gypsum board 12.5 mm / Silicate paint + finishing render 5 mm + insulating render 50 mm + solid brick 110 mm	×	√	WUFI

Some other studies examined the uncertainties associated with boundary conditions, particularly those of semi-empirical methods for wind-driven rain (WDR) calculation (Blocken et al. 2010b). These methods, while seemingly equivalent, exhibit varying degrees of accuracy under different scenarios. For instance, the ISO method works well for facades facing the prevailing wind direction, with observed discrepancies of less than 2 %; however, deviations can reach up to 60 % for those off the prevailing wind direction in complex urban settings (Souri et al. 2021). Some assumptions are questionable or even disproved. In the ISO method, wall factors W [-] of the center and the edge on the same height of the facade are assigned the same values, contradicting the uneven distribution of catch ratios (Blocken and Carmeliet 2004). In the ASHRAE method, variations in heights and horizontal positions are not considered. For instance, CFD simulation provides counterexamples for obstruction factor O [-], showing that upstream obstructions may also increase WDR loads, rather than only decrease them as given in ISO method (Blocken et al. 2009). Furthermore, the WDR coefficient α [s/m] may increase with horizontal rain intensity, while the dependency reproduced by CFD calculation remains absent in the ISO standard. Recent comparative studies evaluate the calculated WDR loads by the ASHRAE and ISO methods against measured datasets or CFD predictions. Chen et al. (2022) found that the ISO method underestimates by 0.5-0.8 times, while the ASHRAE method overestimates by 1.3-2.4 times. Zhou et al. (2023) reported that the cumulative annual WDR loads from both methods are several times larger than CFD results. Gholamalipour et al. (2022) argued that both semi-empirical models overestimate WDR loads by up to three times due to the limited incorporation of geometric configurations. Lu et al. (2023) found that catch ratios calculated by the ISO method fluctuate more and remain lower than the measured results, whereas the ASHRAE method provides more overestimations.

Notably, the differences among semi-empirical methods and specific assumptions and simplifications during their implementation into HAM models collectively contribute to deviations in WDR calculations (Defo et al. 2019; Chen et al. 2022; Lu et al. 2023; Zhou et al. 2023). However, these studies rarely address these additional assumptions and simplifications. For instance, WUFI

only allows assigning eight typical orientations (North, Northeast, East, etc.) instead of arbitrary angles. In DELPHIN, fixed "representative" values are assigned to the reduction factors (C_R = 1.007, C_T = 1.0, O = 0.8, and W = 0.4) instead of actual conditions (Fechner 2020a). An adhering fraction parameter is introduced to exclude splashing raindrops in WUFI. Default values for vertical walls and flat roofs are 0.7 and 1, respectively. An exposure coefficient (no more than 1; default: 1) can be assigned to consider the sheltering in DELPHIN, while the reduction factor appears only from the version DELPHIN 6.1.6.

Another deficiency lies in the inadequate consideration of predicted hygrothermal responses, which are influenced by both the differences among semi-empirical methods and the specific assumptions and simplifications during their implementation into HAM models. Only Defo et al. (2019) discussed the prediction of both WDR loads and hygrothermal responses of building facades based on the ASHRAE and ISO methods, where the ISO method is found to give more "conservative" results for both WDR loads and mold growth risks. However, it lacks experimental datasets as evidence.

In conclusion, previous HAM model assessments have limitations in their methodologies, benchmarks and the considered factors. Additionally, the impact of implementation uncertainties on simulated hygrothermal responses has not been adequately addressed. Therefore, this study adopts a stepwise strategy that incorporates experimental validation and inter-model comparison, leveraging dedicated in-lab and in-situ benchmark experimental datasets for a comprehensive assessment.

Chapter 4 Summary

This part revisited the formulations of governing equations and implementations of inputs in the two most common and commercially available models, WUFI and DELPHIN. It classified the determination approaches of material properties, boundary conditions and other inputs, and subsequently reviewed the main methodologies that may be associated with the quality assessment of HAM models, including verification, validation and inter-model comparison. Verification evaluates whether the governing equations are correctly implemented by comparing simulation outputs with analytical solutions. Validation, on the other hand, involves using real-world experimental data to determine if the model can reliably replicate observed phenomena under specified conditions. When experimental datasets are unavailable, inter-model comparison serves as an alternative. Additionally, incorporating sensitivity analysis can provide deeper insights into how input variables affect the output accuracy. This analysis also revealed limitations in current assessment practices. Existing benchmarks face challenges such as scale restrictions, material monotony, simplified hygrothermal processes and incomplete documentation. While inter-model comparison promotes “peer review” by identifying inconsistencies between results from different tools, it fails to address common deficiencies comprehensively. This thesis introduces a quality assessment scheme supported by stepwise benchmark datasets from controlled labs to real-world environments to enable both experimental validation and inter-model comparison.

Part II Under controlled boundary conditions

This part explores uncertainties in the implementation of hygrothermal material properties into heat, air and moisture (HAM) models and their impact on hygrothermal predictions. It first details the setup and results of an in-lab benchmark experiment conducted. Based on this experimental dataset, an extensive round robin validation campaign is executed to evaluate the reliability and robustness of various HAM models, focusing on the "correct" implementation of material properties and prediction of hygrothermal responses. Building on this, different strategies for implementing hygric properties into WUFI and DELPHIN are systematically assessed.

This part is largely based on Dang et al. (2023a, 2023b, 2024b, 2024c, 2025a, 2025b, 2025c, 2025d, 2026).

Chapter 5 The in-lab experimental setup and datasets

As outlined earlier, existing benchmark datasets often fall short in supporting comprehensive and systematic assessment of heat, air and moisture (HAM) models. Limitations include scale constraints, material uniformity, simplified hygrothermal processes and incomplete documentation. Since no single benchmark can capture all aspects of HAM modeling, a two-step approach is adopted in this thesis: one under controlled in-lab conditions and one under in-situ conditions, targeting uncertainties in material properties and boundary conditions, respectively. This chapter presents the in-lab experimental setup and related datasets (Dang et al. 2024b, 2024c), including the hot box–cold box (HB–CB) experiment, full-scale material characterization tests and measurements of surface transport coefficients.

5.1 The HB-CB experimental setup

An in-lab experiment on the transient hygrothermal responses of four wall assemblies is conducted in a dedicated HB-CB set-up — a climate chamber with controlled boundary conditions designed for hygrothermal studies at KU Leuven, Belgium (Langmans et al. 2012; Vereecken and Roels 2019) — serving as a benchmark for HAM model assessment (Dang et al. 2024b). As illustrated in Fig. 5.1, four wall assemblies (WA1 to WA4) comprise three insulation materials with different hygrothermal characteristics in different orders (Dang et al. 2023b): calcium silicate (CS) board, mineral wool (MW) and wood fiber (WF) board. WA1 consists of CS, MW and WF arranged from left to right, whereas WA2, WA3 and WA4 feature a different order of materials: WF, CS and MW. Aluminum-foil-based vapor barriers (VB) are attached at the left boundary and at the WF/CS interface in WA3 and WA4 respectively, to activate different moisture redistribution patterns. The dimensions of the insulation material layers are 0.6 m (width) × 0.6 m (height) × 0.1 m (thickness), except for the solely 0.1 mm thick VB. A schematic diagram of the setup (section view) is provided in Fig. 5.2, illustrating the connections and joints. Each material

layer is laterally glued to an extruded polystyrene (XPS) frame by polyurethane foam, with the XPS frame providing both structural support and thermal insulation. Rubber foam layers are added between layers to ensure airtightness. Each set of three material-XPS layer is peripherally fixed within a 2.4 m (width) × 2.4 m (height) × 0.31 m (depth) wooden framework and integrated into the rainbow-colored global test frame between the HB and CB. Given the dimensional ratios and lateral insulation, the hygrothermal transport is assumed to be one-dimensional.

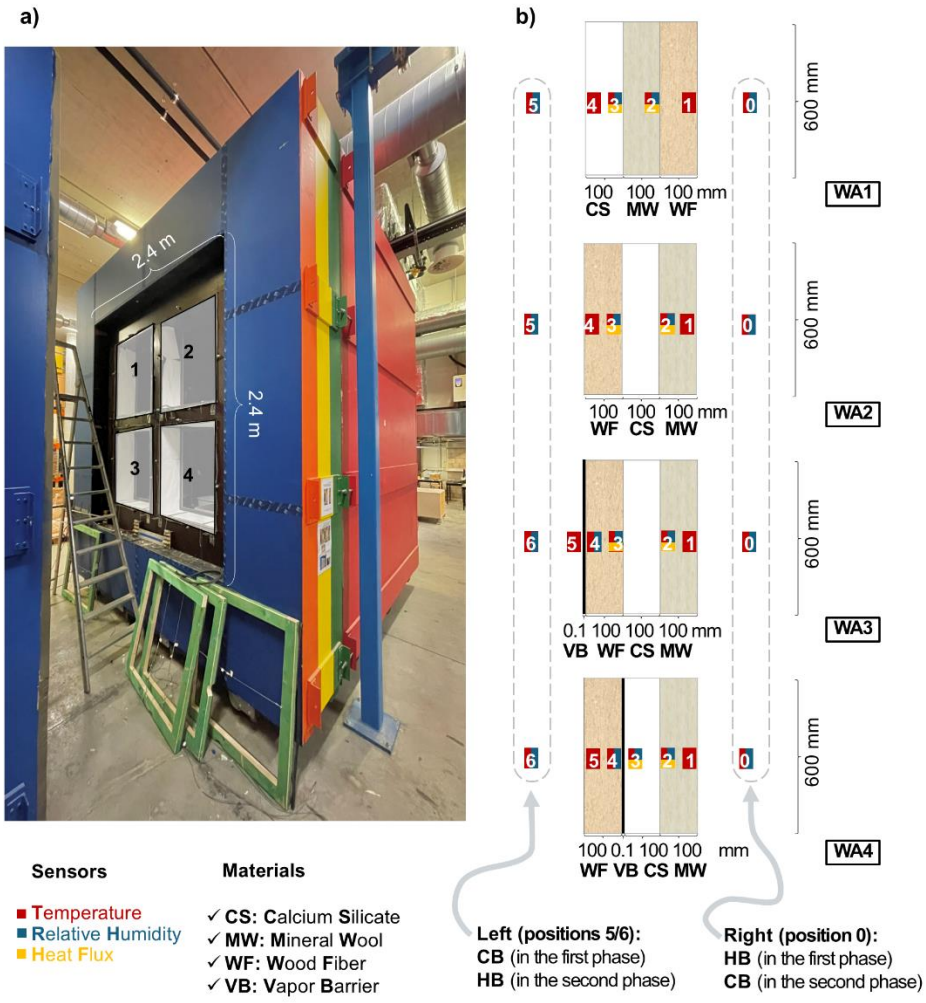


Fig. 5. 1 The HB-CB experiment: a) general setup, b) configurations of wall assemblies (WA1 to WA4) and sensor positions.

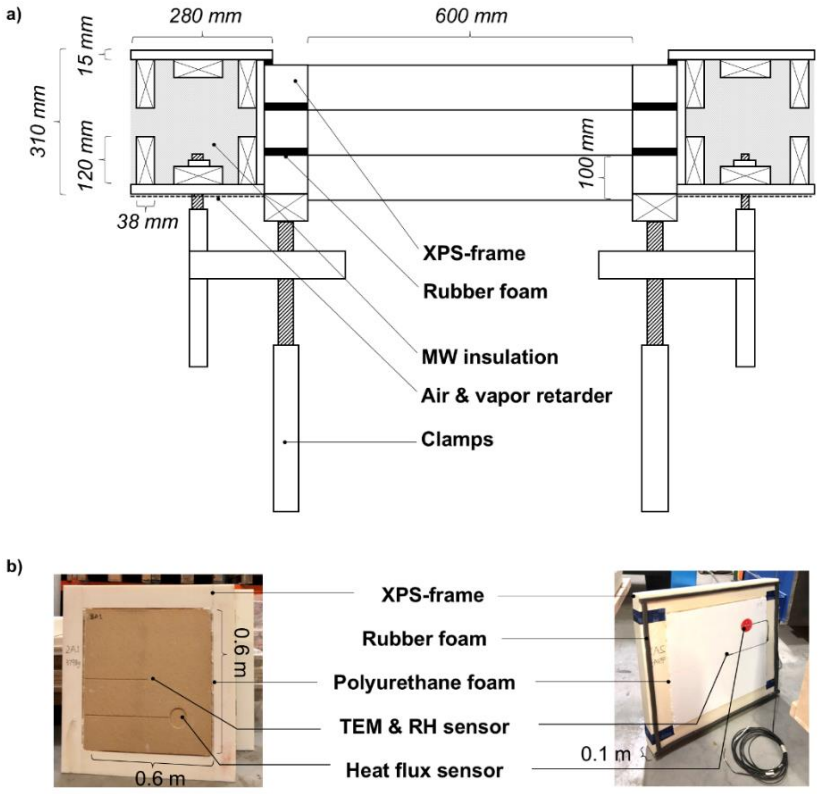


Fig. 5. 2 The HB-CB experimental setup: a) schematic diagram (section view) and b) composition of one layer of one wall assembly.

The calibrated HB and CB generate quasi-steady state boundary conditions (at positions 0 and 5/6, see Fig. 5.1b) at 2 °C & 80 % RH and 28 °C & 54 % RH respectively. After being stored at roughly 20 °C and 50 % RH for months, the samples are installed in the test frame and initially exposed to the HB on the right and CB on the left. The two boxes, and thus their boundary conditions, are switched in the 748th hour, in the middle of the overall 60-day (1440 h) experiment, to trigger different hygrothermal dynamics (see Fig. 5.3). Local temperature (T), relative humidity (RH) and heat flux (HF) are measured by calibrated sensors (Thermo-Electric Type T thermocouples with an accuracy of ± 0.2 °C, Honeywell HIH-4021 humidity sensors with an accuracy of ± 3.5 % RH, and Hukseflux HFP01 heat flux meters with an accuracy of ± 3 %) at the material surface or in the ambient air, while the material layers are detached and weighed every 7 to 10 days to determine their moisture masses (MM).

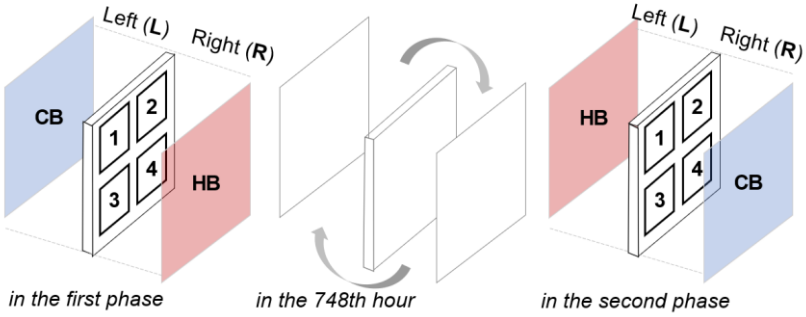


Fig. 5. 3 The scheme of boundary conditions in the HB-CB experiment.

Fig. 5.4 illustrates the whole procedure of the HB-CB experiment. First, a well-insulated wooden framework is constructed within the test frame placed between the HB and CB to avoid thermal bridges and to assure one dimensional hygrothermal transport in the normal direction of all wall assemblies (Fig. 5.4a). Bolts, brackets and slides are installed to maintain the structural integrity of the framework and ensure stable placement of the wall assemblies (Fig. 5.4b). An air tightness test is then performed to test the impermeability of the framework (Fig. 5.4c). Prior to testing, the material samples are stabilized under 20 °C and 50 % RH, with regular weighing until equilibrium is achieved (Fig. 5.4d). Grooves and thin openings are made on the sample surfaces and the enclosing XPS-frames, respectively, allowing the attachment and penetration of sensors and wires (Fig. 5.4e). All air gaps are sealed with polyurethane foam (Fig. 5.4f). Rubber foam is attached along the edges of the XPS-frames to ensure airtightness after integration (Fig. 5.4g). A close inspection (Fig. 5.4h) and air tightness test (Fig. 5.4i) confirm the absence of potential air gaps between layers. In the CB, four large ventilators create a uniform air flow (Fig. 5.4j). The HB, with a much larger size than the cold box, simulates an indoor environment with just a small ventilator to mix the air and regulate the relative humidity by oversaturated salt solution and stabilization via big CS boards (Fig. 5.4k). The HB's temperature is governed by an IR-bulb. The wall assemblies are then fixed by clamps to ensure a good connection between the layers and placed in the wooden framework, with power-on sensors connected to the monitoring device (Fig. 5.4l&m). As the monitoring starts, the HB-CB is closed by fixing bolts (Fig. 5.4n&o). The sample layers are regularly detached and weighed during temporary openings of the experimental setup and finally dried to determine their dry weights (Fig. 5.4p).

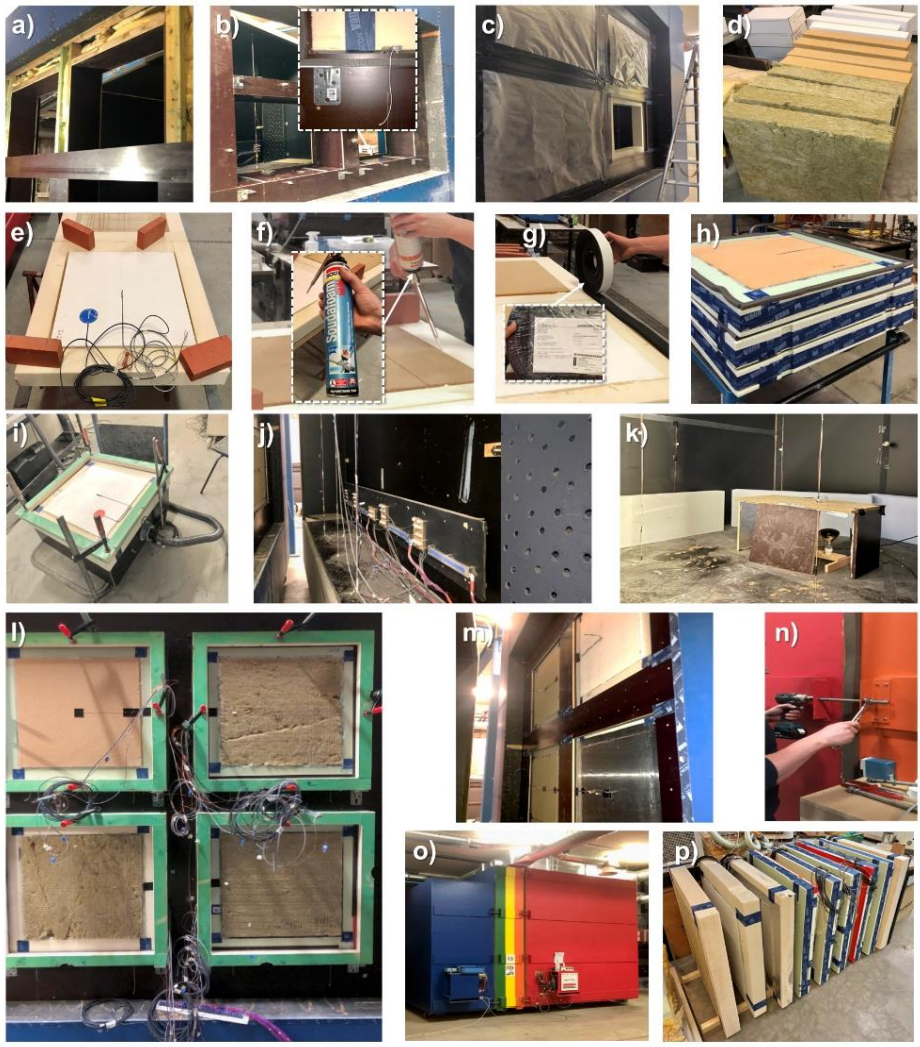


Fig. 5. 4 Procedures of HB-CB experiment: a) construction of insulated wooden framework, b) Installation of bolts, brackets and slides, c) air tightness test of the framework, d) sample preconditioning at 20 °C and 50 % RH, e) sensor and wire integration via grooves and openings, f) sealing air gaps with polyurethane foam, g) edge sealing with rubber foam, h) visual inspection of layer interfaces, i) final air tightness verification, j) setups in the CB, k) setups in the HB, l) & m) sensor activation and wall assembly placement, n) & o) closure of HB-CB setup with bolts, and p) sample weighing and drying for final mass determination.

As shown in Fig. 5.5, the measured boundary conditions remain generally consistent with the experimental settings. Although RH exhibits a certain degree of deviation, the temperature remains stable. Overall, the boundary conditions follow the intended trends, apart from disturbances caused by chamber openings during sample weighing.

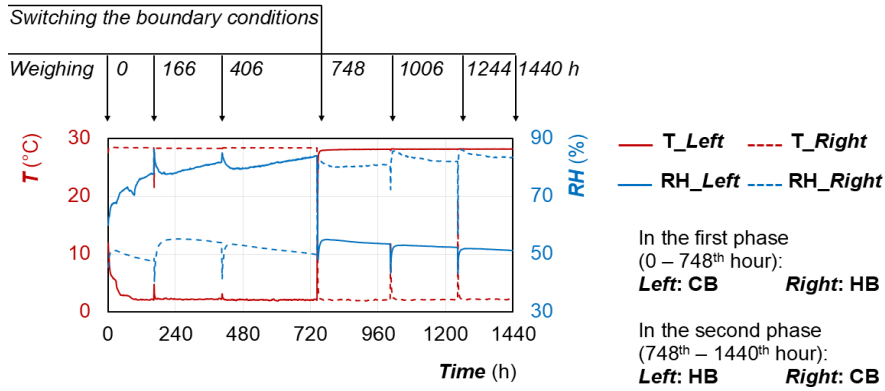


Fig. 5. 5 Measured boundary temperature and RH conditions of the HB-CB experiment.

5.2 Material characterization tests and results

To make the HB-CB experiment functional as validation test, a detailed characterization of the hygrothermal material properties is required. Hygrothermal properties of material samples (of the same batch) are measured via the: (I) steady-state thermal conductivity test, (II) vacuum saturation test, (III) gravimetric desiccator test, (IV) mercury intrusion porosimetry (MIP) test, (V) cup test, (VI) capillary absorption test. The experiment protocols are based on ISO 8301 (1991), ISO 10545-3 (2018), ISO 12571 (2021), ISO 15901-1 (2016), ISO 12572 (2016) and ISO 15148 (2002), while the experimental set-ups/methods are described in Van De Walle (2019) and Feng and Janssen (2021). Table 5.1 gathers the basic information of the tests and samples. Additional details are described as follows.

Test (I): the thermal conductivity λ [W/(m·K)] of dry and moist samples (moist samples stored at 97 % RH) is measured under three different steady-state boundary temperatures (5 and 15 °C; 15 and 25 °C; 25 and 35 °C).

Test (III): three duplicate samples of each material are placed in seven RH conditions regulated by saturated salt solutions (12 % RH: LiCl, 33 % RH: $MgCl_2 \cdot 6H_2O$, 53 % RH: $Mg(NO_3)_2 \cdot 6H_20$, 75 % RH: NaCl, 84 % RH: KCl, 94 % RH: KNO_3, and 97 % RH: K_2SO_4) (Greenspan 1977) at around 23 °C.

Test (IV): mercury intrusion is conducted assuming a surface tension of 0.485 N/m and a contact angle of 130° (Roels 2000).

Test (V): the temperature is maintained at around 23 °C, while RH conditions (in the cup/in the room) are governed by salt solutions (same as

described in test (III)): (1) CS and WF: 12 %/ 53 %, 76 %/ 53 %, 76 %/ 85 %, and 94 %/ 85 %, and (2) VB: 12 %/ 53 %, 53 %/ 85 %, and (3) 94 %/ 85 %. Two or three duplicate samples are used for each scenario due to limitations in the number of available experimental cups.

Test (VI): the moisture content w versus $\left(x/\sqrt{t}\right)$ profile of CS is determined via the ruler method (Evangelides et al. 2010, 2018; Ren et al. 2019). The data is used for calculating the moisture diffusivity D_w [m^2/s] via a Boltzmann transformation (Roels et al. 2003) that can be recalculated into a moisture permeability K_l [kg/(m·s·Pa)] (see Eqs. 2.13 and 2.15).

To address limited equipment availability and the stable nature of certain properties, tailored strategies are employed to ensure efficient characterization. For the liquid moisture transport properties, the ruler method is selected for its simplicity and reliable accuracy (Ren et al. 2019). Over-hygroscopic moisture storage is determined via the MIP test, which provides rapid results with acceptable precision (Feng and Janssen 2021). Additionally, several parameters, such as the specific heat capacity c [J/(kg·K)] of all materials, the density ρ [kg/m^3] and thermal conductivity λ [W/(m·K)] of VB and the vapor resistance factor μ [-] of MW, are assigned based on technical sheets.

Table 5. 1 Basic information of the samples used in the material characterization tests.

Tests	Obtained material properties	Dimensions (cm)	Sample numbers			
			CS	MW	WF	VB
(I) steady-state thermal conductivity test	$\lambda(\varphi)$ and $\lambda(T)$	26×26×3	2	2	2	-
(II) vacuum saturation test	ρ and w_{sat}	5×5×5	3	-	3	-
(III) gravimetric desiccator test	$w(\varphi)$	5×5×2	3×7	3×7	3×7	-
(IV) MIP test	$w(P_c)$ and Ψ	1×1×1	1	-	1	-
(V) cup test	$\mu(\varphi)$	26×26×10	3, 2, 2, 2	-	3, 2, 2, 2	-
		10×10×0.1	-	-	-	3, 3, 3
(VI) capillary absorption test	A_w and w_{cap}	10×10×10	3	-	3	-
	$w(\lambda)$ and $D_w(w)$			-	-	-

The measured (and referenced) single-valued and temperature- or moisture-dependent hygrothermal properties are shown in Table 5.2 and Figs. 5.6 & 5.7, respectively. In Table 5.2, standard deviations are indicated in brackets following the average values, while untested parameters are shown as underlined reference values derived from the technical sheets. The measured thermal conductivities at dry state, $\lambda_{dry}(T)$, and at 97 % RH, $\lambda_{\varphi=97\%}(T)$ are shown in Figs. 5.6a,c,e. The thermal conductivity $\lambda(T,\varphi)$ at specific T_0 [K] and φ_0 [%] can be read from a binary function (Eq. 5.1). Figs. 5.6b,d,f show the sorption isotherms $w(\varphi)$ obtained from the desiccator test, where sorption hysteresis is found to be insignificant for all materials. The moisture storage curve of MW is expected to increase linearly with RH, but slight fluctuations are observed — likely due to its low storage capacity, which makes it sensitive to minor handling or weighing deviations. Linear interpolation between stable low and high RH points is recommended, excluding irregular intermediate values. As shown in Figs. 5.7a&b, the moisture retention curve $w(P_c)$ translated from the sorption isotherm $w(\varphi)$ (obtained via the desiccator test) deviates from the MIP results. This mismatch reflects methodological differences and domain-specific limitations: desiccator test results in the hygroscopic range are considered more reliable than MIP data (Feng and Janssen 2021). In the over-hygroscopic range, MIP is generally effective, but its accuracy near the transition zone may be affected by limitations such as the ink-bottle effect and pore accessibility (Diamond 2000). Meanwhile, the measured saturation moisture content w_{sat} [kg/m^3], as a single-point measurement, is considered more accurate. To ensure continuity, the MIP-derived moisture retention curve is scaled vertically to ensure smooth alignment with the desiccator test results at low RH and the w_{sat} at high RH. Fig. 5.7c shows the measured vapor resistance factor μ [-] from the cup test, with irregular fluctuations observed in WF and VB. For WF, the values deviate from the expected monotonic decrease likely due to its sensitivity to RH changes. For VB, the extremely low vapor transmission renders the results highly sensitive to minor external influences such as surface contamination or handling moisture. To address these anomalies, two corrective strategies may be considered depending on the data pattern. If the overall trend is physically monotonic, the "linear interpolation" approach may be applied, excluding inconsistent intermediate data. Alternatively, if local deviations are minor and the curve remains largely flat, a constant value may be assumed. The moisture content w versus $\left(x/\sqrt{t}\right)$ profile of CS and the translated $D_w(w)$ curve are shown in Figs. 5.7d&e.

$$\lambda(T_0,\varphi_0)=\lambda_{dry}(T_0)+\varphi_0\cdot\frac{\lambda_{\varphi=97\%}(T_0)-\lambda_{dry}(T_0)}{(97\%-0\%)} \tag{5.1}$$

Table 5. 2 Measured (and referenced) single-valued hygrothermal material properties.

Material properties	CS	MW	WF	VB
c [J/(kg·K)]	1160	850	2100	900
λ_{dry} [W/(m·K)]	0.077	0.034	0.037	235
$\lambda_{\varphi=97\%}$ [W/(m·K)]	0.081	0.041	0.041	-
$w_{\varphi=80\%}$ [kg/m³]	5.76 (1.08)	0.38 (0.13)	10.17 (0.77)	-
w_{cap} [kg/m³]	864.92 (1.99)	-	55.32 (1.37)	-
w_{sat} [kg/m³]	891.48 (1.03)	-	925.02 (2.54)	-
A_w [kg/(m·s$^{0.5}$)]	1.04 (0.01)	-	0.02 (0.00)	-
μ_{dry} [-]	3.04 (0.11)	1.00	2.01 (0.03)	3.75×10^5 (2.62×10^5)
μ_{wet} [-]	1.76 (0.03)	-	2.12 (0.16)	2.59×10^5 (9.30×10^4)
ρ [kg/m³]	269.83 (2.27)	53.90(0.00)	101.40 (2.15)	2700
Ψ [-]	89.3	-	92.7	-

Note: Standard deviations are shown in brackets following the average values, while untested parameters are represented by underlined reference values.

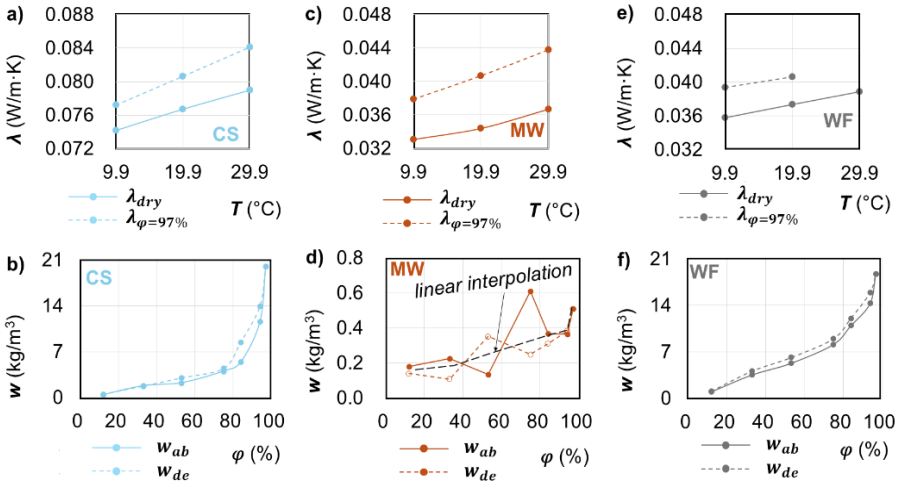


Fig. 5. 6 Measured temperature- or moisture-dependent hygrothermal material properties: a), c) and e) thermal conductivities at dry state, $\lambda_{dry}(T)$, and at 97 % RH, $\lambda_{\varphi=97\%}(T)$, and b), d) and f) sorption isotherms $w(\varphi)$.

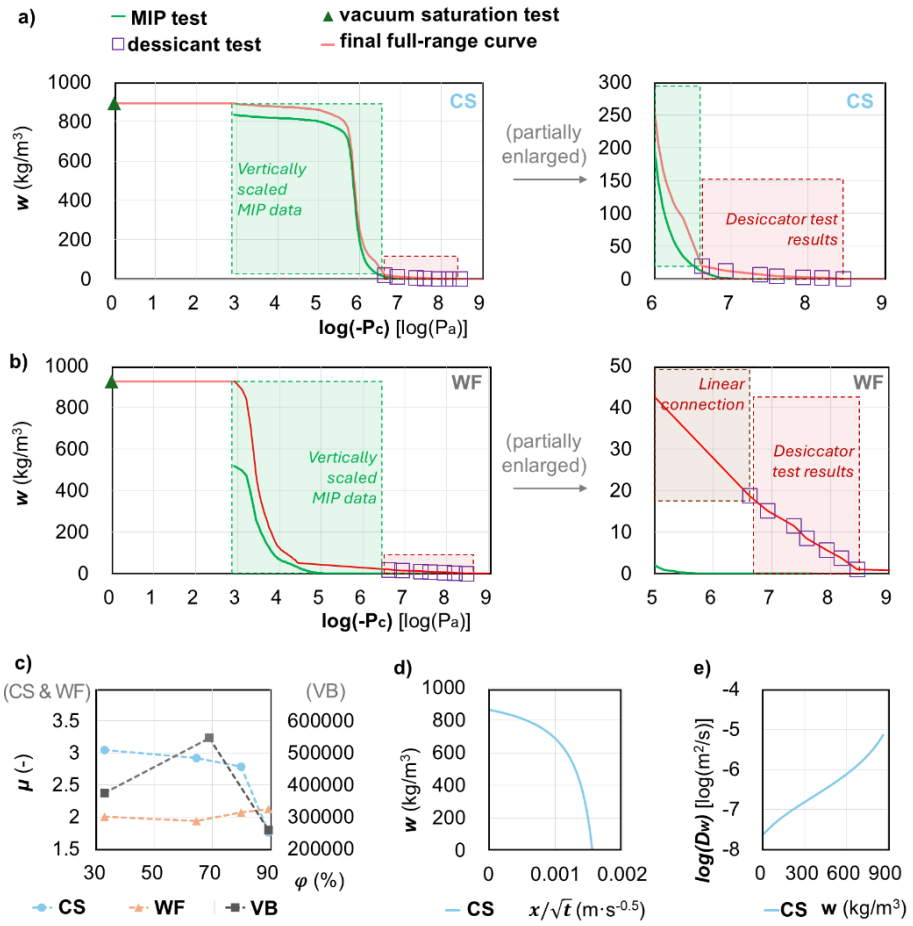


Fig. 5. 7 Measured temperature- or moisture-dependent hygrothermal material properties: a) – b) moisture retention curves $w(P_c)$ (the hygroscopic range is represented by desiccator test results, while the MIP data are used and vertically scaled only in the over-hygroscopic range to ensure smooth connections with adjacent curve segments), c) vapor resistance factors $\mu(\varphi)$, d) moisture content w versus $(x/\sqrt{t})$ profile and e) liquid diffusivity $D_w(w)$.

5.3 Surface transport coefficient measurement and results

Additional measurements are conducted to determine the surface transport coefficients in the HB and CB during the experiment. As shown in Fig. 5.8, four XPS boards containing eight capillary-saturated CS cylindric samples (diameter: 10 cm) are placed in the framework. Separate measurements are made for the HB and the CB, in which the frames are exposed to one climate chamber (HB or CB) on one side and the lab room on the other side. The CS

samples are well sealed except for the surface exposed to the HB or CB, where evaporation takes place. Heat and moisture transport through the two samples within each XPS board is assumed to be equivalent. Therefore, sensors are attached to one sample for monitoring temperature (position 1: surface, position 2: ambient air) and RH (position 2: ambient air), while the other sample is regularly weighed to determine the moisture loss. The temperature and relative humidity of the HB/CB and the lab room are set as 20 °C & 70 % RH and 20 °C & 50 % RH respectively. A linear relationship is observed between mass loss and time for all samples, confirming first-phase drying behavior from the saturated CS surfaces. Surface moisture transport coefficient β [kg/(m²·s·Pa)] is hence derived from Eq. 5.2. The vapor pressure at position 1 $P_v(T_1)$ is assumed to equal the saturation vapor pressure $P_{v,sat}(T_1)$. The total surface heat transport coefficient α_{tot} [W/(m²·K)] can be estimated with the Lewis relation (Kennedy et al. 2009) and ISO 6946, as shown in Eq. 5.3, where α_{rad} and α_{conv} [W/(m²·K)] are radiative and convective surface heat transport coefficient respectively.

$$\beta = \frac{g}{P_v(T_1) - P_v(T_2, \varphi_2)} = \frac{\frac{\Delta m}{\Delta t \cdot A}}{P_{v,sat}(T_1) - P_v(T_2, \varphi_2)} \tag{5.2}$$

$$\alpha_{tot} = \alpha_{rad} + \alpha_{conv} = 4.5 + \frac{\beta}{7.7 \times 10^{-9}} \tag{5.3}$$

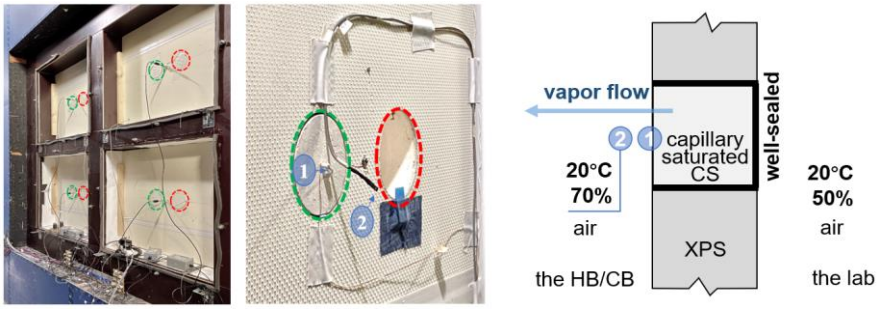


Fig. 5. 8 Experimental setup for surface transport coefficient measurements.

Table 5.3 presents the measured surface moisture transport coefficients β [kg/(m²·s·Pa)] and the derived surface heat convection coefficients α_{conv} [W/(m²·K)] allocated to the left and right of the four wall assemblies in the two phases, which are divided by the reorientation of the wall assemblies at the 748th hour, in the middle of the experiment.

Table 5. 3 Measured surface heat convection transport coefficients α_{conv} [W/(m²·K)] and surface moisture transport coefficients β [kg/(m²·s·Pa)].

In the first phase (0 – 748th hour) (left: the CB, right: the HB):

Wall assemblies	$\boldsymbol{\alpha_{conv}}$_left	$\boldsymbol{\beta}$_left	$\boldsymbol{\alpha_{conv}}$_right	$\boldsymbol{\beta}$_right
WA1	5.26	4.05×10^{-8}	3.56	2.74×10^{-8}
WA2	5.77	4.45×10^{-8}	4.48	3.45×10^{-8}
WA3	6.61	5.09×10^{-8}	3.30	2.54×10^{-8}
WA4	7.85	6.04×10^{-8}	5.85	4.51×10^{-8}
Avg.	6.37	4.91×10^{-8}	4.30	3.31×10^{-8}

In the second phase (748th - 1440th hour) (left: the HB, right: the CB):

Wall assemblies	$\boldsymbol{\alpha_{conv}}$_left	$\boldsymbol{\beta}$_left	$\boldsymbol{\alpha_{conv}}$_right	$\boldsymbol{\beta}$_right
WA1	4.48	3.45×10^{-8}	5.77	4.45×10^{-8}
WA2	3.56	2.74×10^{-8}	5.26	4.05×10^{-8}
WA3	5.85	4.51×10^{-8}	7.85	6.04×10^{-8}
WA4	3.30	2.54×10^{-8}	6.61	5.09×10^{-8}
Avg.	4.30	3.31×10^{-8}	6.37	4.91×10^{-8}

5.4 Measured hygrothermal responses and validity assessment

The hygrothermal responses of the four wall assemblies are shown in Figs. 5.9 – 5.12. While there are periods in which the data are not complete (RH2 of WA2) or out of the reliable scope (RH3 of WA1, RH4 of WA3, RH3 and RH 4 of WA4: the data exceeds 100 % and is corrected to 100 %), the overall hygrothermal conditions can be estimated. In general, all wall assemblies absorb moisture from the right side, as the vapor pressure in the HB is higher in the first phase. Water vapor penetrates the different material layers with different moisture storage capacities and may be buffered by the hygroscopic materials or blocked by the vapor barrier. When the boundary conditions are switched, the absorbing and drying processes are reversed accordingly.

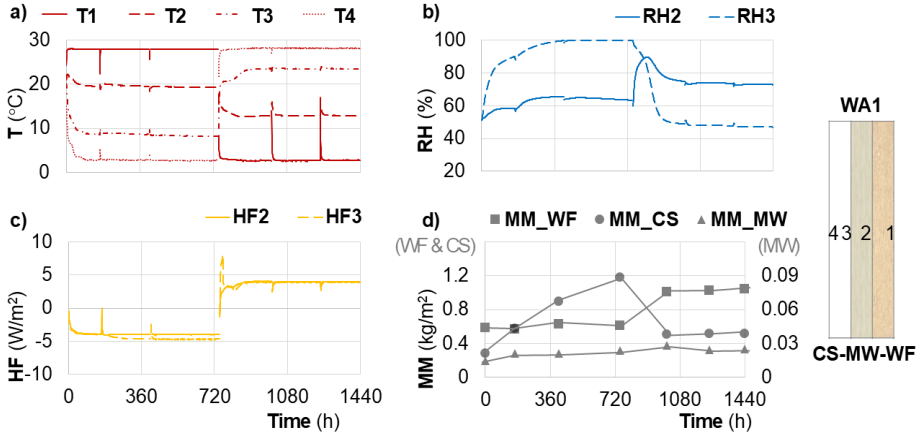


Fig. 5. 9 Measured hygrothermal responses of WA1: a) temperatures: T1- T4, b) relative humidity: RH2 – RH3, c) heat fluxes: HF2- HF3 and d) moisture masses: of WF, CS and MW.

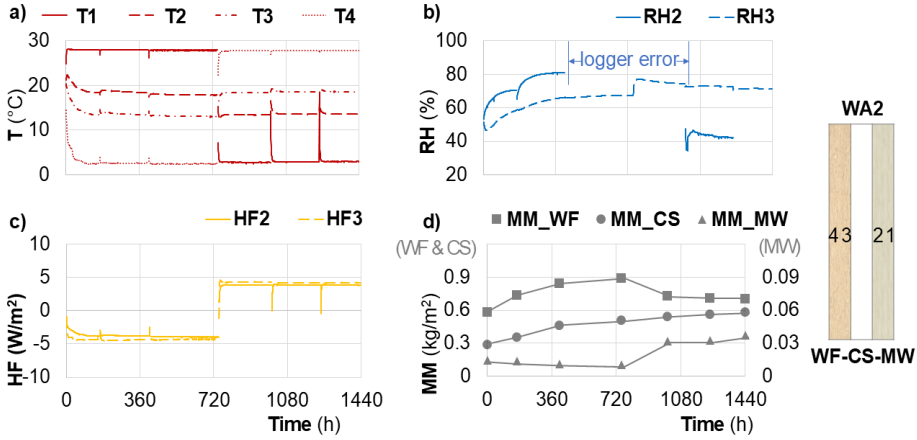


Fig. 5. 10 Measured hygrothermal responses of WA2: a) temperatures: T1- T4, b) relative humidity: RH2 – RH3, c) heat fluxes: HF2- HF3 and d) moisture masses: of WF, CS and MW.

To examine the consistency and integrity of the measured dataset, two HAM models, WUFI and DELPHIN, are used to simulate the hygrothermal responses of the four wall assemblies, incorporating the measured material properties, surface transport coefficients and boundary conditions as inputs. The comparison between simulated and measured hygrothermal responses offers mutual insight into experimental and modeling uncertainties.

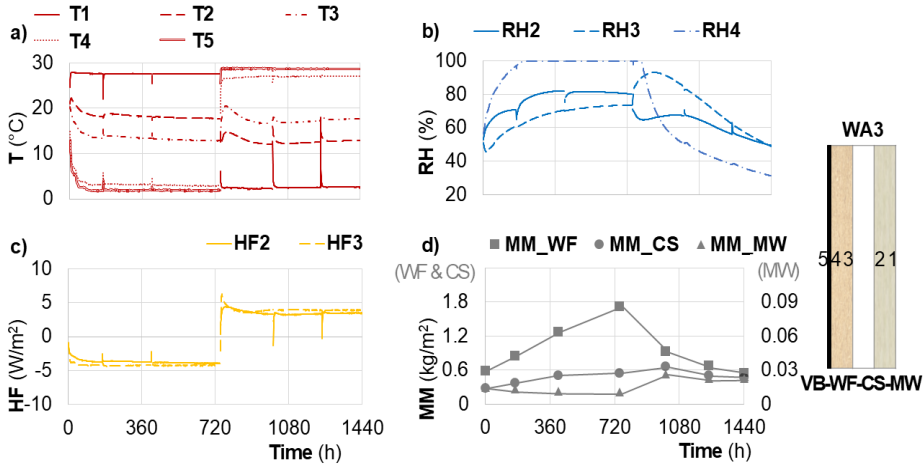


Fig. 5. 11 Measured hygrothermal responses of WA3: a) temperatures: T1- T5, b) relative humidity: RH2 – RH4, c) heat fluxes: HF2- HF3 and d) moisture masses: of WF, CS and MW.

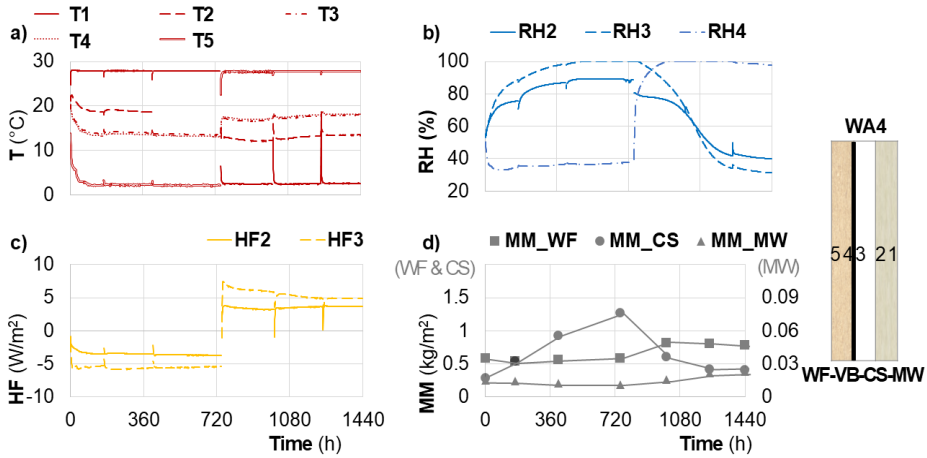


Fig. 5. 12 Measured hygrothermal responses of WA4: a) temperatures: T1- T5, b) relative humidity: RH2 – RH4, c) heat fluxes: HF2- HF3 and d) moisture masses: of WF, CS and MW.

Fig. 5.13 compares the measured and simulated hygrothermal responses of WA1. Temperature predictions show good agreement with the measurement data, with deviations generally within ± 2 °C, while RH discrepancies are slightly larger, typically within ± 10%. These deviations may stem sensor inaccuracies (see Section 5.1), but more critically from uncertainties in material property inputs that affect the reproduction of hygrothermal transport processes. For heat flux, WUFI results align closely with measurement results, whereas DELPHIN exhibits a persistent deviation of approximately 2.5 W/m^2, likely due to model-specific settings. Moisture mass predictions vary by material: WF shows the best overall agreement; CS agrees well initially but diverges

particularly in the second phase, with deviations up to 0.25 kg/m^2; MW achieves better agreement in the second phase and early-stage deviations reaching 0.01 kg/m^2. Except for heat flux, the two models produce overall consistent results, even when both deviate from measurements, indicating that discrepancies arise more from experimental uncertainties and operator effects than from model differences. These include sensor drift, manual handling and calibration issues — for example, some RH values exceeding 100 % that require manual correction. In the absence of a definitive "ground truth", inter-model comparison offers a valuable complementary perspective. This pattern of model agreement with localized deviations is observed across all assemblies, though not detailed here for brevity (Dang et al. 2025b, 2025c). The next chapter will further explore whether these discrepancies can be attributed to inherent model differences or user-induced variability.

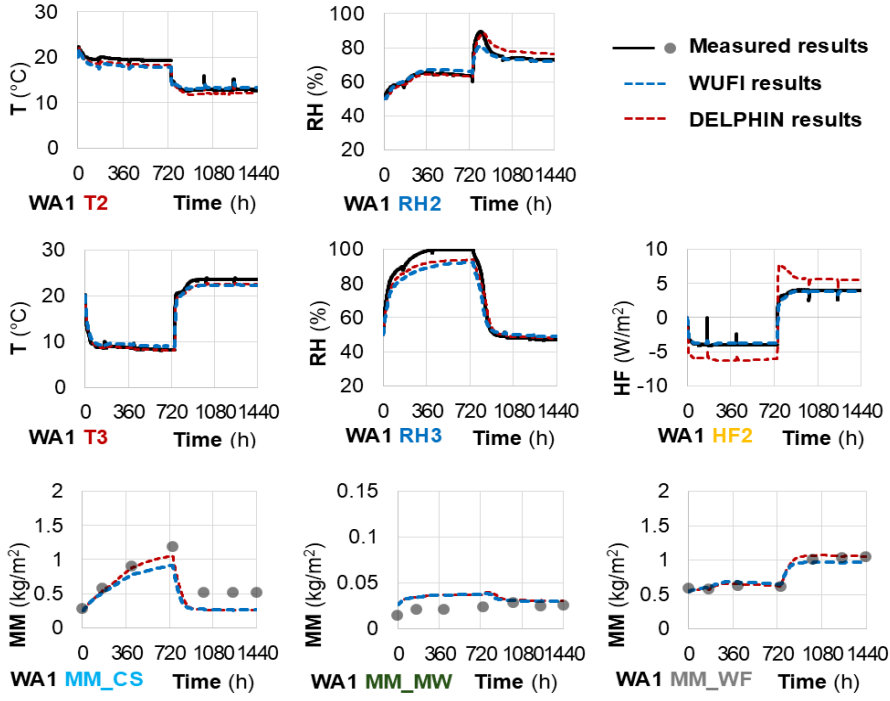


Fig. 5. 13 Comparison between measured and simulated hygrothermal responses of WA1: temperatures: T2- T3, relative humidity: RH2 – RH3, c) heat fluxes: HF2 and d) moisture masses: of WF, CS and MW.

Chapter 6 Extensive round robin validation campaign

This chapter presents the outcomes and insights from a state-of-the-art round robin validation campaign titled "*Empirical validation of HAM-models based on a dedicated HB-CB experiment*" (Dang et al. 2025b) aiming to evaluate the robustness and reliability of heat, air and moisture (HAM) models in predicting one-dimensional hygrothermal responses of building components under controlled boundary conditions. The in-lab benchmark experimental datasets, detailed in the previous chapter, have been reproduced by over 70 contributors in 38 participating groups from 19 countries using various HAM models. This cooperation builds upon prior efforts in the HAMSTAD project (Adan et al. 2004; Hagentoft et al. 2004), adding significant values to HAM model assessment. This chapter involves the methodology and project overview, comparisons of hygrothermal response predictions across different stages and models, and an impact analysis of implemented material properties on the simulated hygrothermal responses. The approach integrates experimental validation with inter-model comparison, combining correlation analysis to provide recommendations for improving the simulation accuracy.

6.1 Project overview and methodology

6.1.1 Research scheme

The assessment based on the in-lab dataset primarily focuses on the implementation of hygrothermal material properties while controlling other variables (e.g., uniform samples with minimal boundary effects, simple and quasi-steady-state boundary conditions, measured surface transport coefficients, etc.) as much as possible. Even then though, the allocation of noted deviations remains complex. The main uncertainties stem from both experimental limitations and the processing of material properties, particularly those that cannot be directly measured and must be inferred or transformed

from experimental data. Experimental errors are treated as systematic, while the focus lies on evaluating modeling risks through stepwise assessment.

For a more explicit analysis thus, a stepwise protocol is developed. **The first stage** is based on an "engineering perspective". Instead of providing measured material properties, only basic parameters from technical sheets are given (the claimed values of density ρ [kg/m^3], thermal conductivity λ [W/(m·K)], specific heat capacity c [J/(kg·K)], vapor diffusion resistance factor μ [-] and capillary absorption coefficient A_w [kg/(m·s$^{0.5}$)]). The "engineers" can either directly select material entries from the built-in databases of HAM models or create their own material files. The measured boundary temperature and relative humidity (RH) conditions and estimated initial conditions (20 °C and 50 % RH: the lab room conditions at which the samples have been stored for months before the experiment) are provided. The description for surface transport is limited to "*the HB, whose size is much larger than the cold box, simulates an indoor environment with just a small ventilator to mix the air, while the CB simulates the outdoor environment with four large ventilators creating a uniform air flow along the building component*", and therefore the assignment can be based on standards or experience. **The second stage** takes a more academic view. In addition to the initial and boundary conditions defined in the first stage, raw data points of measured material properties and surface transport coefficients are provided for conversion into model-compatible formats (Dang et al. 2024b, 2024c). Although uncertainties remain in the translation, deviations are expected to be reduced since the newly provided measured datasets are used as inputs. **The third stage** finally is an extra chance for participants who intend to fine-tune the implementations of material properties (mainly), algorithms (if applicable, particularly within personal codes) and other factors. The information and data provided in the previous stages are carried forward. The measured hygrothermal responses as well as simulation results from other groups in stages 1 and 2 are supplemented as references. These references enable participants to detect and adjust inappropriate settings through comparison and iterative refinement. Table 6.1 shows the data series provided (as inputs) to and required (as outputs) from the contributors over the three stages. The ticks (√), circles (O) and crossings (×) indicate "fully provided/ required for submission", "limited information provided/ optional for submission" and "not given", respectively. Simulated hygrothermal responses, including temperature (T), relative humidity (RH) and heat flux (HF) at interfaces and moisture mass (MM) of each material layer (see Fig. 5.1b), are collected in time series for comparison.

Table 6. 1 Data series provided (as inputs) and collected (as outputs).

Data series		Stage 1	Stage 2	Stage 3
Inputs (provided by the coordinator)	Initial conditions	√	√	√
	Boundary conditions	√	√	√
	Surface transport coefficients	O	√	√
	Material characteristics	O	√	√
	Hygrothermal responses	×	×	√
Outputs (collected from the participants)	Surface transport coefficients	O	√	√
	Material characteristics	√	√	√
	Hygrothermal responses	√	√	√

Note: Raw measurement data are provided in Excel sheets, while output results are collected using standardized Excel templates. Participants using WUFI and DELPHIN are additionally required to submit the corresponding standard material property files. The ticks (√), circles (O), and crossings (×) indicate "fully provided/ required for submission", "limited information provided/ optional for submission", and "not given", respectively.

6.1.2 Participation overview

This project received no direct funding, so all participants contributed voluntarily. The registration started in February 2023, initially attracting 55 groups from 22 countries. As Fig. 6.1a) shows, the actual participation (in at least one stage of the tasks) involves 38 groups from 19 countries (for cross-national groups, the number only counts 1/N for each country, N = number of the countries): Austria (AT), Australia (AU), Belgium (BE), Brazil (BR), Canada (CA), China (CN), Czech Republic (CZ), Germany (DE), Denmark (DK), Estonia (EE), Finland (FI), France (FR), Hungary (HU), Japan (JP), the Netherlands (NL), Portugal (PT), Slovakia (SK), the United Kingdom (UK), and the United States (US). Groups may submit multiple results (from different models, or using different implementation approaches, or by different persons). Each submission result is denoted by the group number (as assigned after the registration) and a letter (to distinguish different results from one group). The entire process remains anonymous. KU Leuven (BE), as the institutional coordinator, was responsible for task distribution, result collection and data analysis. Fig. 6.1b additionally illustrates the proportion of the employed models in the three stages. Two commercial models, WUFI and DELPHIN, are the primary choices. Additionally, about one-third of the submissions employ custom-built models

developed using various programming languages and software platforms, such as COMSOL, MATLAB, Fortran and Python.



Fig. 6. 1 Participation overview: a) numbers of groups and b) numbers of submissions and employed HAM models.

6.1.3 Performance indicators

In addition to plotting the results in line charts, two statistical indices, the normalized root-mean-square-error (NRMSE) and Pearson correlation coefficient (r), are employed to quantify the deviations and correlations between the simulated and measured datasets as heat maps. These two metrics are complementary: NRMSE captures the magnitude of absolute deviations, while r reflects the consistency of temporal trends. Using both allows for a more comprehensive assessment of model performance, distinguishing cases where the simulation matches the overall pattern but deviates in magnitude, or vice versa. The root-mean-square-error (RMSE) describes the average absolute error of differences between simulated and measured values, but this value is sensitive to the variation amplitudes. Therefore, its adapted form, normalized root-mean-square-error (see Eq. 6.1) is employed to avoid misinterpretation and to ensure the same order of magnitude (Chakraborty and Elzarka 2018) across the variables. There is no standardized value for the NRMSE, but suggested thresholds for RMSE are 1 or 2 (for temperature) and 2 or 5 (for RH)

for “high” or “low” accuracy, respectively (Huerto-Cardenas et al. 2020). The *r* (see Eq. 6.2) indicates the strength of a linear relationship between two data series, ranging from -1 (opposite trend) to +1 (similar trend). A near-zero value indicates no relation. There is no fixed threshold, but suggested values for building behavior are reported in literature, for instance, $r > 0.5$ (Paolo 2013) or its square $r^2 > 0.75$ (ANSI/ASHRAE Guideline 14-2002). As both indices require the same quantities in the paired data series, only non-null values are included for their calculation (since some measured data are missing, for instance, due to logger errors).

$$NRMSE = \frac{1}{m_{max} - m_{min}} \cdot \sqrt{\frac{\sum_{i=1}^{n}(m_i - s_i)^2}{n}} \tag{6.1}$$

$$r = \frac{\sum_{i=1}^{n}[(m_i - \bar{m}) \cdot (s_i - \bar{s})]}{\sqrt{\sum_{i=1}^{n}(m_i - \bar{m})^2} \cdot \sqrt{\sum_{i=1}^{n}(s_i - \bar{s})^2}} \tag{6.2}$$

where, i and n are the ordinal number and amount of the entries within one data series; m and s are the measured and simulated data; max and min are the maximum and minimum.

6.2 Overall assessment

The simulated hygrothermal responses of WA1 and WA4 are compared with the measured datasets using line charts in Figs. 6.2-6.7 (see Fig. 5.1b for details of the four wall assemblies, WA1 – WA4, and the sensor positions). These two wall assemblies are selected because most participants set the minimal deviations in WA1 as the optimization criteria for fine-tuning in stage 3 while WA4 is representative for the other three wall assemblies, given its similar material order and the vapor barrier that makes the moisture transport more complex. To highlight the impact of the adjusted implementations, results from those groups who did not participate in all three stages are temporarily removed. Heat maps in Figs. 6.8 and 6.9 depict the NRMSE and *r* between simulated and measured hygrothermal responses of the four wall assemblies in each of the three assessment stages. In each subgraph, each vertical grid corresponds to a different submission, which are grouped into three categories according to the employed models (DELPHIN, WUFI and others). A star (“*”) is assigned to empty boxes where submitted data are missing, while an additional hyphen (“-”) is marked in boxes with negative *r* values. As explained previously, a small NRMSE and a large *r* value (“bluer” boxes) indicates a good agreement between measurement and simulation. Note that, three groups (using WUFI) only present the results of WA1 in stage 3, purely

focusing on enhancing the predictive accuracy for this specific wall assembly through adjustments in their implementations.

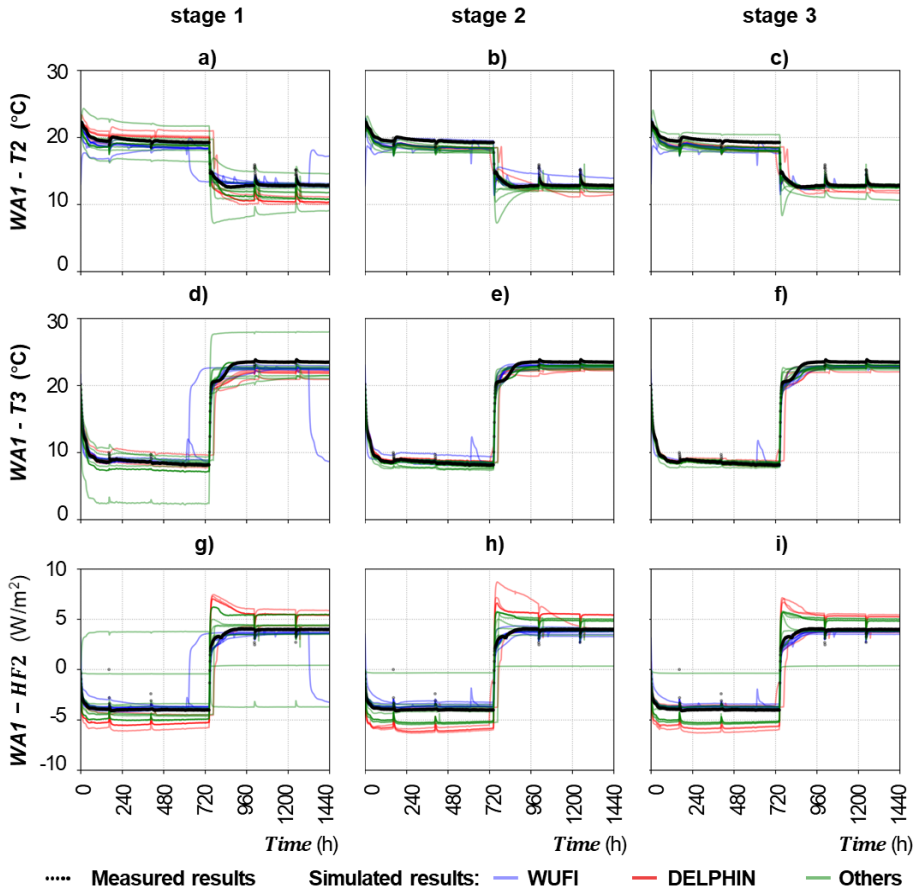


Fig. 6. 2 Simulated temperatures and heat fluxes of WA1: a) – c) T2, d) - f) T3 and g) - i) HF2.

There is a clear trend that the agreement between measurement and simulation increases from stage 1 over stage 2 to stage 3, observable from a horizontal view in Figs. 6.2-6.9. In stage 1, the flexibility to generate or select material properties and surface transport coefficients yields disparity in the NRMSE of the hygrothermal predictions (Fig. 6.8, left column) (Dang et al. 2025a). Even so, most outputs are in good correlation with the measured datasets, except for *r* of the moisture masses (MM) of CS and MW (see Fig. 6.9, left column). In stages 2 and 3, implementing the measured material properties as inputs effectively reduces the divergences. This optimization effect is more pronounced in heat-related variables (T and HF) than in moisture-related variables (RH and MM). In stage 3, nearly all heat-related variables

satisfy the criteria NRMSE < 0.1 and r > 0.5. On the other hand, the moisture-related variables, particularly for MM of MW, remain roughly uncorrelated, although RH predictions are improved. Complementarily, WUFI results are slightly better in line with the measured data than the outcomes from DELPHIN and other models. The moisture-related responses express larger deviations, but an overall trend agreement is achieved. The calculated MM of CS are obviously piled into two model categories in stage 1: DELPHIN results (red curves) and WUFI results (blue curves) concentrate at different values, while the results from other models have a larger spectrum. Since this distinction is not obvious in the RH courses, the limited material entries in the databases and/or similarity of their properties are presumably the primary reasons (Figs. 6.4a and 6.7d). As measured material properties are provided in stage 2, the agreement in most MM of CS and WF (Figs. 6.4b,c,h,i, and 6.7b,c,e,f) are improved, while there are still mismatches between the calculated and measured MM of MW (Figs. 6.4e&f and 6.7h&i).

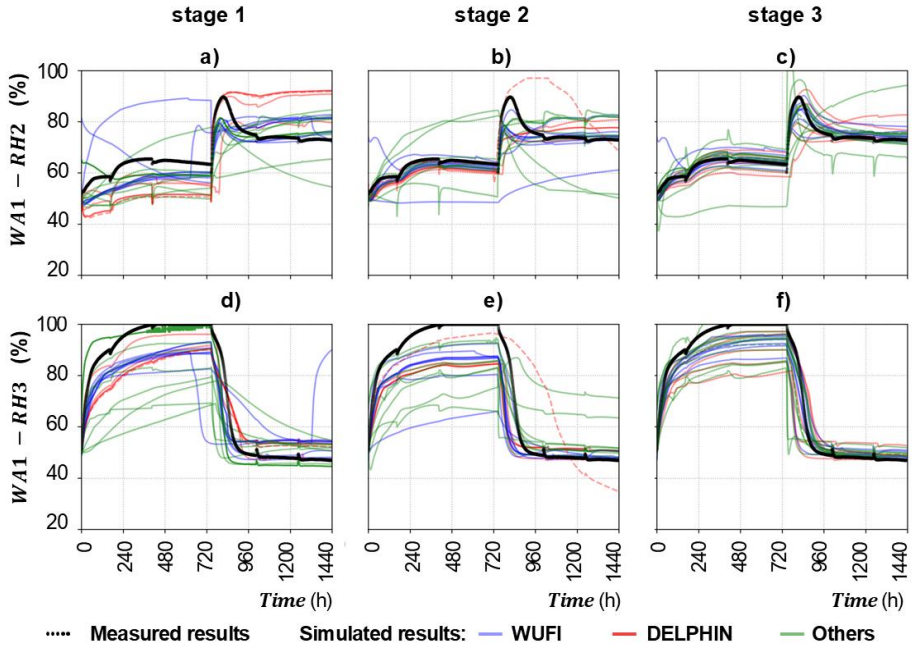


Fig. 6. 3 Simulated relative humidity of WA1: a) – c) RH2, and d) – f) RH3.

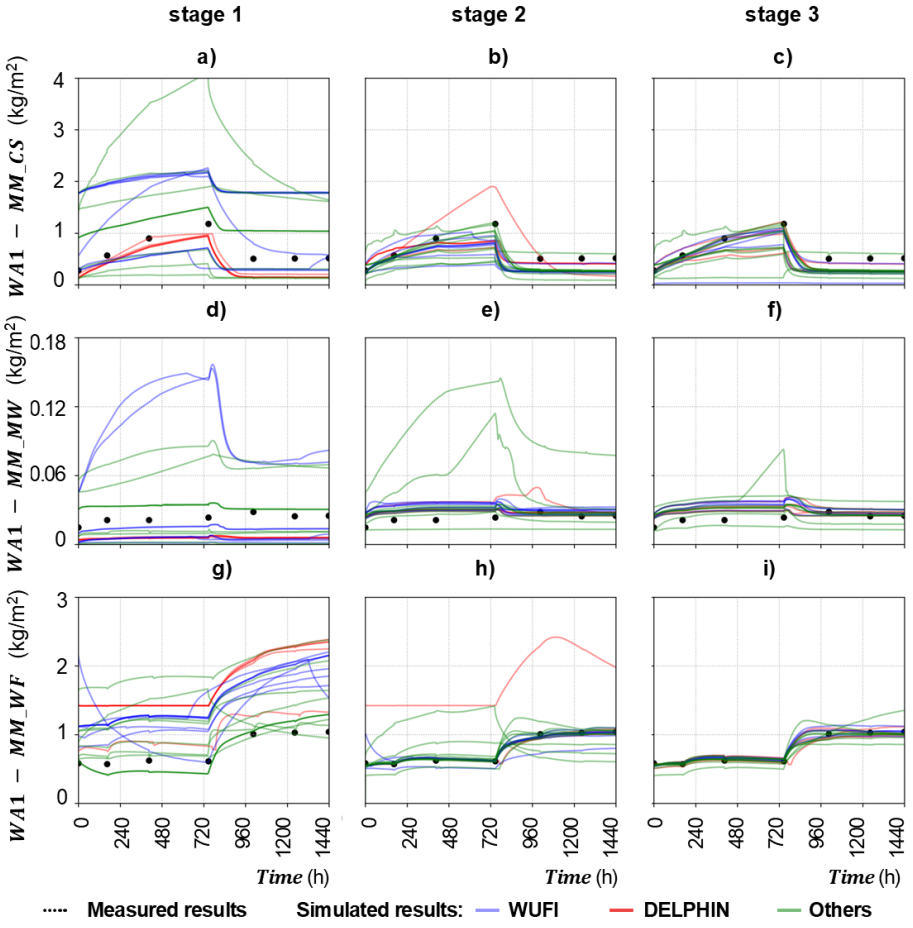


Fig. 6. 4 Simulated moisture masses in WA1: a) – c) of CS, d) – f) of MW, and g) – i) of WF.

Given that RH is highly sensitive to moisture exchange with adjacent materials and ambient air, the more accurate implementation of material properties in stage 2 relative to stage 1 is expected to reduce the deviations between simulated and measured results. However, some RH predictions remain unchanged or become worse, presumably due to user impact. This is proven by the results calculated by fine-tuned models in stage 3, as errors in earlier stage might be corrected (Figs. 6.3b,c,e,f and 6.6b,c,e,f,h,i).

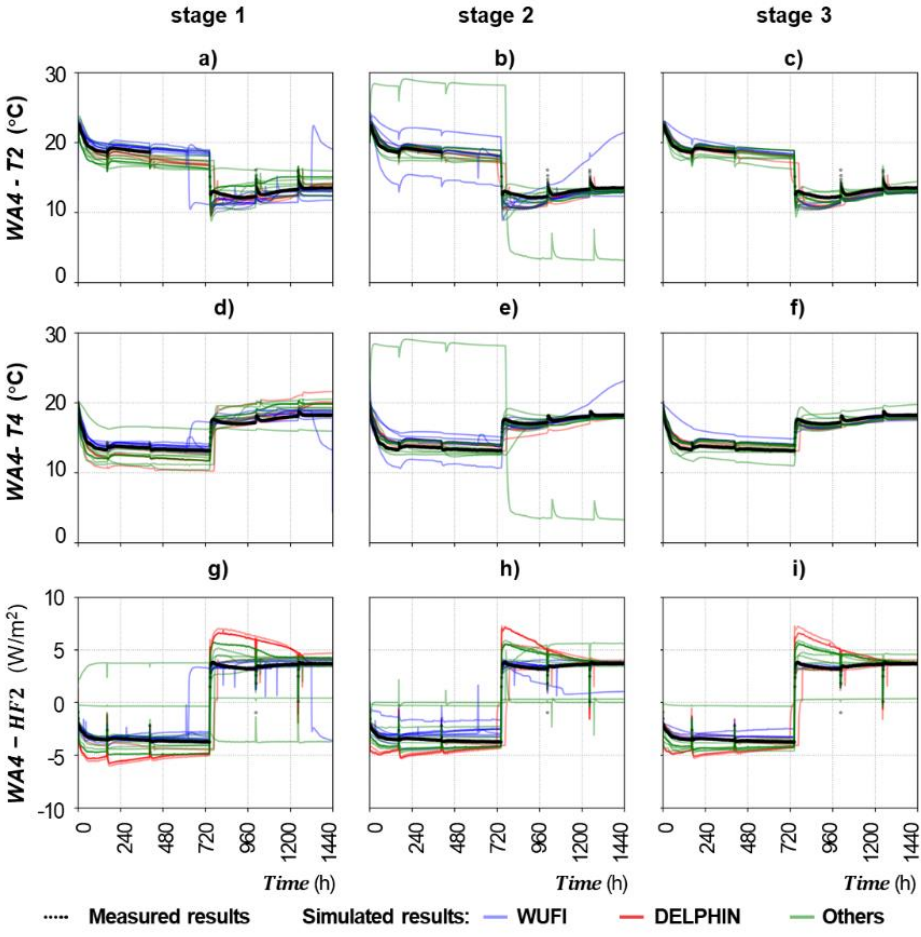


Fig. 6. 5 Simulated temperatures and heat fluxes of WA4: a) – c) T2, d) - f) T4 and g) - i) HF2.

It is obvious that the implemented material properties have a significant influence on the simulated moisture masses. Whether the materials are (1) selected from the databases of HAM models (stage 1) or (2) translated from the measured data (stage 2), there are always uncertainties. That of the former is mainly the mismatch between the hygrothermal properties of the actual materials and the material entries in the databases (assuming the developers' implementations are correct). That of the latter corresponds to the translation from the measured material properties (and some untested properties with reference values) to the respective formulations in the different models, during which specific assumptions, simplifications and approximations are made.

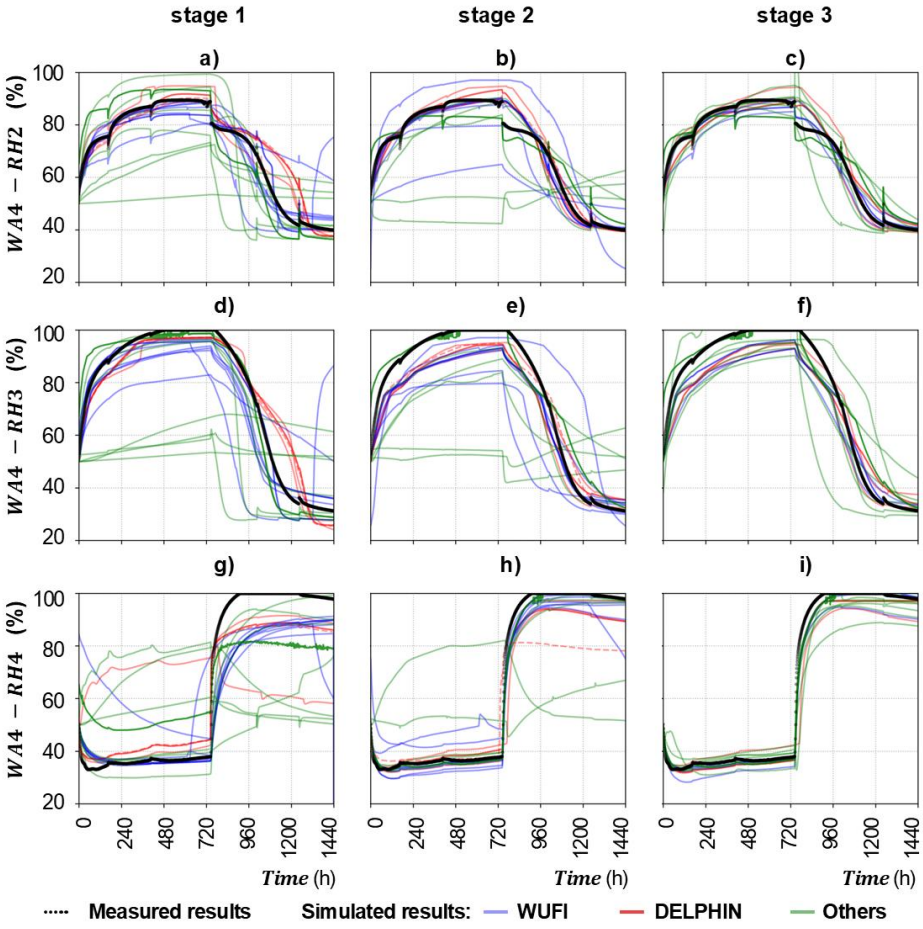


Fig. 6. 6 Simulated relative humidity of WA4: a) – c) RH2, d) – f) RH3 and g) – i) RH4.

In addition, user preferences, biases and errors also significantly contribute. For instance, some outputs likely include the data on wrong positions, for the opposite directions or wrong looping statements. In addition, more obvious errors occur, such as RH results between 0 and 1 (shown in dashed lines), instead of the required percentage and moisture contents in kg/m^3 instead of moisture masses in kg/m^2, judging from the trends and orders of magnitude. These kinds of deviations can be easily distinguished in this case but may be difficult to detect in more complicated scenarios and can lead to misinterpretation. Note that raw data are used for calculating NRMSE and *r*, so any errors are directly propagated into these metrics.

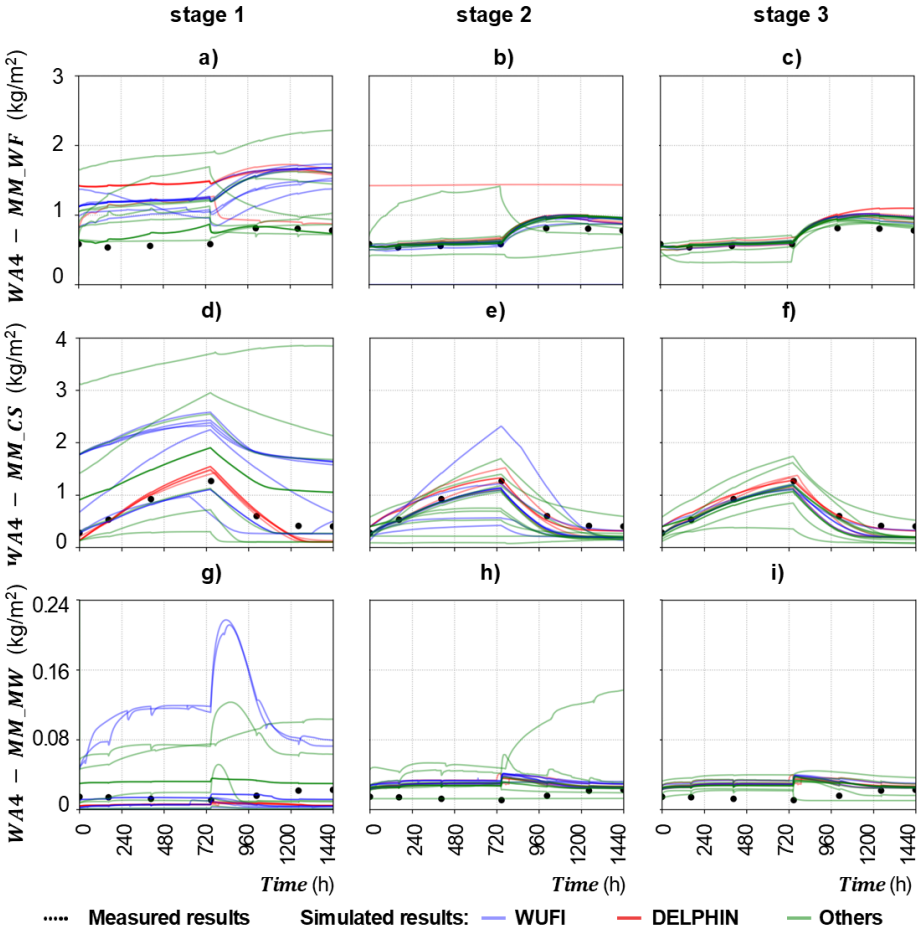


Fig. 6. 7 Simulated moisture masses in WA4: a) – c) of WF, d) – f) of CS, and g) – i) of MW.

While overall good agreement and a considerable improvement over stages are observed for temperature predictions, the heat fluxes obviously deviate from three model categories (Figs. 6.2g-i and 6.5g-i). Particularly around the 748th hour (when the boundary conditions are switched), some heat fluxes from DELPHIN (in red) experience a sharp increase before dropping, whereas most results from WUFI (in blue) remain closer to the measured results. Those from other models (in green) are mostly intermediate. To diagnose this disparity, Fig. 6.10 presents detailed outputs of the temperature profiles and heat fluxes in WA1, simulated by the author of this thesis using WUFI and DELPHIN. The temperature profiles are nearly identical (Fig. 6.10a), suggesting that the conduction heat flows in both models are comparable and not the source of the observed deviation.

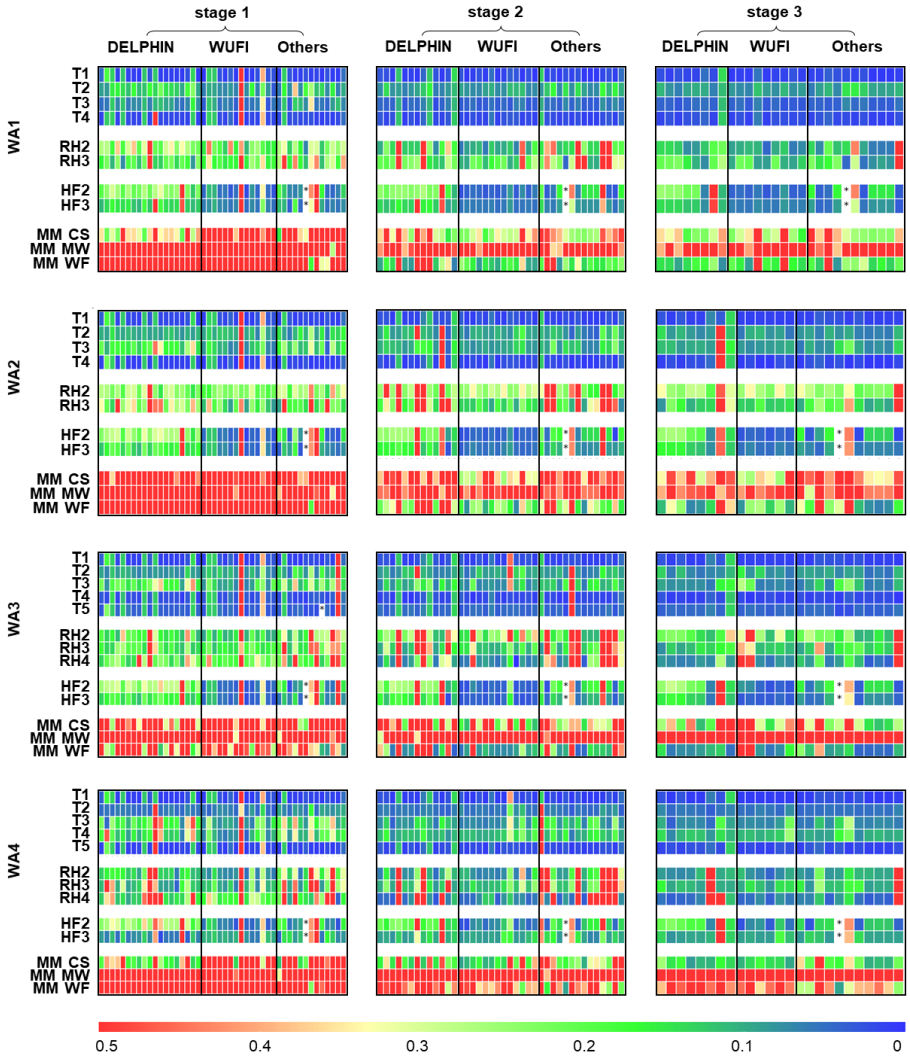


Fig. 6. 8 Normalized root-mean-square-error (NRMSE) between the simulated and measured hygrothermal responses ("the smaller, the better") (temperatures: T1 – T4, relative humidity: RH2 – RH4, heat fluxes: HF2 – HF3, and moisture masses: MM_CS, MM_MW and MM_WF).

A key distinction lies in how each model reports heat flux. DELPHIN allows users to output either the total heat flux or its individual components, including the conduction flux and the enthalpy fluxes associated with liquid convection, vapor diffusion and vapor convection (Outputs in DELPHIN 6.1). WUFI, by contrast, provides a single, unspecified "heat flux" output option, without clarifying whether enthalpy contributions are included.

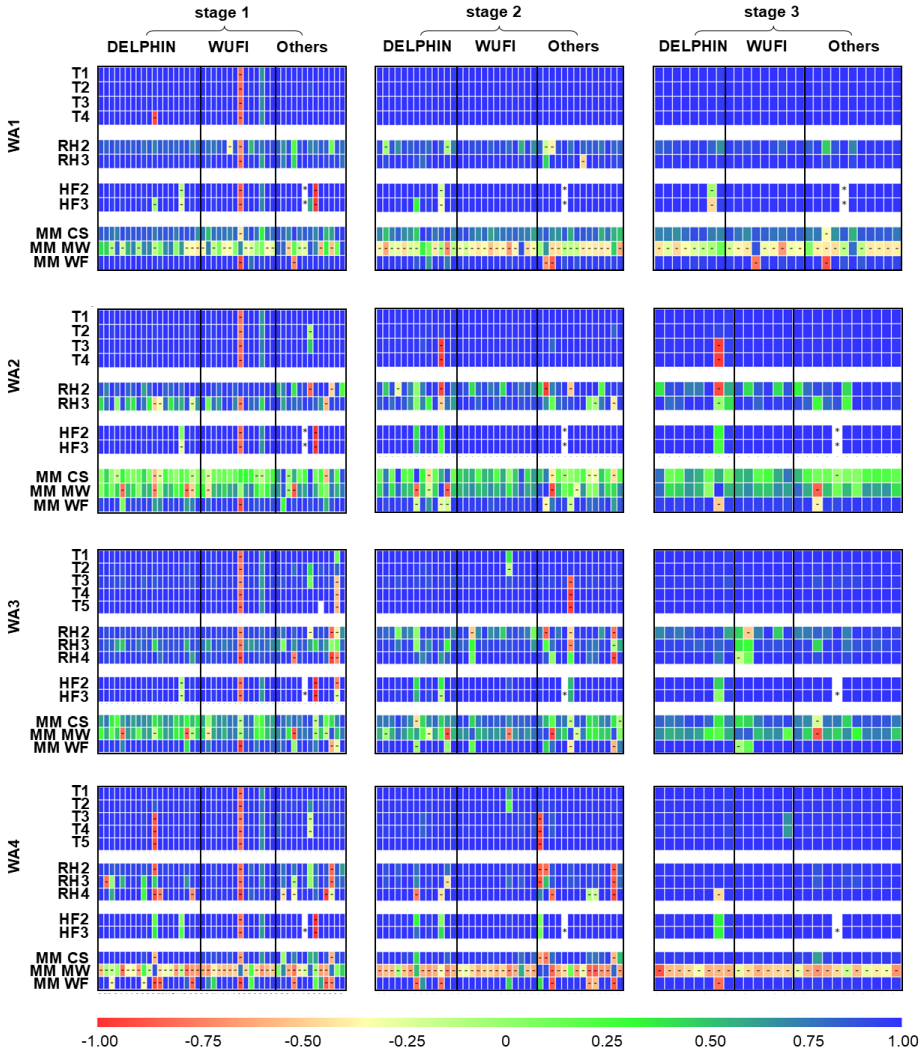


Fig. 6. 9 Pearson correlation coefficient (r) between the simulated and measured hygrothermal responses ("the closer to +1, the better") (temperatures: T1 – T4, relative humidity: RH2 – RH4, heat fluxes: HF2 – HF3, and moisture masses: MM_CS, MM_MW and MM_WF).

In the measurement, the heat flux sensors are configured to capture the conduction component only. However, many DELPHIN users select the output of "total heat flux" (including the author of this thesis in the initial simulation shown in Fig. 5.13), which includes the enthalpy contribution from moisture transport. This mismatch leads to noticeable deviations from the measured data, not due to computational errors, but to a misinterpretation of the measured quantity relative to the selected output. WUFI's default output, though vague, happens to align with the sensor's reading, resulting in better apparent

agreement (Fig. 6.10b). This underscores a critical point: users must clearly identify the physical quantity being measured and ensure that the model output corresponds to it. Misalignment between measured and simulated quantities can lead to misleading conclusion, even when simulations are technically correct. Model developers should provide transparent documentation and clearly define output variables to support accurate interpretation.

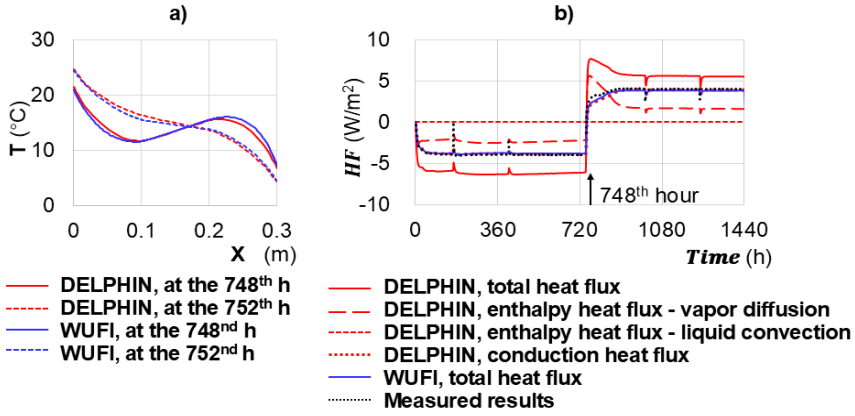


Fig. 6. 10 Detailed outputs of heat-related responses in WA1: a) temperature profiles at the 748th and 752nd hour, and b) heat flux components of HF2.

6.3 Impact of uncertainties in material properties on predicted hygrothermal responses

6.3.1 Implementation of material properties in stage 1

Obvious deviations in simulated hygrothermal responses are observed in stage 1, where participants rely on limited material data from technical sheets (see Table 6.2) as inputs. This restricted information, particularly the absence or partial availability of key hygrothermal properties such as moisture storage and transport function, constrains input accuracy and contributes to discrepancies in simulation outcomes. Participants have flexibility in defining their criteria for "similarity", either by matching one or more parameters (e.g., density ρ [kg/m^3], specific heat capacity, c [J/(kg·K)], thermal conductivity λ_{dry} [W/(m·K)], vapor resistance factor μ [-] and capillary absorption coefficient A_w [kg/(m^2·s$^{0.5}$)]), or selecting material entries from comparable manufacturers or production batches. However, similarity in one property may coexist with deviations in others (see Fig. 6.11) (Dang et al. 2025a). Additional uncertainty arises from discrepancies between the claimed values reported in

technical sheets and those determined through the material characterization tests (see Tables 5.2 and 6.2).

Table 6. 2 Claimed hygrothermal material properties in the technical sheets.

Material properties	CS	MW	WF	VB
ρ [kg/m³]	230-265	35	110	
c [J/(kg·K)]	1030		2100	
λ_{dry} [W/(m·K)]	0.067- 0.073	0.037	0.037	
μ [-]	2	1	3	> 5×10⁷
A_w [kg/(m²·s$^{0.5}$)]	0.85		≤ 1	

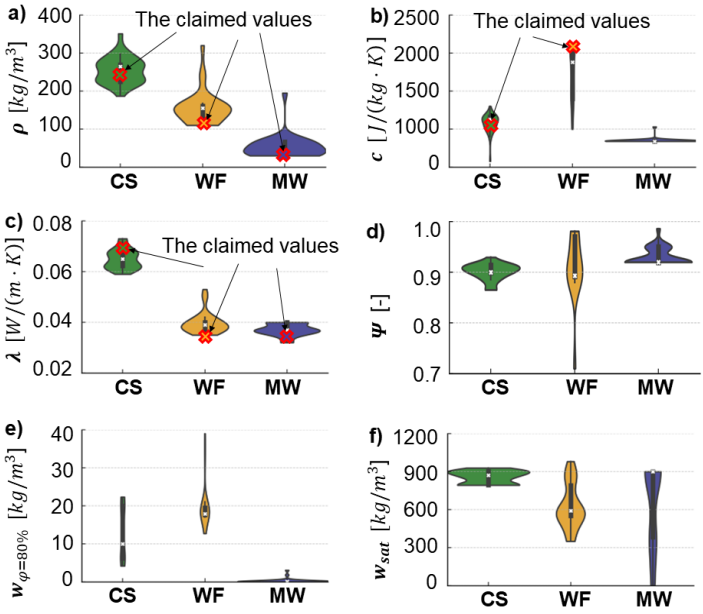


Fig. 6. 11 Implemented and claimed material properties: a) density ρ, b) specific heat capacity c, c) dry thermal conductivity λ_{dry}, d) porosity Ψ, e) moisture content at 80 % RH $w_{\varphi=80\,\%}$ and f) saturated moisture content w_{sat} in stage 1.

Figs. 6.12-6.13 illustrate the wide spectrum of the implemented moisture storage and transport properties applied in DELHIN and WUFI during stage 1, compared with the measured results. Data from other models are not shown due to translation complexity under different driving potentials. For CS,

differences in moisture storage capacity reach go up to 20 kg/m³ in the hygroscopic range (Figs. 6.12a&b) and 200 kg/m³ in the over-hygroscopic range (Figs. 6.12g&h), which may lead to significant deviations in RH evolution and moisture accumulation. Even larger differences are observed for MW, a non-hygroscopic material (Figs. 6.12c,d,i,j). Two main approaches are identified in the implementation of its moisture storage curve: most assume a purely non-hygroscopic behavior, applying linear interpolation in the over-hygroscopic range up to the saturation moisture content; others treat it as slightly hygroscopic, introducing gradual moisture uptake even in the hygroscopic range, possibly for numerical convenience. Neither approach fully captures the observed hygrothermal responses (Figs. 6.4d-f and 6.7g-i). Deviations are also evident in the implemented moisture transport properties, particularly for liquid transport: those of CS may differ by several orders of magnitude, while WF shows similarly large variations — some include liquid transport functions, others omit them entirely (Fig. 6.13).

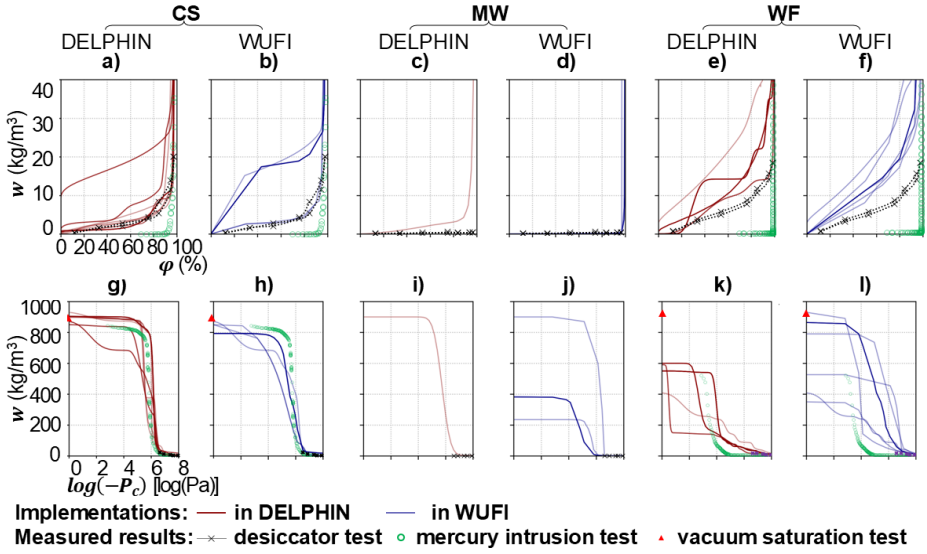


Fig. 6. 12 Implemented: a) – f) sorption isotherms $w(\varphi)$, and g) – l) moisture retention curves $w(P_c)$ in DELPHIN (in red) and WUFI (in blue) in stage 1.

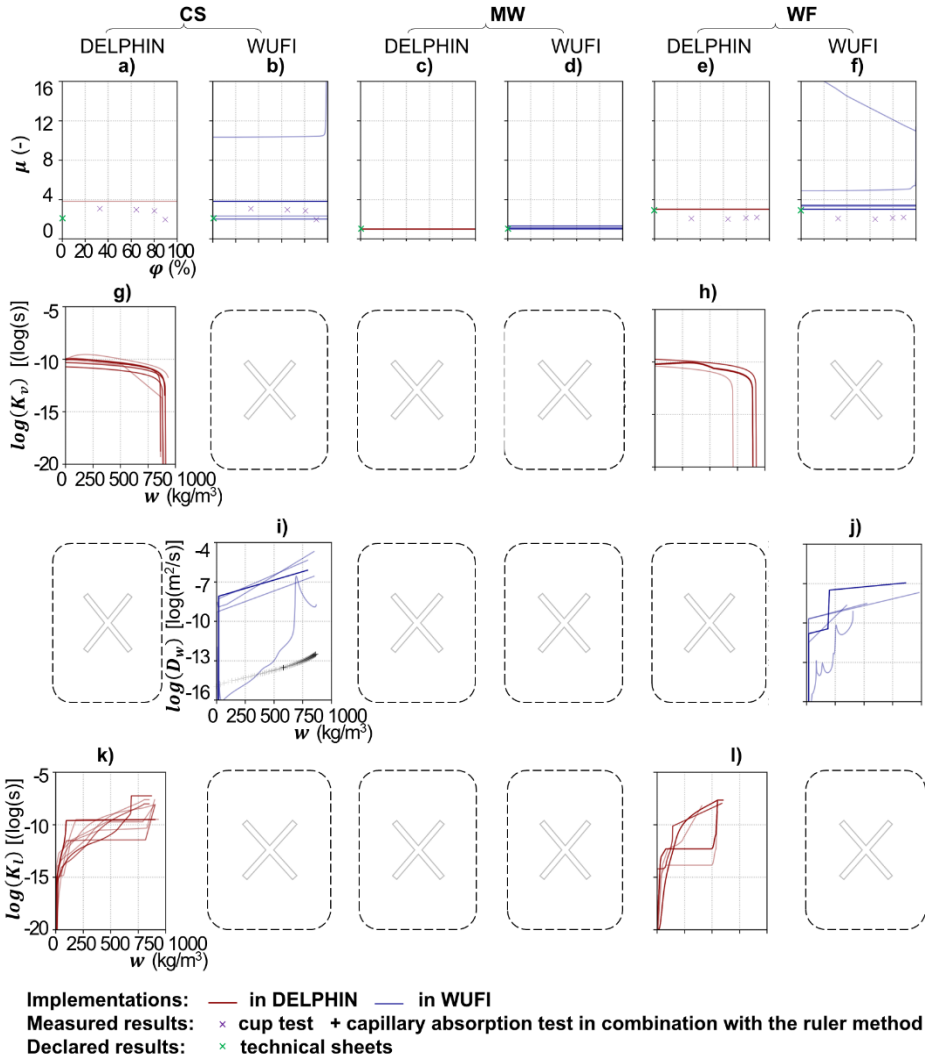


Fig. 6. 13 Implemented: a) – f) vapor resistance factor $\mu(\varphi)$, g) - h) vapor permeability $K_v(w)$, i) - j) liquid diffusivity $D_w(w)$, and k) - l) liquid permeability $K_l(w)$ in DELPHIN (in red) and WUFI (in blue) in stage 1.

6.3.2 Implementation of material properties in stage 2

In stage 2 most participants directly assign the measured values for simple single-valued parameters, although a few submissions contain errors (e.g., assigning data of material A to material B). For more complex parameters or functional inputs, such as moisture storage and transport properties, larger deviations are observed. These arise from different modeling assumptions,

simplifications, approximations as well as occasional human errors during the translation of measured data into model-specific formats. The implemented moisture storage and transport coefficients in DELHIN and WUFI in stage 2 are compared with the measured or claimed properties in Figs. 6.14 and 6.16.

Fig. 6.14 illustrates the implemented sorption isotherms $w(\varphi)$ and moisture retention curves $w(P_c)$ in WUFI and DELPHIN. The assignment for moisture storage function is compulsory for all materials including non-hygroscopic materials including MW. In DELPHIN, either function can be applied, while WUFI only supports sorption isotherms. The coordinator has converted these into moisture retention curves by applying Kelvin's law (Eq. 2.10) with additional interpolation to facilitate a comprehensive comparison. Due to the non-overlapping nature of the experimental results from the hygroscopic desiccator test and the mercury intrusion porosimetry (MIP) test (Feng and Janssen 2021), one needs to select among the provided results, for instance, by setting one dataset as the baseline (assumed to be the most accurate), while scaling or shifting partial data from other experiments (see Section 5.2).

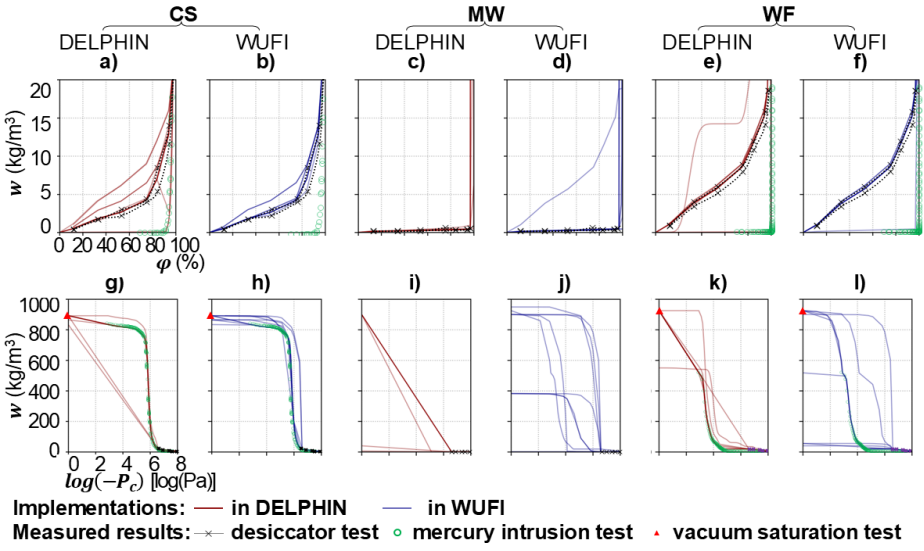


Fig. 6. 14 Implemented: a) – f) sorption isotherms $w(\varphi)$, and g) – l) moisture retention curves $w(P_c)$ in DELPHIN (in red) and WUFI (in blue) in stage 2.

Fig. 6.15 illustrates the simplification methods applied in implementing moisture storage properties in this case. Both WUFI and DELPHIN disregard the sorption hysteresis, requiring users to apply single (ab-/de-sorption or their average) curve (Figs. 6.15a&e). This simplification appears to have minimal impact given that the sorption hysteresis is negligible for the materials involved here. Desiccator test results are generally more straightforward and

considered more reliable in the hygroscopic range (Feng and Janssen 2021). Many participants implement sorption isotherms $w(\varphi)$ by linearly connecting the equilibrium moisture content at 97 % RH with the vacuum saturation moisture content (Fig. 6.15b). Unless expressed as a function of capillary pressure or other equivalent potentials (e.g., water chemical potential, Matsumoto 1978) that can enlarge the scope of X-axis, the deviations in over-hygroscopic range are unlikely to be diagnosed. A similar linear connection may also be applied when implementing moisture retention curves $w(P_c)$ (Figs. 6.14g,i,k and 6.15f). Despite limited reliability in the hygroscopic range and inherent experimental constraints (Diamond 2000), some participants still rely heavily on MIP results due to their completeness (Figs. 6.14a and 6.15c&g). Given the superior clarity and reliability of desiccator test result in the hygroscopic range compared to MIP data, the author processes the measured datasets as a piecewise function for $w(P_c)$: (1) applying desiccator test results in the hygroscopic range, (2) using adjusted MIP data in the over-hygroscopic range (Figs. 5.7a&b) to ensure smooth connections with (1) and (3) the measured saturation moisture content (Figs. 6.15d&h).

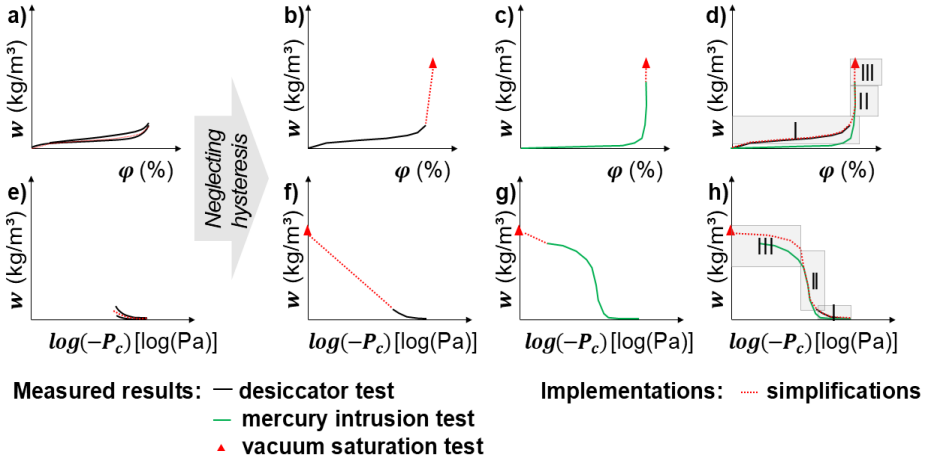


Fig. 6. 15 Simplifications in implementing moisture storage properties: a) – d) sorption isotherms $w(\varphi)$, and e) – h) moisture retention curves $w(P_c)$.

Water vapor transport properties can be written as vapor resistance factor $\mu(\varphi)$ or translated into vapor permeability $K_v(w)$, while liquid transport properties can be expressed as liquid diffusivity $D_w(w)$ or further converted into liquid permeability $K_l(w)$. All functions above are applicable in DELPHIN, while only vapor resistance factor $\mu(\varphi)$ and liquid diffusivity $D_w(w)$ are applicable in WUFI. Fig. 6.16 illustrates these implementations in DELPHIN and WUFI in stage 2. For vapor transport properties, most participants directly

adopt the measured results from the cup test, whereas others apply additional processing. A small number of DELPHIN users translate the measured vapor resistance factor at dry state μ_{dry} into $K_v(w)$ according to Eq. 2.20 (Hagentoft et al. 2004; Vogelsang et al. 2013) (see Fig. 6.16g).

For liquid transport properties, most participants rely on the data from the ruler method, while others turn to Künzel's formula (Eq. 2.14) to estimate the liquid diffusivity (see Figs. 6.16h&i). The corresponding liquid permeability K_l, calculated by multiplying liquid diffusivity with the slope of the moisture retention curve, can again lead to considerable deviations (Eq. 2.15, Fig. 2.2). Although MW is assumed to be non-capillary-active material, some participants still assign certain values to the liquid transport coefficients (Fig. 6.16j). For WF, only the capillary absorption coefficient (A_w = 0.02 kg/(m^2·s$^{0.5}$)) is measured and provided as the indicator for liquid transport, yielding different considerations: neglecting liquid transport properties or estimating a liquid diffusivity or a permeability function (Figs. 6.16k,l,n).

Another issue concerns the "double inclusion" of liquid transport: vapor transport dominates in the dry cup test, whereas the wet cup test also capture contributions from liquid water transport. To ensure consistency, the latter should either be separated into vapor and liquid components, preserving pure vapor transport values, or merged into a total moisture transport coefficient. As suggested by the WUFI developers, the implementation should be either based on a constant μ value (from the dry cup test) together with liquid transport properties, or alternatively it should use $\mu(\varphi)$ function without implementing additional liquid transport properties (WUFI forum1). However, a considerable proportion of the participants apply both $\mu(\varphi)$ function and liquid diffusivity. A similar concept should be complied within DELPHIN: the vapor permeability K_v (translated from dry cup test, considering pure vapor transport) should be accompanied with liquid permeability K_l. This "double inclusion" exists in 20 CS property files and 11 WF property files, out of the 26 WUFI/DELPHIN submissions in stage 2. While the contribution of liquid transport under low-humidity conditions may be limited, its potential impact warrants further investigation and will be examined in detail in Section 7.3.

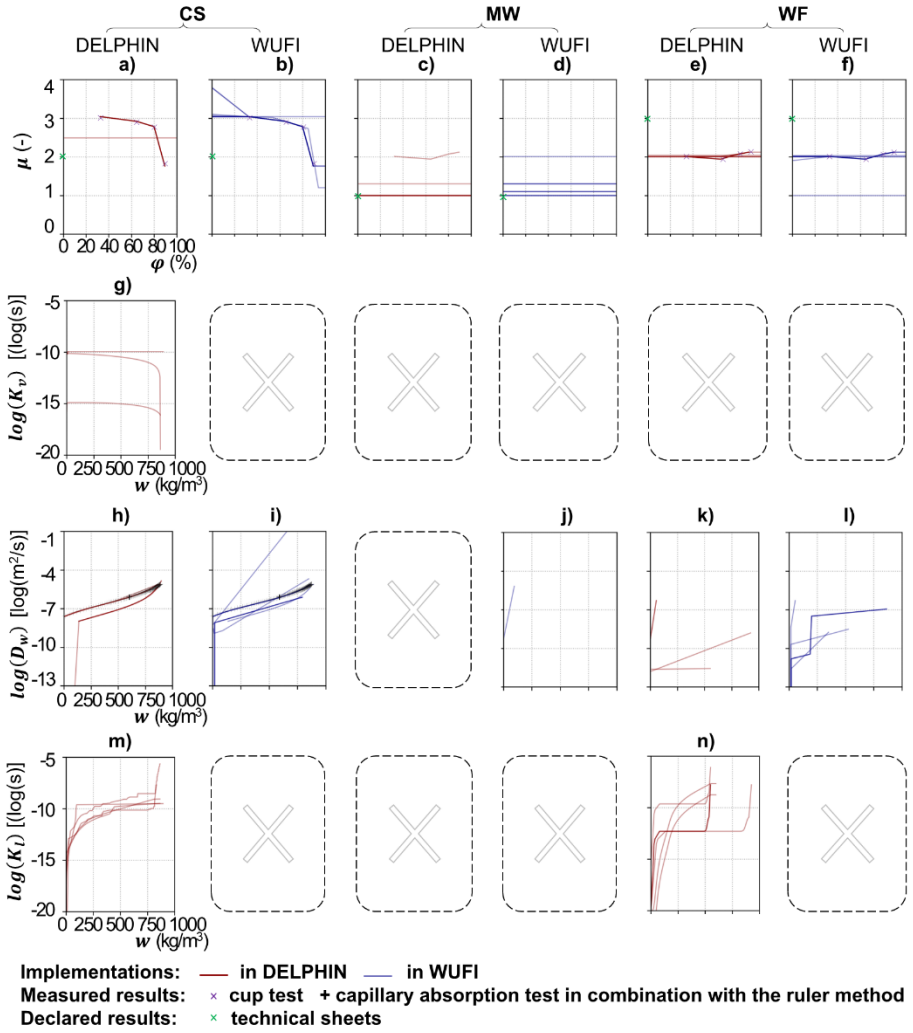


Fig. 6. 16 Implemented: a) – f) vapor resistance factor $\mu(\varphi)$, g) vapor permeability $K_v(w)$, h) – l) liquid diffusivity $D_w(w)$, and m) - n) liquid permeability $K_l(w)$ in DELPHIN (in red) and WUFI (in blue) in stage 2.

6.3.3 Impact of input uncertainties on output accuracies in stages 1 and 2

To examine how deviations in implemented material properties affect the accuracy of simulated hygrothermal responses, two series of NRMSE results for WA1 and WA4 from stages 1 and 2 are analyzed. The comparison isolates the role of material properties, as other inputs are uniformly defined and relatively simple. The analysis focuses on moisture-related responses, given that heat-related outputs are generally well captured. Specifically, the NRMSE is calculated for (1) the deviations between the measured and implemented

moisture storage properties (specifically, $w(\varphi)|_{\varphi<97\%}$, since most materials act mainly in the hygroscopic range) or moisture transport properties (specifically, a newly introduced parameter, "equivalent moisture permeability" $K_{v+l}|_{\varphi<97\%}$, under the gradient of vapor pressure), and (2) the deviations between measured and calculated moisture-related responses. The Pearson correlation (r) between the two NRMSE series indicates which inputs have crucial impacts on which outputs, and how influential the impacts are. The outliers are excluded according to the 1.5-IQR rule. To harmonize the properties expressed in different forms and/or under different gradients, the equivalent permeability K_{v+l} is applied (Eq. 6.3). Four representative sets of material parameters implemented in WUFI and DELPHIN are translated using Eqs. 6.4-6.7, assuming a stagnant air permeability of δ_a = 1.9×10^{-10} kg/(m·s·Pa) and a saturation vapor pressure $P_{v,sat}$ = 2338 Pa at 20 °C. Fig. 6.17 compares the resulting values with the baseline results from the cup test.

$$g_{v+l} = -\left(K_v + K_l \cdot \left(\frac{\partial P_c}{\partial P_v}\right)\right)\nabla P_v = -K_{v+l}\nabla P_v \tag{6.3}$$

$$K_{v+l} = \frac{\delta_a}{\mu} \text{ [when } \mu \text{ is used as the parameter]} \tag{6.4}$$

$$\begin{aligned} K_{v+l} &= \frac{\delta_a}{\mu} + D_w \cdot \left(\frac{\partial w}{\partial P_v}\right) = \frac{\delta_a}{\mu} + D_w \cdot \left(\frac{\partial w}{\partial \varphi}\right) \cdot \left(\frac{\partial \varphi}{\partial P_v}\right) \\ &= \frac{\delta_a}{\mu} + D_w \cdot \left(\frac{\partial w}{\partial \varphi}\right) \cdot \frac{1}{P_{v,sat}} \text{ [when } \mu \text{ \& } D_w \text{ are used as the parameters]} \end{aligned} \tag{6.5}$$

$$K_{v+l} = \frac{\delta_a}{\mu} + K_l \cdot \left(\frac{\partial P_c}{\partial P_v}\right) \text{ [when } \mu \text{ \& } K_l \text{ are used as the parameters]} \tag{6.6}$$

$$K_{v+l} = K_v + K_l \cdot \left(\frac{\partial P_c}{\partial P_v}\right) \text{ [when } K_v \text{ \& } K_l \text{ are used as the parameters]} \tag{6.7}$$

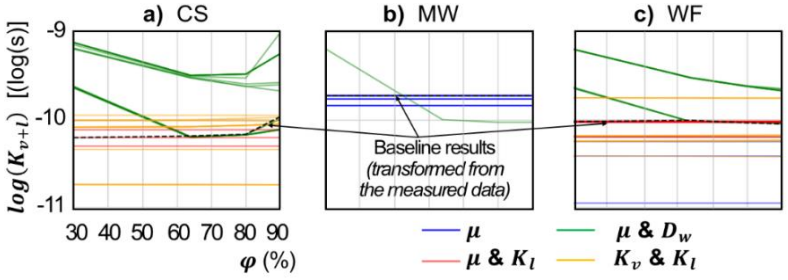


Fig. 6. 17 The equivalent moisture permeability K_{v+l} translated from the implemented moisture transport properties by participants using WUFI and DELPHIN in stages 1 and 2.

Fig. 6.18 illustrates the correlations between (1) the NRMSE between measured and implemented moisture storage properties (Fig. 6.18a) or moisture transport properties (Fig. 6.18b) and (2) the NRMSE between measured and simulated moisture-related responses: a higher r value indicates a larger

impact of the implemented hygric material properties on the corresponding simulated moisture-related responses.

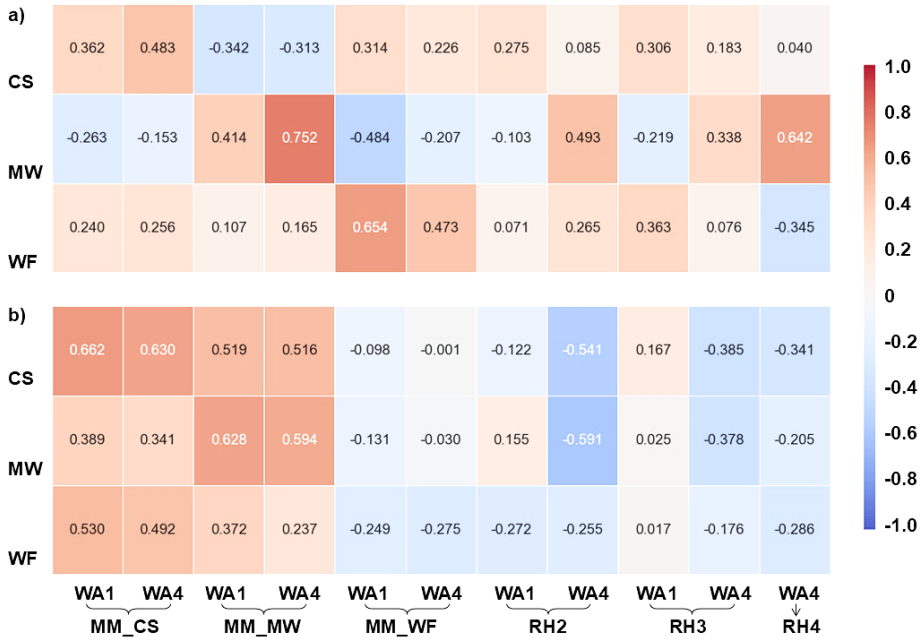


Fig. 6. 18 Pearson correlations between inputs and outputs in stages 1 and 2: a) r between (1) NRMSE between measured and implemented $w(\varphi)$ and (2) NRMSE between measured and calculated outputs, and b) r between (1) NRMSE between measured and implemented $K_{v+l}(\varphi)$ and (2) NRMSE between measured and calculated outputs.

A first strong expression is that both moisture storage and transport properties have a significant impact on the moisture mass and RH of primarily the material itself and sometimes of the neighboring materials. Specifically, implemented moisture storage properties influence the amount of moisture flows between materials and thereto RH at the interfaces, while the moisture transport properties influence the speed of moisture flows. An exception is observed in the impact of WF's moisture transport property on its moisture mass. A possible explanation is that moisture transport in WF also occurs beyond the hygroscopic range, which is excluded from the correlation analysis. Moreover, due to experimental limitations in characterizing liquid transport in WF, only vapor-phase properties are measured and provided, requiring independent estimation of liquid-phase behavior and introducing additional uncertainty. Beyond these material-specific issues, inherent model differences and user-induced impact cannot be excluded. These factors may also contribute to the observed deviations, which helps explain why the resulting correlations are not strictly aligned.

The moisture-related predictions are highly sensitive to the implementation of hygric material properties. Building on this correlation-based attribution analysis, future research may incorporate targeted sensitivity analyses to deepen understanding of these dependencies. Moreover, integrating measured moisture mass into model validation is essential for revealing how input hygric properties influence hygrothermal predictions, beyond conventional reliance on temperature and relative humidity.

6.3.4 Insights from model fine-tuning in stage 3

The provided measured hygrothermal responses in stage 3 allow investigating whether simulation outcomes are close to experimental observations. While there are also uncertainties in the measurement (e.g., logger errors, inherent limitations in experiment protocols, etc.), the measured hygrothermal responses can be used as a reference to modify the implementations for a "more satisfied" result. Since multi-factors are involved in most submissions, it is difficult to evaluate the impact on each specific adjustment with other variables controlled, but these adjustments with positive effects reported by the participants are summarized below. Out of the 28 submissions, five remained unchanged as in stage 2. These contributors were satisfied with the agreement between simulation results and the measured datasets or avoided further adjustment to prevent artificial fitting without physical accuracy. Among the rest 23 complete submissions, a range of strategies are implemented to refine the simulation models. Most adjustments are made in refining moisture storage functions (10, the number of submissions, same below), liquid transport functions (10), surface transport coefficients (9), and thermal conductivities (5). The frequency order of the adjusted materials is CS (16), MW (10), WF (7) and VB (1). Some participants mentioned that an improved accuracy is observed after refining the grid discretization (6) and correcting sensor positions (2) to better capture the physical setup. Some participants took the chance to correct errors (5) in implementing surface transport coefficients, initial conditions, and boundary conditions as well as output positions or units.

Chapter 7 Assessing the implementation of material properties in WUFI and DELPHIN

Building on insights from the round robin validation, this chapter systematically investigates the strategies and uncertainties in the implementation of material properties in representative heat, air and moisture (HAM) models, particularly in WUFI and DELPHIN (Dang et al. 2025c, 2025d, 2026). To address three key modeling challenges — (1) implementation of liquid transport properties, (2) integral or separate formulations for vapor and liquid transport properties and (3) implementation of moisture storage properties, comparative simulations are conducted in different representative scenarios.

7.1 Problem statement and research scheme

HAM models have diverged in selecting driving potentials and describing material properties to resolve the discontinuity of moisture content potential at the materials' interface (Straube and Burnett 2001; Hens 2007; Janssen et al. 2007; Funk et al. 2008; Janssen 2011). Among the most widely used HAM models are WUFI and DELPHIN. While their underlying algorithms are largely mathematically and physically equivalent (see Eqs. 2.1-2.5), simulation outcomes may still vary significantly. The round robin test revealed that, despite using identical experimental datasets (Dang et al. 2024b, 2024c), moisture-related predictions varied notably across models and users — highlighting the impact of different assumptions, simplifications and approximations in implementing hygric material properties (Dang et al. 2025b). However, user-induced variability in other assignments across submissions introduces additional uncertainties, complicating sensitivity analyses (Dang et al. 2025a). In a follow-up study (Dang et al. 2025c), comparative simulations of the same experimental setup were conducted using the same HAM model (DELPHIN) by the same person (the author of this thesis) to isolate the effects of implementation strategies for material properties. Moisture transport properties were implemented via different approaches, and their impact on hygrothermal response predictions were compared. Interestingly, no significant deviations in

hygrothermal predictions were observed across these approaches. This outcome is attributed to the fact that the HB–CB test scenarios primarily fall within the hygroscopic range, where liquid water transport — typically more sensitive to implementation differences — is not dominant. Nevertheless, further investigation is warranted to assess how different strategies for implementing material properties may influence simulation results, particularly under conditions where capillary transport plays a more significant role.

To support a meaningful extension of simulation regimes beyond those employed in the round robin test, it is first necessary to identify and understand the uncertainties in characterizing and transforming material properties. These uncertainties generally arise from three main sources: (1) intra-operator repeatability (on same samples performed by the same individual using the same equipment in the same lab) (ISO 5725-1), (2) inter-operator reproducibility (on same samples performed by different individuals using different equipment or following different measurement protocols in different labs) (Roels et. al. 2004; López et. al. 2017; Feng et al. 2020) and (3) material heterogeneity (including production-related inconsistencies, e.g., between manufacturers or between batches from the same manufacturer, in engineered materials and intrinsic variability particularly in natural materials) (Aït Oumeziane et. al. 2021; Xu et. al. 2023; Hofheinz et. al. 2025). Whereas the impact of repeatability is relatively restricted, material heterogeneity and inter-operator reproducibility are known to be significant (Feng et al. 2015). These uncertainties are particularly pronounced for properties that cannot be directly measured and must be inferred through physical or mathematical transformation (Roels et al. 2004). For instance, liquid diffusivity can be determined from moisture content profiles measured via e.g., X-ray or nuclear magnetic resonance (NMR), with the Boltzmann transformation (Roels et al. 2003) or through simplified alternatives (Ren et al. 2019). Translating such data into liquid permeability or other equivalent parameters introduces further complexities, as outcomes are influenced by other factors like the slope of the moisture retention curve (see Figs. 2.1 and 2.2). Even for more accessible properties like the moisture retention curve, covering the full saturation range often requires combining results from multiple characterization tests. Discrepancies frequently arise — for instance, moisture retention curves derived from mercury intrusion porosimetry (MIP) test often conflict with those translated from the gravimetric desiccator test in the hygroscopic range (Feng and Janssen 2021; Dang et al. 2024b). Sorption hysteresis can also lead to deviating adsorption and desorption curves (see Figs. 6.15a&e) (Zhu et. al. 2025). In practice, many users rely on existing databases (Kumaran 1996; ASHRAE 2013; Materialdatensammlung für die energetische Altbausanierung), particularly

those embedded in commercial models such as WUFI and DELHIN. However, due to material heterogeneity and inconsistent data processing practices, entries for seemingly "identical" materials often vary significantly in their hygric properties (Yamamoto and Takada 2022). The flexibility afforded to users in selecting and assigning the properties further amplifies discrepancies in simulation outcomes (Dang et al. 2025a). While sensitivity analyses have indeed highlighted the significance of such disparities (Panico et al. 2023; Janssens et al. 2024; Vandemeulebroucke et al. 2023, 2024; Gan et al. 2025), there remains a need for more targeted strategies to improve the implementation.

This chapter examines these differences across four simulation stages.

Stage 1 (see Section 7.2) employs HAMSTAD Benchmark 4 (Hagentoft et al. 2004) to compare approaches for implementing liquid transport properties. The wall configuration, comprising an external load-bearing layer and an internal finishing layer, is subjected to "extreme" moisture exposures featured by wind-driven rain (WDR). An additional evaluation is conducted under measured real-world climate conditions using the same setup. This stage evaluates deviations in simulation outcomes resulting from liquid diffusivity $D_w(w)$ estimated using Künzel's formula (Eq. 2.14), as recommended by WUFI, compared to experimentally derived data and their corresponding liquid permeabilities $K_l(w)$. All relevant property formats are implemented in both WUFI and DELPHIN if possible. The comparisons highlight not only impact of implementation strategies but also reveal the intrinsic model differences.

Stage 2 (see Section 7.3) introduces two virtual configurations: a concrete wall internally insulated with either autoclaved aerated concrete (AAC) or calcium silicate (CS). Each setup is subjected to either a wetting–drying cycle or continuous wetting as typical "service" conditions, where vapor and liquid transport mechanisms are both active. This stage examines how different strategies for combining or separating vapor and liquid transport properties influence hygrothermal predictions. All simulations are performed in DELPHIN due to its broader support for property formats, including all possible implementation approaches compatible with WUFI.

Stages 3 and 4 (see Section 7.4) evaluate moisture storage properties under the same "extreme" and "service" scenarios used in stages 1 and 2. While the moisture retention curve provides a relatively robust method for defining storage behavior in the over-hygroscopic range, these stages focus on uncertainties associated with the sorption isotherm $w(\varphi)$, particularly the accuracy of two fitting formulas for the sorption isotherm curve, recommended or embedded in WUFI. All simulations are performed in WUFI.

Table 7.1 summarizes the simulation scenarios and analytical objectives across the four stages. This structured analysis compares how different implementations of hygric properties influence simulation outcomes across "extreme", "real climate" and "service" moisture exposure regimes, revealing modeling uncertainties in WUFI and DELPHIN and informing strategies to improve prediction reliability.

Table 7. 1 Overview of simulation scenarios and analytical objectives.

Details / Stages	Configurations and boundary conditions	Simulation models	Key questions addressed
Stage 1	HAMSTAD Benchmark 4, under "extreme" or "real climate" conditions	WUFI and DELPHIN	Reliability of Künzel's formula (Eq. 2.14) for $D_w(w)$ estimation, and equivalence between $D_w(w)$ and $K_l(w)$ derived via different methods/models
Stage 2	Concrete-AAC or -CS, under "service" conditions	DELPHIN	Equivalence between integral and separate implementation of vapor and liquid transport properties
Stage 3	HAMSTAD Benchmark 4, under "extreme" conditions	WUFI	Reliability of two fitting formulas for $w(\varphi)$ in WUFI
Stage 4	Concrete-AAC or -CS, under "service" conditions	WUFI	

7.2 Implementation approaches for liquid transport properties

Stage 1 uses the HAMSTAD Benchmark 4 as a controlled setting. As shown in Fig. 7.1, the airtight wall consists of a 0.1 m thick external load-bearing material and a 0.02 m thick internal finishing layer, both exposed to heat and moisture loads. All required simulation input data (including material properties, boundary conditions and initial conditions) are explicitly provided in the instruction document (Hagentoft et al. 2004).

This scenario addresses the representation of liquid transport properties in regimes characterized by capillary flow. DELPHIN couples vapor diffusion and capillary transport using simultaneous vapor pressure and capillary pressure as driving potentials in its default formulation. WUFI, in contrast, uses relative humidity (RH) as the driving potential for both vapor and liquid transport, and follows a segmented implementation: vapor diffusion is continuous across the entire RH range, while liquid transport represented by a moisture-dependent diffusivity becomes active only above 80 % RH. The

comparative analysis in this stage explores how these fundamentally different formulations influence simulation outcomes in conditions where liquid transport plays a dominant role. In accordance with the validation publication provided by DELPHIN's developers (Sontag et al. 2013), this study adheres to their parameter assignments. Although WUFI lacks a dedicated validation document, the simulations adhere to HAMSTAD input requirements. Grid discretization is further refined to minimize numerical artifacts.

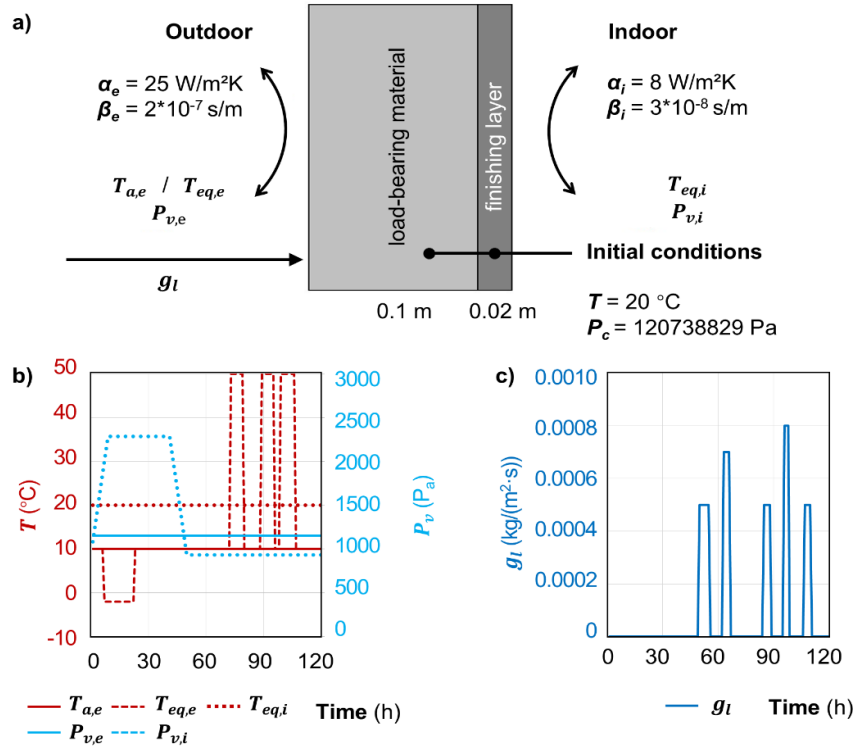


Fig. 7. 1 HAMSTAD Benchmark 4: a) geometry, surface transport coefficients and initial conditions, and b) & c) boundary conditions.

Table 7.2 and Fig. 7.2 present the implementation approaches and the resulting liquid transport properties in the comparative cases. The only modification adopted here pertains to the implementation approaches for the liquid transport properties of the load-bearing material. On the one hand, the default approach, referred to as approach K1.0, is precisely represented by the provided data series of the $K_l(P_c)$ function. By linking this with the slope of the moisture retention curve (see Eq. 2.15), a theoretically equivalent $D_w(w)$ function can be derived, leading to the approach D1.0. The approaches K1.0 and D1.0 are simulated in DELPHIN and WUFI respectively. Note that DELPHIN

only supports strictly monotonic material property functions. Therefore, the original D1.0 curve, whose liquid diffusivity exhibits a peak in low moisture content range, must be modified by excluding certain data points to meet this criterion and yield a modified approach, D1.1. Approach D1.1 is applied in both WUFI and DELPHIN to enable inter-model comparison. On the other hand, liquid diffusivity can be estimated using Künzel's formula (Eq. 2.14), and WUFI can generate the curve via logarithmic interpolation between the calculated values at 80 % and 100 % RH. This method forms the basis of approach D2.0. The required capillary absorption coefficient A_w [kg/(m·s$^{0.5}$)] and capillary moisture content w_{cap} [kg/m^3] are obtained by a preceding capillary absorption simulation, in which the original $K_l(P_c)$ function is implemented. Since the D2.0 approach is compatible with both WUFI and DELPHIN, it is also selected for inter-model comparison to assess differences. Expanding on this, another approach D2.1 involving the two liquid diffusivities, $D_{ws}(w)$ and $D_{ww}(w)$, is simulated in WUFI. Since DELPHIN only supports single moisture diffusivity function, the result of $D_{ws}(w)$ is implemented in approach D2.0, while the translated $K_l(P_c)$ function leads to a separate approach, K2.0. This configuration generates four cases in DELPHIN (K1.0, K2.0, D1.1 and D2.0) and four cases in WUFI (D1.0, D1.1, D2.0 and D2.1).

Table 7. 2 Implementation approaches for liquid transport properties.

Implementation approaches and models	Data resources and processing methods
K1.0 (DELPHIN)	Provided in the HAMSTAD instruction document (Hagentoft et al. 2004)
D1.0 (WUFI)	Theoretically equivalent to and translated from K1.0 (DELPHIN) via Eq. 2.15, subject to inter-model differences
D1.1 (DELPHIN)	Adapted from D1.0 (WUFI) by excluding certain data in low moisture content range to ensure monotonicity
D1.1 (WUFI)	Theoretically equivalent to D1.1 (DELPHIN), subject to inter-model differences
D2.0 (WUFI)	Estimated using Künzel's formula (Eq. 2.14)
K2.0 (DELPHIN)	Theoretically equivalent to D2.0 (WUFI), subject to inter-model differences
D2.0 (DELPHIN)	Theoretically equivalent to D2.0 (WUFI), subject to inter-model differences
D2.1 (WUFI)	Adapted from D2.0 (WUFI) by distinguishing $D_{ww}(w)$ from $D_{ws}(w)$ with the default reduction

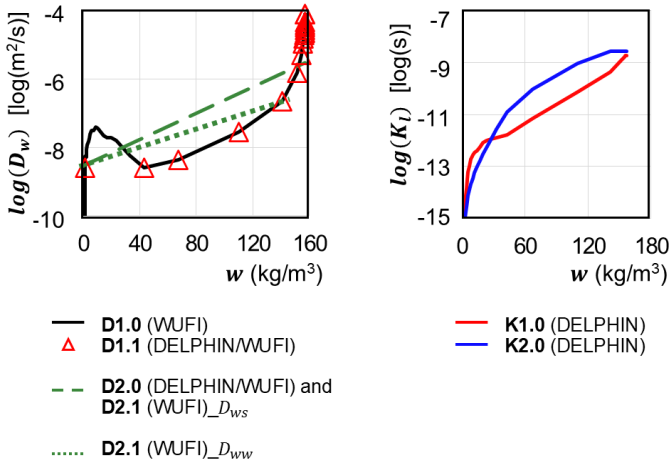


Fig. 7. 2 Implementation approaches for liquid transport properties of stage 1.

An additional remark concerns the implementation of moisture storage properties in WUFI, though it is not the focus of this section. The data series of $w(P_c)$ function is provided in the HAMSTAD instruction document. Since WUFI only supports $w(\varphi)$ function, a conversion via Kelvin's law (Eq. 2.10) is applied. Simulations start with manually input moisture contents at default RH values, progressing in increments of 10 % from 0 % to 50 %, 5 % from 50 % to 90 %, and 1 % from 90 % to 99 %, with additional points at 99.5 % and 100 %. However, abrupt boundary condition transitions, particularly rain events accompanied with low temperatures, make moisture storage highly sensitive to the $w(\varphi)$ function in the over-hygroscopic range, causing sudden saturation jumps on the exterior surface. To smooth the curve, additional input data points, converted from $w(P_c)$ function via Kelvin's law, are inserted between 99.5 % and 100 % RH. Results indicate that the more interpolation points are provided for the $w(\varphi)$ function, the more accurate WUFI's predictions become. In contrast, DELPHIN appears more robust: even with sparse input data that would lead to inaccuracies in WUFI, it still yields results consistent with those derived from the $w(P_c)$ function. This suggests that DELPHIN may perform more refined internal interpolation automatically, whereas WUFI's accuracy remains highly dependent on the input resolution.

The comparative simulations are conducted in two steps. In the first step, different implementation approaches are applied to the liquid transport properties of the load-bearing material while all other inputs remain consistent with those specified in the instruction (Hagentoft et al. 2004). The simulated hygrothermal responses are then compared against predictions from the HAMSTAD project participants. Although experimental evidence is unavailable, inter-model comparison provides a reference. In the second step, the

boundary conditions are changed into a full-year in-situ experimental dataset of the VLIET building (Leuven, Belgium; "VL") (Fig. 7.3) (Dang et al. 2024a, 2025e), which includes wind-driven rain (WDR) imposed to the wall, thereby making the differences more pronounced under real-life weather conditions. All other inputs remain the same as in the first step.

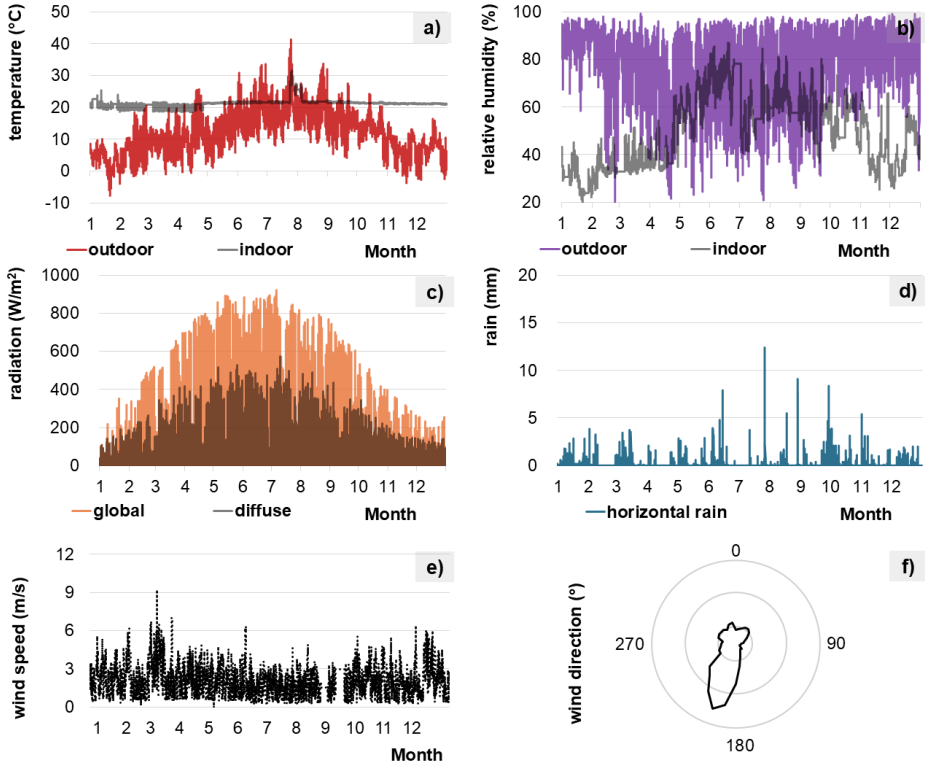


Fig. 7. 3 Weather conditions at VL: a) temperature, b) relative humidity, c) solar radiation, d) horizontal rain, e) wind speed, and f) wind direction.

Fig. 7.4 illustrates the simulated moisture contents at both surfaces and moisture content profiles in the first step of stage 1, compared against the predictions from the HAMSTAD participants (indicated by the gray band). Overall, the outcomes from various scenarios exhibit a consistent trend with the reference, although differences exist in the fluctuation amplitudes and the variation rates due to the different implementation strategies for the liquid transport properties of the load-bearing material.

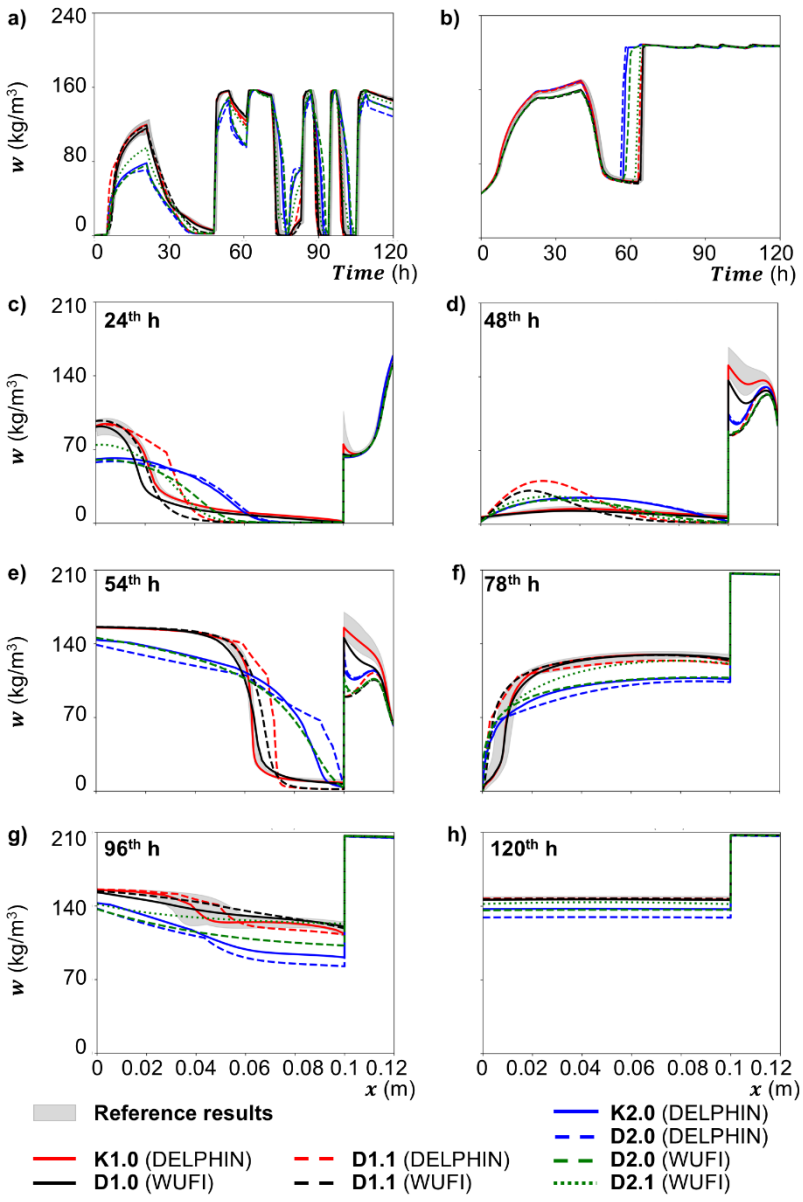


Fig. 7. 4 Simulated moisture contents on a) exterior surface and b) interior surface, and c) – h) moisture content profiles at the 24th, 48th, 54th, 78th, 96th and 120th hours in the step 1 of stage 1.

As its outer boundary is sensitive to rain exposures, certain discrepancies are observed in the moisture content fluctuations, as illustrated in Fig. 7.4a. In general, the approaches K1.0 and D1.0, which either fully implement or completely transform the material properties as instructed, produce outcomes

that align most closely with the reference results. Although D1.1 incorporates simplifications in the low-humidity range to comply with the monotonicity requirement, it still maintains good consistency. Conversely, K2.0 and D2.0, based on the liquid diffusivity curve derived from the simplified formula (Eq. 2.14), exhibit significant deviations from the given curve in the high-humidity range. These discrepancies result in distinct variations in peak moisture levels and waveform shifts during extreme transitions between dry and wet conditions. The D2.1 approach, which applies dual moisture diffusivities depending on rainy or non-rainy conditions, yields predictions that generally fall between the 1.0-series and 2.0-series. Despite the consistent implementation of material properties of the internal finishing layer across scenarios, its moisture content remains influenced by the variations in the moisture dynamics of the load-bearing material (Fig. 7.4b). The distinction between 1.0-series versus 2.0-series curves appears to exert a slightly greater impact than the inherent differences between models. This is largely attributed to the overall higher liquid permeability and diffusivity in the capillary range associated with the 2.0-series, resulting from the use of Künzel's formula (Eq. 2.14). The moisture content profiles (Figs. 7.4c-h) further highlight the influence of various strategies for modeling liquid transfer properties. For the load-bearing material, the 1.0-series and 2.0-series scenarios form distinct groups, with the former aligning more closely with the reference results. Model-related differences are also evident: approach D1.1 produces divergent results in the two models; the discrepancy between D2.0 (DELPHIN) and D2.0 (WUFI) almost exceeds that between D2.0 (DELPHIN) and K2.0 (DELPHIN), despite their theoretical equivalence. This may stem from inter-model differences, although precise attribution is challenging due to the non-disclosure of both software codes.

Fig. 7.5 illustrates the simulated moisture mass (MM) of the load-bearing material in the second step of stage 1. Although displayed in logarithmic scale, the differences among various scenarios are not readily distinguishable. To enhance interpretability, the main plot overlays the overall range (the light blue area) with the mean curve (the bright blue line), while the red shading indicates the standard deviation across scenarios. Periods of heightened material moisture contents and larger standard deviations, specifically the 10-day spans in February, March and October, underscore the potentially greater influence of different implementation approaches, as clearly illustrated by the magnified intervals in the upper subplots.

Overall, the discrepancies between models may exceed those introduced by parameter conversion. For example, D2.0 (DELPHIN) almost entirely overlaps K2.0 (DELPHIN) but exhibits some deviation from D2.0 (WUFI). In

contrast, K1.0 (DELPHIN) and D1.0 (WUFI) demonstrate better agreement, generally predicting lower moisture contents than D1.1 (DELPHIN & WUFI), which underestimates moisture transport in low-humidity regions due to monotonicity constraints, potentially leading to slower evaporation predictions. Furthermore, since D2.0 (WUFI) and D2.1 (WUFI) employ identical implementations for moisture transport properties during rain events, their localized magnifications appear nearly identical.

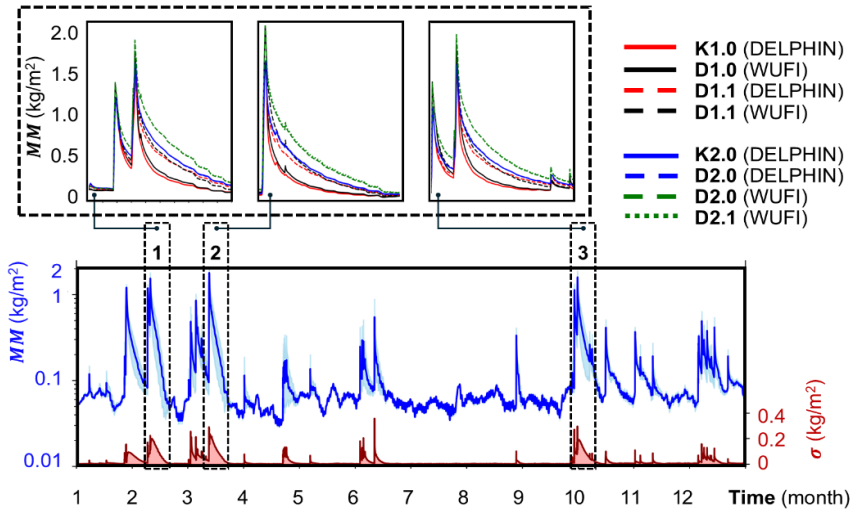


Fig. 7. 5 Simulated moisture masses of the loading-bearing material in the step 2 of stage 1.

However, when examining annually cumulative outcomes in Table 7.3, D2.1 (WUFI) produces overall the highest moisture contents, likely due to its suction characteristics being identical to D2.0 (WUFI) but exhibiting slower redistribution. The liquid diffusivity applied for redistribution is intended to represent reduced moisture transfer; however, the assignment criteria for both types of liquid diffusivities in WUFI depend solely on rainfall occurrence. This simplified approach fails to account for spatial variations in moisture transfer rates within the structure, leading to significant overestimations or, in some cases, potential underestimations. Given the inherent difficulty of direct measurements, it remains challenging to determine which model is closer to the reality. Nevertheless, the rationale behind distinguishing the two methods solely based on the presence or absence of rainfall warrants further scrutiny — particularly considering that, in high-humidity conditions, the numerical discrepancy between the two methods can differ by an order of magnitude.

Table 7. 3 Data characteristics of simulation moisture contents of the loading-bearing material in the step 2 of stage 1.

Metrics / Scenarios	Min.	P25	Median	P75	Max.	Avg.
K1.0 (DELHIN)	0.0300	0.0537	0.0653	0.0861	1.6068	0.0902
D1.0 (WUFI)	0.0284	0.0533	0.0660	0.0961	2.0331	0.1032
D1.1 (DELPHIN)	0.0300	0.0543	0.0654	0.0835	1.5996	0.0976
D1.1 (WUFI)	0.0284	0.0537	0.0653	0.0908	2.0211	0.1075
K2.0 (DELPHIN)	0.0300	0.0537	0.0649	0.0907	1.6169	0.1045
D2.0 (DELPHIN)	0.0300	0.0539	0.0651	0.0897	1.6143	0.1043
D2.0 (WUFI)	0.0284	0.0542	0.0657	0.1072	2.0605	0.1267
D2.1 (WUFI)	0.0284	0.0543	0.0657	0.1081	2.0606	0.1274

7.3 Integral versus separate implementation approaches for vapor and liquid transport properties

Stage 2 primarily investigates different formulations of vapor and liquid transport properties, evaluating their influence on predicted hygrothermal responses, particularly under boundary conditions that may partially drive materials into the over-hygroscopic regime. While the integral and separate implementations of vapor and liquid transport terms are often equivalent, notable questions remain. A key concern is whether supplementary data for liquid transport properties, derived via the Boltzmann transformation (Roels et al. 2003) or Künzel's formula (Eq. 2.14), should complement the cup test results. As preliminarily discussed in Dang et al. 2025c, such supplementation becomes particularly significant in the over-hygroscopic range. However, for low-moisture-content (hygroscopic) range, it may lack accuracy and even lead to risks of overestimation (Carmeliet et al. 2004). Furthermore, whether vapor and liquid transport properties are implemented integrally or separately can influence hygrothermal predictions in a case-dependent manner. To investigate this, virtual scenarios are introduced in this section, featuring a 300 mm concrete wall internally insulated with 100 mm of either AAC or CS. The two

configurations differ in sorption behavior, representing wetting-drying (WD) and pure wetting (WW) conditions (Fig. 7.6).

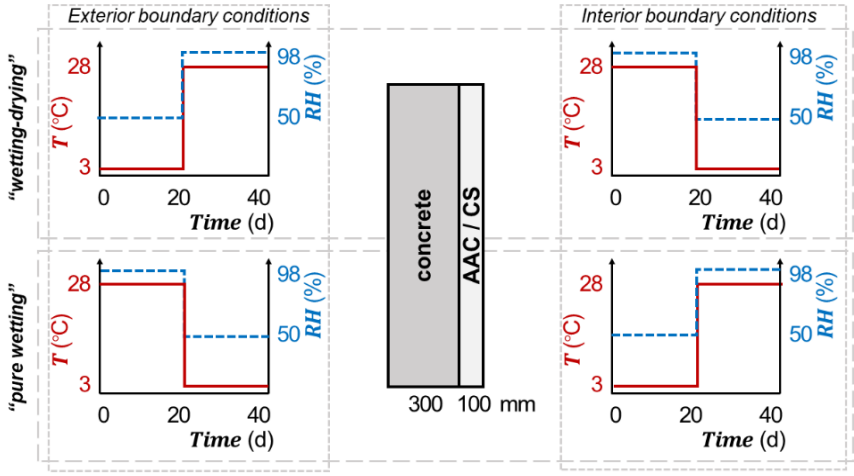


Fig. 7. 6 Wall configurations and boundary condition schemes of the "wetting-drying" and "pure wetting" scenarios in stage 2.

In both configurations, the concrete layer acts as vapor-tight, effectively blocking vapor diffusion through its thickness, whereas the CS and AAC layers are highly capillary-active, enabling significant liquid water transport. Under the imposed boundary conditions representing either pure wetting or combined wetting and drying, the system exhibits both vapor and liquid water transport. This also creates distinct combinations of moisture transfer mechanisms in each scenario, allowing the influence of vapor-liquid transport interactions to be examined under contrasting sorption regimes. In the WD scenario, the boundary conditions are set to 3 °C and 50 % RH on the left ("outdoor") and 28 °C and 98 % RH on the right ("indoor") for the first 20 days, enabling wetting of the AAC or CS layer. For the subsequent 20 days, the conditions are reversed to induce a drying process. In contrast, the WW scenario applies boundary conditions that are opposite to those in the WD scenario for both phases. During the first 20 days, the left side is set to 28 °C and 98 % RH, and the right side to 3 °C and 50 % RH. In the subsequent 20 days, the conditions are reversed. In all scenarios, initial conditions are set to 15 °C and 75 % RH. The surface transport coefficients follow the HAMSTAD instruction document: α_e = 25 W/m^{2}K and β_e = 2*10^{-7} s/m for the "outdoor" side, while α_i = 8 W/m^{2}K and β_i = 3*10^{-8} s/m for the "indoor" side (Hagentoft et al. 2004). These scenarios represent conditions in which both vapor and liquid transport mechanisms are active, allowing an assessment of how integrated versus separated modeling approaches influence hygrothermal predictions. To eliminate

model-specific discrepancies, all simulations are performed in DELPHIN, which supports multiple formats of material properties.

The properties of material "ConcreteB25_411" in DELPHIN's database are assigned to concrete. For AAC and CS, the hygric properties are derived from Feng and Janssen (2021), whereas their thermal properties are assigned based on comparable entries in DELPHIN's material database. Table 7.4 provides an overview of the single-valued properties (density ρ [kg/m^3], porosity Ψ [m^3/m^3], specific heat capacity c [J/(kg·K)], thermal conductivity λ [W/(m·K)], vapor resistance factor at dry state μ_{dry} [-], capillary saturation moisture content w_{cap} [kg/m^3], vacuum saturation moisture content w_{sat} [kg/m^3] and capillary absorption coefficient A_w [kg/(m·s$^{0.5}$)]). The moisture storage properties are implemented using a piecewise function (Dang et al. 2025b): only the portion of the sorption isotherm below 97.4 % RH and the portion of the moisture retention curve above 97.4 % RH are used.

Table 7. 4 Single-valued hygrothermal material properties implemented in stage 2.

Material properties	Concrete	AAC	CS
ρ [kg/m^3]	2320.2	461.2	271.0
Ψ [m^3/m^3]	0.143	0.814	0.891
c [J/(kg·K)]	850	1081	1160
λ [W/(m·K)]	2.100	0.095	0.065
μ_{dry} [-]	110.00	7.35	1.97
w_{cap} [kg/m^3]	136.0	313.4	755.8
w_{sat} [kg/m^3]	143.0	812.6	888.8
A_w [kg/(m·s$^{0.5}$)]	0.008	0.046	1.010

The only variable relates to the moisture transport properties of CS and AAC. Feng and Janssen (2021) reported the measured $\mu(\varphi)$ function from the cup test, along with necessary data to derive the $D_w(w)$ and $K_l(w)$ functions — either via the Boltzmann-transformed X-ray attenuation test or through Künzel's formula (Eq. 2.14). The integral approach V0L0 is derived entirely from the $\mu(\varphi)$ function from the cup test. Its separate version V1L1, incorporating a constant vapor transport term and a liquid transport term as outlined

in Eq. 2.17, is included to evaluate equivalence. Other scenarios integrate additional data for liquid transport properties derived from measurement or simplified approaches. Specifically, two implementation approaches for vapor transport properties are explored: a reduction as described in Eq. 2.16 (sub-approach V2) and a linear reduction (sub-approach V3). For liquid transport properties, two implementation approaches are considered: either based on X-ray attenuation test (sub-approach L2) or Künzel's formula (sub-approach L3). Their combinations lead to four paired scenarios: V2L2, V2L3, V3L2 and V3L3, complementary to V0L0 and V1L1. All six scenarios are simulated in DELPHIN due to its compatibility with all property formats. Note that except for V0L0 that implements the measured $\mu(\varphi)$ function, the others represent vapor and liquid transport properties using the K_v and K_l functions. An overview of these implementation approaches is provided in Table 7.5.

Table 7. 5 Implementation approaches for moisture transport properties.

Approaches	Descriptions
V0L0	The $\mu(\varphi)$ function as directly obtained from the cup test is implemented.
V1L1	Vapor and liquid transport terms are separated from the cup test results (Eq. 2.17). The constant value, μ_{dry}, is assigned to the $\mu(\varphi)$ function or converted to the $K_v(w)$ function, assuming vapor transport is constant without reduction. The $K_l(w)$ function subtracting the vapor contribution from the total is implemented.
V2L2	The non-linear reduction (Eq. 2.16) is applied for the $K_v(w)$ function separated from the cup test results. The measured $D_w(w)$ or translated $K_l(w)$ functions derived from X-ray attenuation test is implemented.
V2L3	The non-linear reduction (Eq. 2.16) is applied for the $K_v(w)$ function separated from the cup test results. The estimated $D_w(w)$ or translated $K_l(w)$ functions using Künzel's formula (Eq. 2.14) is implemented.
V3L3	The linear reduction is applied for the $K_v(w)$ function separated from the cup test results. The measured $D_w(w)$ or translated $K_l(w)$ functions derived from X-ray attenuation test is implemented.
V3L3	The linear reduction is applied for the $K_v(w)$ function separated from the cup test results. The estimated $D_w(w)$ or translated $K_l(w)$ functions using Künzel's formula (Eq. 2.14) is implemented.

Fig. 7.7 illustrates the resulting vapor and liquid transport properties corresponding to these approaches. Generally, the V3 curves exhibit significant underestimation in the low moisture content range, whereas V2 shows only slight deviation from V1. While the discrepancies between L2 and L3 typically remain within one order of magnitude, L1 appears to significantly underestimate liquid transport behavior in the high moisture content range relative to

both approaches. The differences in the scale of X-axis between pure vapor and liquid transport properties reflect a modeling assumption in DELPHIN: vapor transport is assumed to extend up to vacuum saturation, whereas liquid transport is limited by capillary saturation.

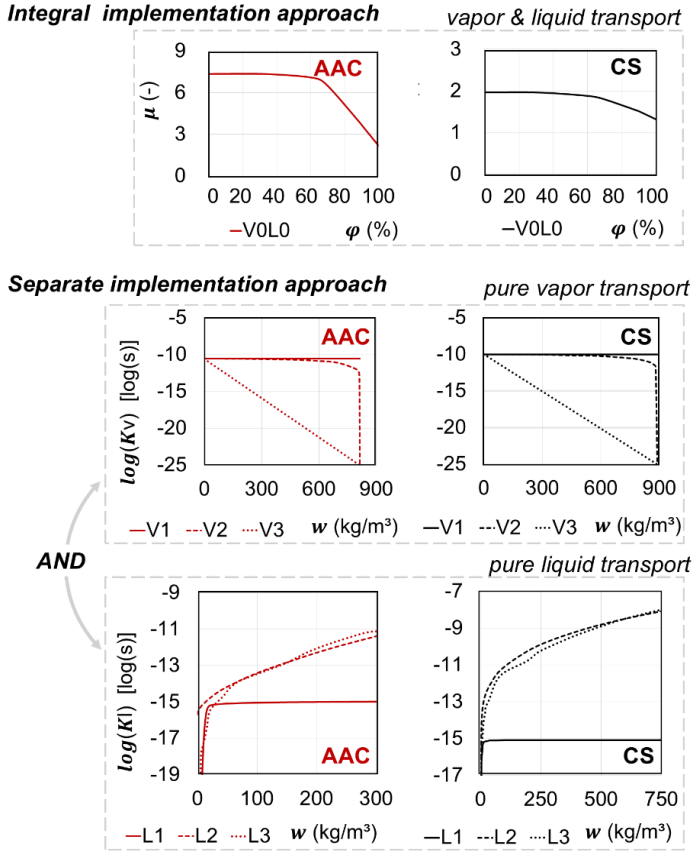


Fig. 7. 7 Implemented vapor and liquid transport properties in stage 2.

The "equivalent permeability" K_{v+l} [s] (Dang et al. 2025b) is employed to harmonize the properties in different gradients in Fig. 7.8. Overall, in the hygroscopic range, the equivalent permeabilities derived from the L2-related approaches for both materials are significantly higher, whereas L3 — estimated using the simplified formula — aligns with the results from V0L0 and V1L1 better, which are purely based on cup test results. Since vapor transport is the prevailing mechanism in the hygroscopic range (Roels et al. 2003), the Boltzmann-transformed X-ray attenuation test results likely overestimate moisture behavior in this range. The vapor transport terms contribute to the differences but to a limited extent. In the over-hygroscopic range, the permeabilities associated with L2 and L3, which include an independent moisture

transport component, show a noticeable increase. The results for AAC converge across different methods, while for CS, L2 consistently exceeds L3.

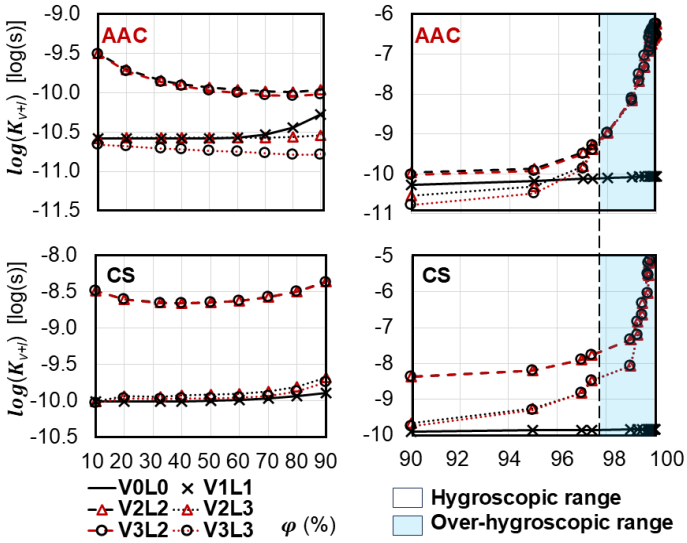


Fig. 7. 8 Equivalent vapor and liquid permeabilities implemented in stage 2.

Figs. 7.9 and 7.10 present the simulated RH profiles and moisture masses (MM) time series for stage 2. The 480th and 960th hours are visualized as they mark the transition in boundary conditions and the termination of the numerical simulation. From the RH perspective, the simulated results for concrete remain nearly identical across all scenarios, whereas the CS or AAC layer enters the over-hygroscopic range to different extents. When the CS or AAC layer primarily remains within the hygroscopic range (Figs. 7.9b,d,e,g), the variations are largely influenced by the specific sub-approach for implementing liquid transport properties. Regarding the MM time series for the two sorption processes across the two wall configurations, no clear pattern emerges. The differences between V0L0 and V1L1 are pronounced, even surpassing those observed in scenarios where additional liquid transport terms are incorporated (Fig. 7.10). In the concrete-AAC wall, similar trends appear among materials assigned to the same implementation approaches for liquid transport properties; conversely, the impact of vapor transport property on the concrete-CS wall seems non-negligible (Figs. 7.10b,d,f,h).

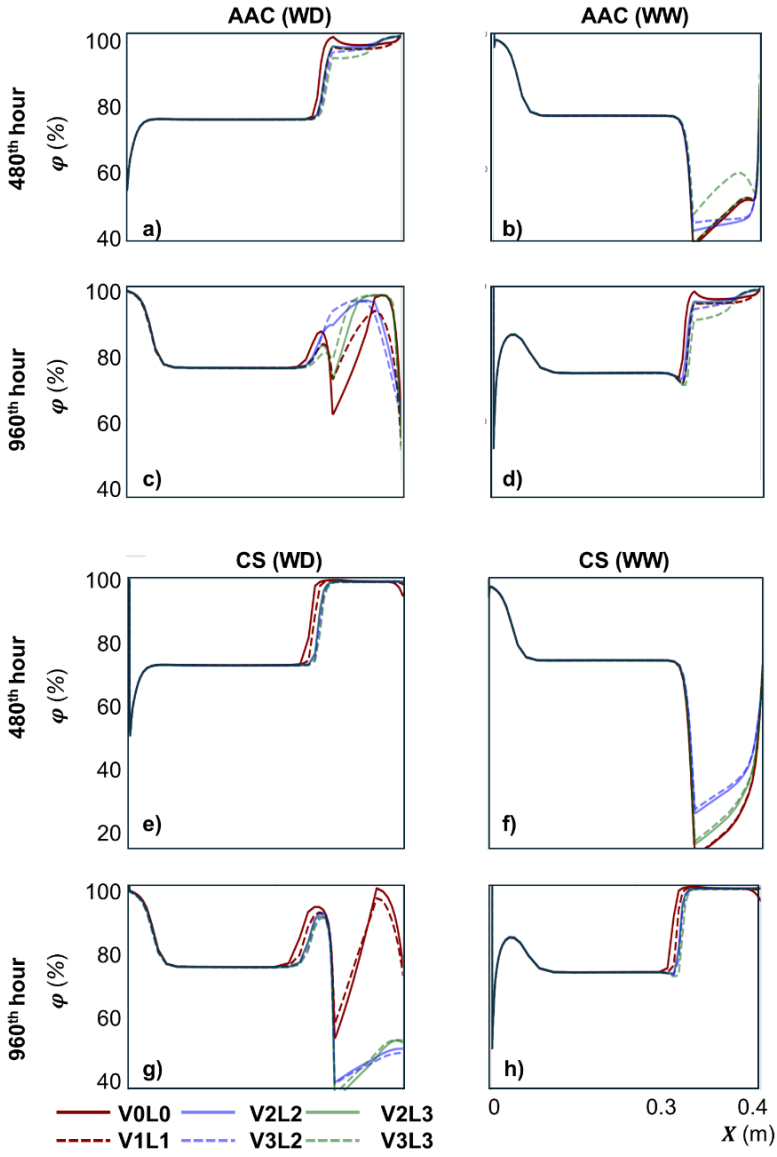


Fig. 7. 9 Simulated relative humidity profiles at the 480th and 960th hours in stage 2.

While incorporating or omitting additional liquid transport terms has an impact, the more noteworthy discrepancies occur between scenarios V0L0 and V1L1, where moisture transport properties derived from the cup test are implemented either integrally or separately yet remain theoretically equivalent. However, these differences suggest underlying implementation nuances.

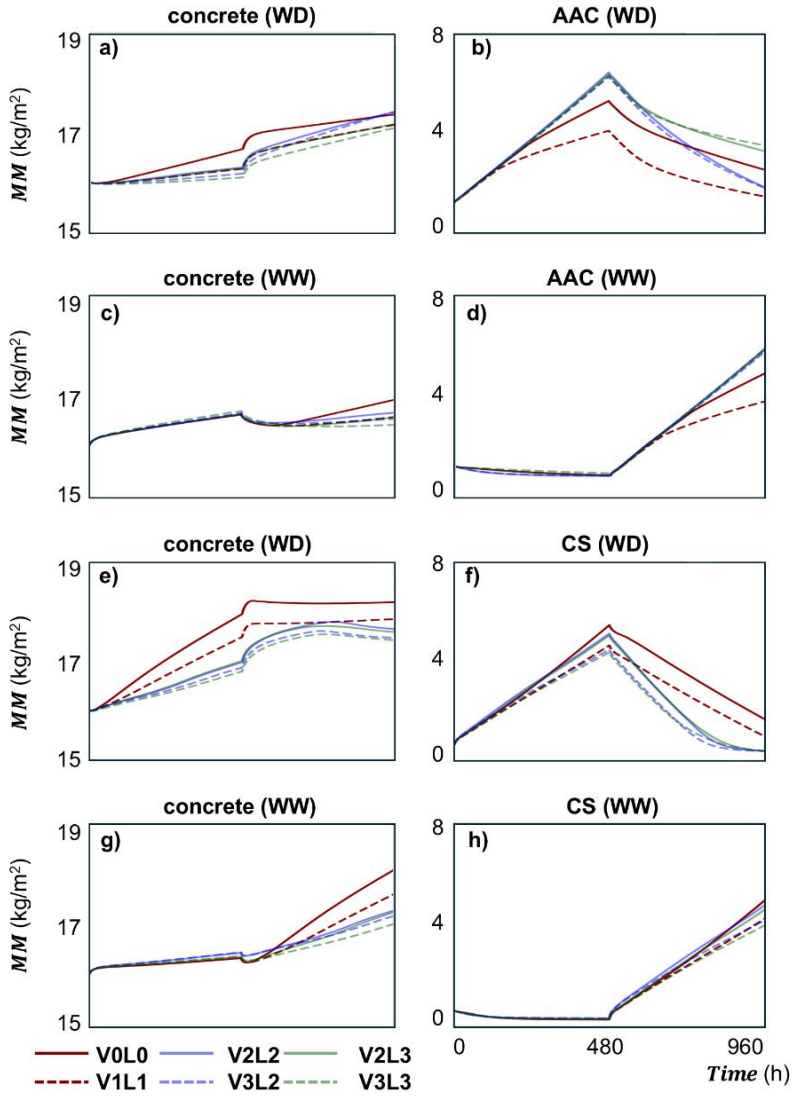


Fig. 7. 10 Simulated moisture masses of concrete, CS and AAC layers in stage 2.

In fact, the default reduction applied to the $\mu(\varphi)$ function in DELPHIN (as described in Eq. 7.1) is only identified after unexpected deviations are observed in the simulation results and subsequently clarified through direct communication with the model developers — information not disclosed in the user manual or published literature. This reduction, however, does not apply if users pre-convert the data to the default $K_v(w)$ function, thereby avoiding the internal adjustment. To assess whether this internal reduction accounts for the discrepancies, an additional simulation is conducted using an adjusted $\mu(\varphi)$ function divided by the reduction factor, aiming to restore the original

cup test results as expected to be implemented in the integral implementation approach shown in Fig. 7.7. Interestingly, this adjusted V0L0 scenario does not yield significant differences compared to the previously reduced V0L0 version. Nevertheless, this observation does not preclude the possibility that such reductions may lead to substantial in other case. Therefore, it is recommended to convert parameters into DELPHIN's default formats prior to simulation, to avoid uncertainties from undocumented internal reductions.

$$\mu(\varphi)_{reduction} = \mu(\varphi)_{user-input} \cdot \left(1 - \frac{w}{w_{sat}}\right) \tag{7.1}$$

Despite these efforts, the discrepancies between V0L0 and V1L1 remain unresolved. Another explanation is that the two implementation approaches treat moisture fluxes differently, which may affect the advection of sensible and latent heat within the heat balance equation (Eq. 2.3), thereby influencing the moisture transport. Specifically, V1L1 considers a portion of moisture flow as liquid flow for the calculation of sensible heat advection, while V0L0 treats the entire moisture flux as vapor flow, thereby accounting for the full latent heat transport associated with L_v in Eq. 2.3. As latent heat transport plays a far more significant role than sensible heat transport, this difference likely contributes more substantially to the observed discrepancies. To validate this hypothesis, two additional approaches are introduced: (1) V0L0_Kv, where the $\mu(\varphi)$ function is converted into the $K_v(w)$ function via Eq. 7.2 (similar to Eq. 2.16 but without reduction and utilizing varied μ values) to verify the equivalence with V0L0 and (2) V0L0_Kl, where the $\mu(\varphi)$ function is fully transformed into the $K_l(w)$ function, as described in Eq. 7.3 (following the derivation in Eq. 2.2). These approaches are compared with the existing approaches V0L0 and V1L1. In sum, V0L0 and V0L0_Kv rely solely on vapor transport, whereas V0L0_Kl uses only liquid transport. In contrast, V1L1 incorporates both vapor and liquid mechanisms. The WD scenario of the concrete-CS wall is used for these supplementary comparisons on the four approaches.

$$K_v(P_c) = \frac{D_{va}}{\mu(\varphi) \cdot R_v T} \cdot \frac{\nabla P_c}{\nabla P_v} \tag{7.2}$$

$$K_l(P_c) = \delta_v \cdot \frac{\varphi P_{vsat}}{\rho_w R_v T} = \frac{D_{va}}{\mu(\varphi) \cdot R_v T} \cdot \frac{\varphi P_{vsat}}{\rho_w R_v T} \tag{7.3}$$

Fig. 7.11 presents the detailed outputs of the WD scenario for the concrete-CS wall, implemented using the four approaches: V0L0, V0L0_Kv, V0L0_Kl and V1L1. Overall, the results of V0L0 and V0L0_Kv exhibit strong similarity, though slight discrepancies exist, potentially due to fitting variations and numerical precision. Nevertheless, the findings largely support the equivalence of different material property parameters. As expected, V1L1,

which incorporates both vapor and liquid transport, falls between the results of V0L0 and V0L0_Kv (relying solely on vapor transport) and V0L0_Kl (exclusively employing liquid transport). The cumulative total heat flux is shown in Fig. 7.11d, with its two contributing components — enthalpy flux due to vapor diffusion and conductive heat flux at the interior surface — presented in Figs. 7.11e&f, respectively. These correspond to the terms $(L_v + c_v T)g_v$ and $\lambda \nabla T$ in Eq. 2.3. Note that the enthalpy flux due to liquid advection (the term $c_l T g_l$ in Eq. 2.3) — remains zero across all simulation cases, including V0L0_Kl, which is explicitly configured to represent moisture transport exclusively via the liquid phase. This contradicts the intended modeling assumption and suggests that DELPHIN may still internally resolve moisture transport through vapor diffusion, even under configurations designed to suppress it. However, no explanation for this behavior is provided by the model developers.

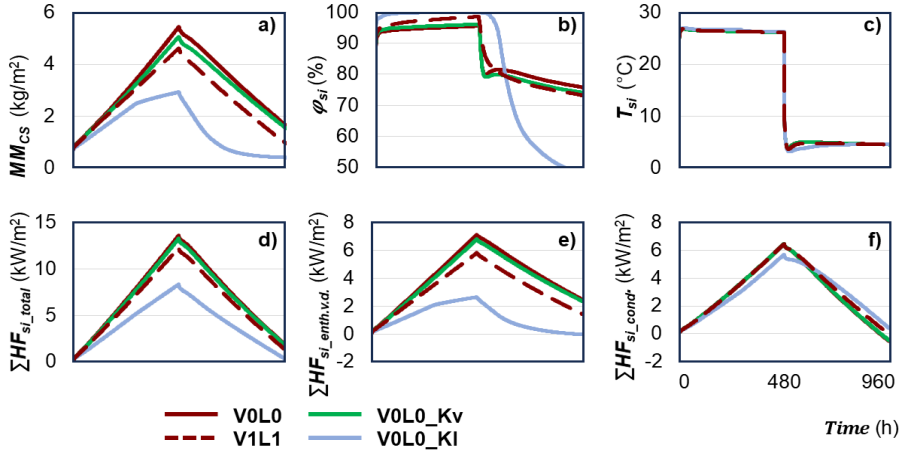


Fig. 7. 11 Simulated a) moisture mass of CS, b) relative humidity, c) temperature, d) cumulative total heat flux, e) cumulative enthalpy heat flux due to vapor diffusion and f) cumulative conductive heat flux at the interior surface in the supplementary simulation of stage 2.

To verify this assumption, an additional comparative scenario WD+WDR is applied to V0L0_Kl, imposing a liquid source of 1 L/(m²·s) at both interior and exterior surfaces. Fig. 7.12a displays the enthalpy heat flux due to liquid advection at the exterior boundary (se), the concrete/CS interface (it) and the interior boundary (si). While the liquid advection at the interior surface remains zero, both the concrete/CS interface and the exterior surface exhibit the effects of liquid water transfer. Fig. 7.12b presents the RH profiles under the WD+WDR scenario, further confirming that liquid migration at the concrete/CS interface originates from the exterior liquid source. Meanwhile, the interior surface, despite being in a prolonged near-saturation state, still

exhibits zero liquid advection. This behavior suggests that DELPHIN may only activate liquid transport mechanisms when an imposed liquid source is present at the exterior boundary. Since rare materials are both capillary-active and vapor-tight, the approach V0L0_Kl is unlikely to be adopted in practice. Nevertheless, computational discrepancies in hygric predictions may still arise among integral and separate approaches for implementing vapor and liquid transport properties, including V0L0, V0L0_Kv and V1L1. These deviations are generated through their impact on heat transfer.

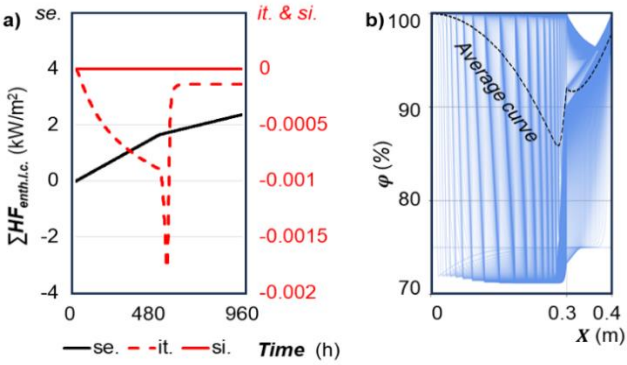


Fig. 7. 12 Simulated a) cumulative enthalpy heat flux due to liquid advection at the exterior surface (se.), concrete/CS interface (it.) and interior surface (si.) and b) relative humidity profiles of WD+WDR scenario applying V0L0_Kl in stage 2.

7.4 Implementation approaches for moisture storage properties

Understanding moisture storage behavior is essential for accurate hygrothermal simulation of porous building materials. While the gravimetric desiccator method is widely used to characterize moisture sorption behavior within the hygroscopic range, it becomes increasingly undependable near saturation due to challenges in controlling the high RH conditions. To address this limitation, HAM model users often resort to: (1) linear extrapolation between the last measured point and the free saturation moisture content, or (2) supplementary methods such as the MIP or the pressure plate tests to enrich the dataset in the over-hygroscopic range (Dang et al. 2025b, 2026). Unlike moisture retention curve, sorption isotherms are typically too steep or narrow to reliably characterize the over-hygroscopic domain, making it critical to assess the precision and relevance of input data for moisture storage functions in this region. This issue is particularly relevant in WUFI, which relies on sorption isotherms and may obscure uncertainties in the over-hygroscopic range, as

observed in the round robin test (Dang et al. 2025b). In contrast, DELPHIN's default use of moisture retention curves may mitigate this risk. Therefore, simulations in this section focus exclusively on WUFI.

WUFI prompts users to input moisture contents at a default set of RH conditions (10 %, 20 %, …, 90 %, 93 %, 95 %, 99 %, 99.5 %, 99.9 %, 99.95 %, 99.99 % and 100 %) though these can be manually modified. When detailed measurement data are unavailable, WUFI offers two additional simplified nonlinear formulas to approximate the curve.

The two-point formula, associated with Eq. 2.11, relies on moisture content values at 80 % and 100 % RH. These points are selected for practical reasons rather than mathematical necessity: equilibrium moisture contents at 80 % RH of materials are widely available.

The three-point formula (see Eq. 7.4), recommended by WUFI's developers (WUFI Forum2), follows a structure that loosely resembles the van Genuchten model (Eq. 2.12, Van Genuchten 1980) to better capture moisture behavior near saturation. The two fitting parameters, pk1 and pk2, are typically derived by calibrating moisture contents particularly near 80 %, 95 % and 100 % RH (Holm et al. 2002). Although not yet implemented in WUFI's interface, this method is documented in their online guidance (WUFI Forum2) and supported by an internal experimental tool "FitFspFkt2" which enables manual fitting via minimization of the sum of squared residuals.

Importantly, the three-point formula is not strictly tied to those specific RH values; they are suggested for convenience still. The accuracy of the curve depends heavily on the proximity of input points to the steep region near saturation. The more data points provided (e.g., RH = 99 %, 99.5 %, 99.9 %, etc.), the better the curve can be constrained — especially near saturation. Practically, without data near RH = 99.9 %, the slope and position of the curve in that region remain poorly defined.

$$w(P_c) = \frac{w_{sat}}{1+\left(\frac{P_c}{pk1}\right)^{pk2}} = \frac{w_{sat}}{1+\left(\frac{\rho_W \cdot R_v \cdot T \cdot ln(\varphi)}{pk1}\right)^{pk2}} \tag{7.4}$$

A central question remains whether these data processing approaches, including simplified formulas and manual fitting, can reliably characterize the moisture storage behavior, particularly in the sensitive over-hygroscopic range. This uncertainty is amplified by the limited availability and precision of experimental data at very high RH range. Furthermore, it is essential to assess how these choices — whether using raw measured data or fitted curves based on the two-point formula, three-point formula or others (Feng et al. 2013) — influence the accuracy of hygrothermal response predictions.

To ensure methodological continuity with previous sections on analyzing implementation strategies for moisture transport properties, the impact assessments concerning moisture storage properties are designated as stages 3 and 4, build upon simulation comparisons using HAMSTAD Benchmark 4 and additional scenarios for concrete-AAC or concrete-CS configurations (see Fig. 7.6) still, under either “extreme” or “moderate” conditions.

Fig. 7.13 illustrates different implementation strategies for the sorption isotherm of the load-bearing material in stage 3. The raw data points are derived from the well-fitted $w(P_c)$ function in the HAMSTAD instruction document (Hagentoft et al. 2004) using Kelvin’s law (Eq. 2.10). Since WUFI requires RH and moisture content to be entered as dual-column data series rather than functional expressions, the density of data points is manually adjusted to ensure a smooth curve, resulting in the reference version of the sorption isotherm. The simplified linear, two-point and three-point curves are equally included. The linear curve adopts the reference values up to 97 % RH (marking the transition between hygroscopic and over-hygroscopic ranges), and then linearly connects to the saturation moisture content. This method, employed by several participants during the round robin validation, reflects an overly simplified implementation strategy (Dang et al. 2025b). The two-point and three-point curves substantially undervalue the moisture storage at low RH levels, despite offering improved accuracy in the over-hygroscopic range. In all scenarios, moisture transport properties are implemented according to the HAMSTAD instruction document, using the given data for μ_{dry} and the $D_w(w)$ function (translated from $K_l(w)$ function). This setup is consistent with the approach D1.0 applied in stage 2.

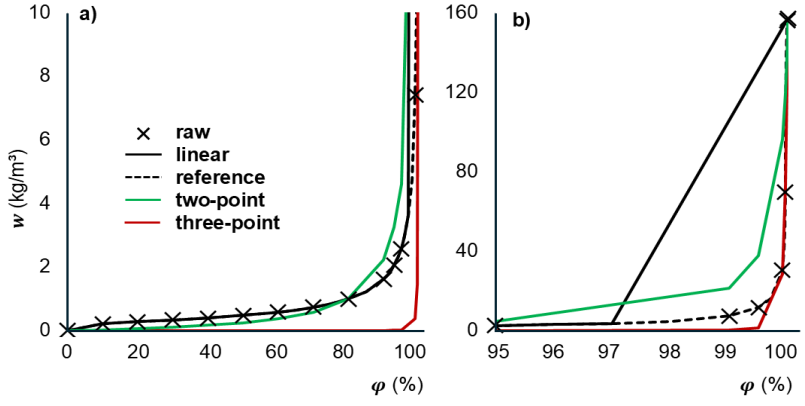


Fig. 7. 13 Implementation approaches for moisture storage properties of the load-bearing material in stage 3.

As shown in Fig. 7.14, the methods for implementing moisture storage properties affect the simulation results of HAMSTAD Benchmark 4 in stage 3. The three-point formula yields moisture content values that closely mirror those derived from the reference curve (Fig. 7.14a). The two-point formula also yields comparable outcomes overall. This consistency arises from the specific boundary conditions for this scenario, characterized by wind-driven rain (WDR) exposure and apparent liquid transport. These conditions mainly give over-hygroscopic behavior, a regime where the performance of both simplified curves proves to be more accurate. However, the linear curve brings about substantial overestimations, reaching up to 10 kg/m^3 (Fig. 7.14a), especially when involving WDR exposure. Temperature predictions at the exterior surface show only minimal variation and are therefore omitted. Fig. 7.14b provides a detailed view of the exterior boundary RH, focusing on the over-hygroscopic range. As anticipated, simulations using the reference and the three-point curves, both associated with lower equilibrium moisture contents in this domain (see Fig. 7.13), reach saturation more quickly and remain saturated for longer periods. In contrast, the two-point and the linear curves result in markedly reduced saturation durations. While the overall differences across the approaches are moderate, they underscore the importance of accurate moisture storage curve, near saturation in this case.

Stage 4 focuses on modeling the sorption behavior of AAC and CS using two simplified isotherm formulas alongside the reference curve as a reference. To simplify data processing, WUFI's default solutions for implementing moisture transport properties are applied to AAC, CS and concrete, i.e., a constant μ_{dry} combined with the $D_w(w)$ function derived from Künzel's formula (Eq. 2.14). This leads to inevitable discrepancies between stages 2 and 4, and therefore the comparisons below are confined to scenario variations in this stage. Figs. 7.15a&c reveal that the three-point formula substantially underestimates moisture storage in the hygroscopic range. However, its performance improves in the over-hygroscopic range, where it aligns more closely with the reference curve (Figs. 7.15b&d). This outcome stems from the criterion used in "FitFspFkt2", which minimizes the sum of squared residuals. In practice, the curve's geometry makes it challenging to achieve a balanced fit across both hygroscopic and over-hygroscopic domains. Focusing the fit on the over-hygroscopic range typically yields a lower residual sum. In contrast, the two-point curve exhibits an under-and-over pattern, intersecting the reference curve at 80 % RH. Below this threshold, it tends to underestimate moisture storage, while above it, it consistently overestimates.

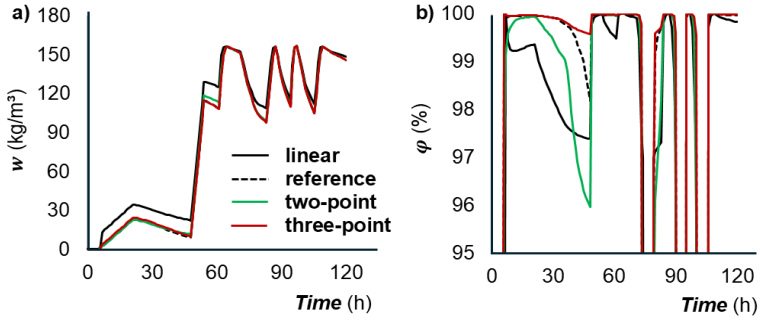


Fig. 7. 14 Simulated a) moisture contents of the load-bearing material and b) RH on the exterior surface in stage 3.

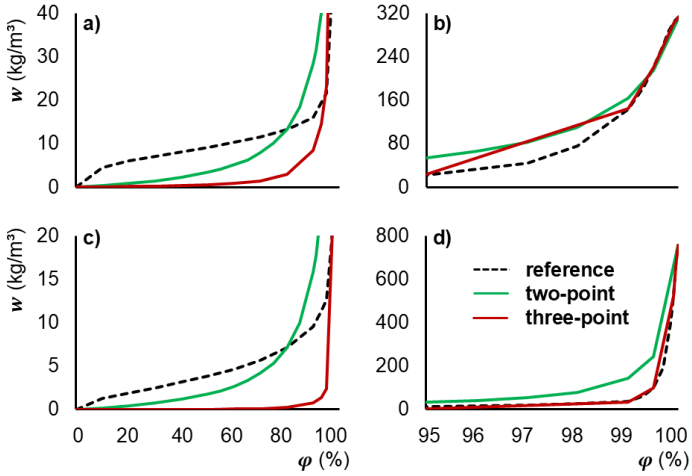


Fig. 7. 15 Implementation approaches for moisture storage properties of a) & b) AAC and c) & d) CS in stage 4.

Figs. 7.16 and 7.17 present the simulated RH profiles and MM time series in stage 4. Overall, the two simplified isotherm formulas do not introduce any significant deviations in RH predictions within the over-hygroscopic range when compared to the reference curve. However, notable discrepancies, up to 20 % RH, are noticed in the lower-humidity range (Figs. 7.16b&g). Regarding MM, both formulas produce time series with similar trend as the reference curve. Regarding MM, both formulas yield time series that follow the general trend of the reference curve but exhibit different degrees of over- and underestimation without a consistent pattern across scenarios (Fig. 7.17).

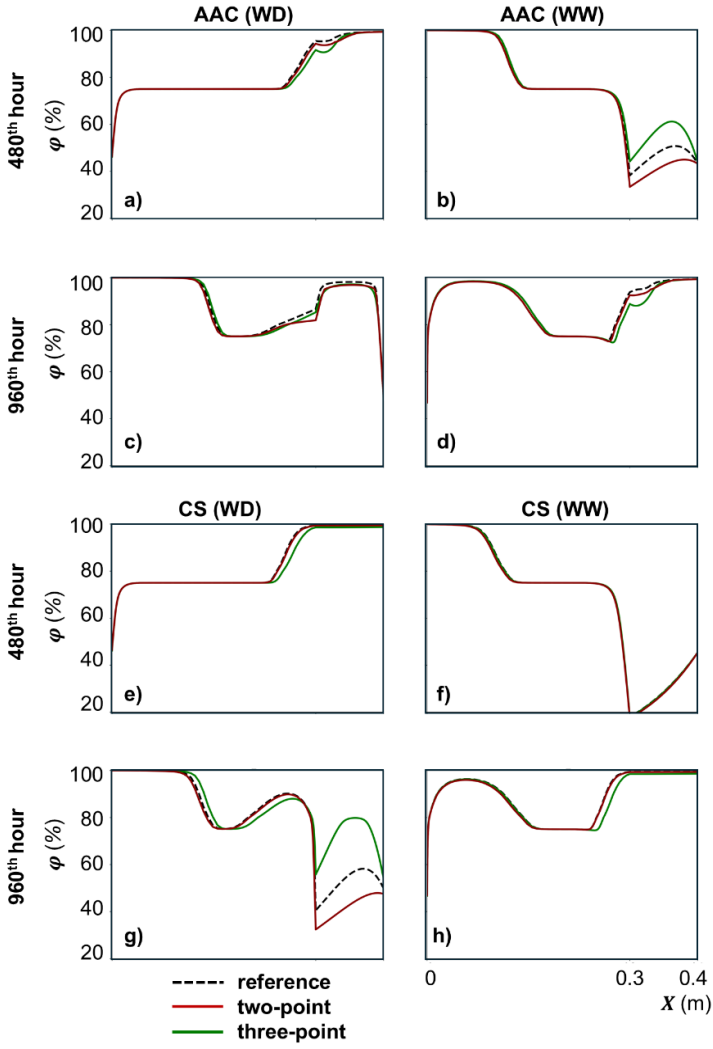


Fig. 7. 16 Simulated RH profiles at the 480th and 960th hours in stage 4.

The analysis of stages 3 and 4 is based on fully characterized moisture storage function of materials, with the reference curve representing accurate behavior derived from ample experimental data. As recommended by Feng and Janssen (2021) and Dang et al. (2025b), this curve combines desiccator test results for the hygroscopic range with MIP or similar techniques for the over-hygroscopic range, followed by fitting and scaling to ensure precision. In practice, however, experimental data for the over-hygroscopic range are not always available, and simplified functions are therefore commonly used.

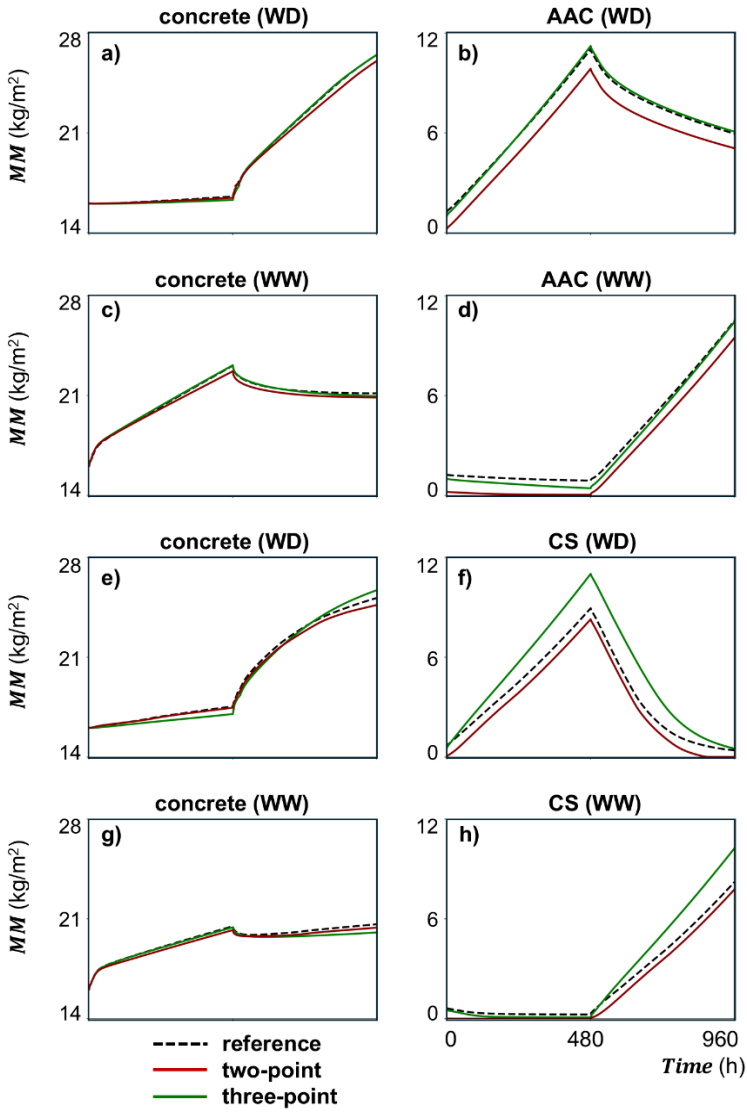


Fig. 7. 17 Simulated MM time series of concrete, CS and AAC in stage 4.

This study examines the impact of two such formulas implemented in WUFI through case studies. The two-point formula, founded on only two characteristic values, may reflect hygroscopic materials, but lacks robustness across diverse material types. Its simplicity can hence be problematic for modeling or estimation without supporting data. The three-point formula better captures the typical steepness and narrowness of sorption isotherms in the over-hygroscopic range but also has inherent limitations in matching the observed values across the full RH spectrum. Although minimizing the sum of

squared residuals is a common fitting criterion, it tends to assign disproportionate weights to regions with larger absolute differences between measured and fitted moisture contents, typically retrieved in the over-hygroscopic range. These regions can dominate the residual sum, leading the optimization to prioritize them at the expense of the lower hygroscopic range. Ironically, the region where accurate data are most readily available. Conversely, in the over-hygroscopic range, where experimental measurements are typically unavailable, the two simplified formulas may offer viable alternative solutions. A tiered strategy is recommended for implementing moisture storage properties. Priority should be given to experimental dataset. Linear extrapolation in the over-hygroscopic range should be avoided unless justified by material behavior or boundary conditions. The two- or three-point formula may be cautiously used, provided input values are selected near the steep region of the sorption isotherm to capture nonlinearity and minimize underestimation risks.

Future work could focus on refining the fitting routines to enable asymmetric error weights for hygroscopic and over-hygroscopic ranges. One promising direction is minimizing the sum of normalized residuals, rather than the absolute squared differences as currently adopted by FitFspFkt2, to reduce high-RH bias and improving overall fit quality. Developing piecewise or hybrid isotherm models may further enhance flexibility near saturation by segmenting the RH domain into tailored regimes. Probabilistic or machine learning-based methods could improve robustness, especially under sparse or noisy data conditions. Further studies should also explore a broader set of numerical scenarios to systematically compare different approaches. Where possible, experimental validation should be adopted as a benchmark to assess the accuracy and practical relevance of the proposed approaches.

Chapter 8 Summary

This part integrated experimental validation and inter-model comparison to assess uncertainties in the implementation of material properties in heat, air and moisture (HAM) models. Based on the hot box-cold box (HB-CB) benchmark dataset, the round robin exercise revealed that while heat transport is consistently predicted, moisture-related outputs are highly sensitive to the definition of moisture storage and transport properties. Correlation and multi-stage evaluation analyses highlighted the influence of user-defined inputs and suggested using moisture mass as an indicator for model validation. Further comparative insights from WUFI and DELPHIN illustrated how modeling strategies affect simulation outcomes. Key implementation challenges — including the translation of liquid transport properties, treatment of vapor–liquid terms and definition of storage functions — were examined through controlled and real-weather scenarios. Discrepancies arise from simplified formulas, software-specific defaults and opaque code structures, which may obscure physical meaning and introduce hidden uncertainties. Overall, predictive accuracy depends not only on theoretical formulation but also on the quality and transparency of material data acquisition and implementation.

Part III Towards real-life applications

While hygrothermal responses of building components under real climate conditions are subject to numerous uncertainties, the implementation of wind-driven rain (WDR) represents one of the most significant factors. This part addresses: (I) the implementation of different semi-empirical methods for WDR calculation into HAM models with specific assumptions and simplifications, and (II) the impacts of these assumptions and simplifications on the accuracy of the predicted hygrothermal responses. The stepwise evaluation consists of two phases. In phase 1, two measured datasets from Leuven (Belgium) and Eindhoven (the Netherlands) are employed to compare multiple semi-empirical methods for WDR calculation in WUFI and DELPHIN. The outcomes are confronted with the measured datasets and manual calculation results. In phase 2, these calculated WDR loads, together with the measured datasets as benchmarks, are applied as imposed fluxes to the same configuration in parallel scenarios to appraise the deviations in hygrothermal responses. The part begins with an introduction to the experimental setups, datasets and geometric configurations, and subsequently proceeds to compare the simulation results of the two phases using different methods.

This part is largely based on Dang et al. (2024a, 2025e).

Chapter 9 The in-situ experimental setups and datasets

This chapter firstly introduces two in-situ experimental setups and datasets from Leuven (Belgium) and Eindhoven (the Netherlands) used for assessing the implementation of wind-driven rain (WDR) in heat, air and moisture (HAM) models and its impact on hygrothermal predictions.

9.1 The WDR experimental setups and datasets

While experimental datasets from small-scaled setups are presented as the "correct answer" in previous comparison and validation studies on WDR prediction, long-term WDR measurements of real-world buildings are rare. Beyond the inherent differences between these semi-empirical methods, additional uncertainties arise from specific simplifications in implementing these methods into HAM models. To further evaluate these impacts on predicted WDR loads and hygrothermal responses, two dedicated experimental datasets are introduced below.

The first experimental setup is located at the KU Leuven VLIET experimental building (referred to as "VL") in Leuven, Belgium (50.53° N, 4.42° E) (Blocken and Carmeliet, 2002, 2007; Desta et al. 2011). The measured meteorological data and the hygrothermal response of the southwest-oriented (aligned with the prevailing local wind direction) masonry walls from January to December 2019 are used (Vereecken et al. 2020; Vereecken and Roels 2021a, 2021b). As shown in Fig. 9.1, the test area with the six wall sections under an overhanging sloped roof are separated by well insulated vapor tight wooden frames. Three wall-mounted WDR gauges (collection area: 0.2 m × 0.2 m) are placed between the wall sections, but only the measured data of the top rain gauge is used because the data of the other gauges are either incomplete or erroneous. Theoretically, the difference in measured water amounts between two consecutive time steps should be zero in the absence of rain, or positive when rain occurs. However, negative values may appear due to evaporation and measurement errors. To eliminate these influences, momentary WDR

values are set to zero. Solar radiation, horizontal rainfall and wind velocity are recorded by a weather station on the flat roof and a meteorological mast positioned in the front free field. The climatic data is presented in Fig. 7.3.



Fig. 9. 1 Outdoor view of the VLIET experimental Building (VL).

The second dataset is based on the monitoring at the main building of TU/e (Eindhoven University of Technology) (referred to as "MB") in Eindhoven (the Netherlands, 51.45° N, 5.48° E) from September 1998 to September 1999. In contrast to the small low-rise VL building, this dataset is collected at a much larger 45 m high west-oriented facade (Fig. 9.2). Rain gauges in different sizes (0.032 - 0.527 m^2) and shapes (round and rectangle) had been placed at both center (C) and edge (E) at 38.8 m height from 1997 to 1999 for validating early semi-empirical and CFD models (Van Mook 2003). The wind velocity and horizontal rain are measured by a weather station 127 m to the west (Van Mook 2002). The meteorological wind speed at 10 m is processed from data of an anemometer at 38.8 m with an empirical wind speed profile coefficient (Van Mook 1999).

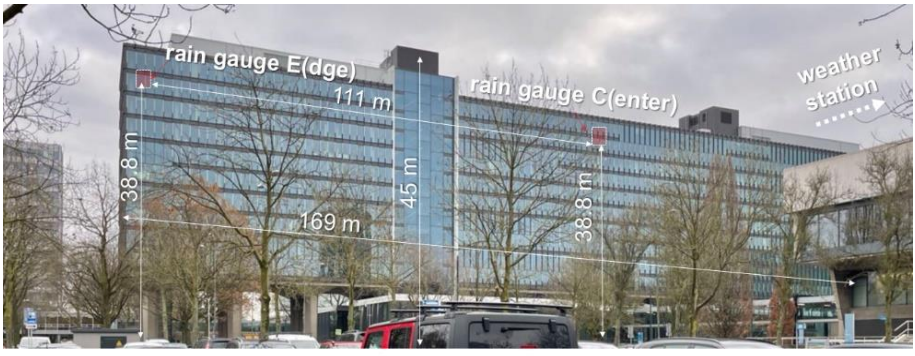


Fig. 9. 2 Outdoor view of the main building (MB) of the TU/e.

Monitored hourly weather conditions at VL and MB are presented in Figs. 7.3 and 9.3 respectively. The data of MB in 1998 are placed after the data in 1999 to present a continuous, synthetic one-year dataset. The relative humidity and solar radiation at MB are not measured and instead displayed by reference data (Visual crossing; Doutreloup et al. 2022).

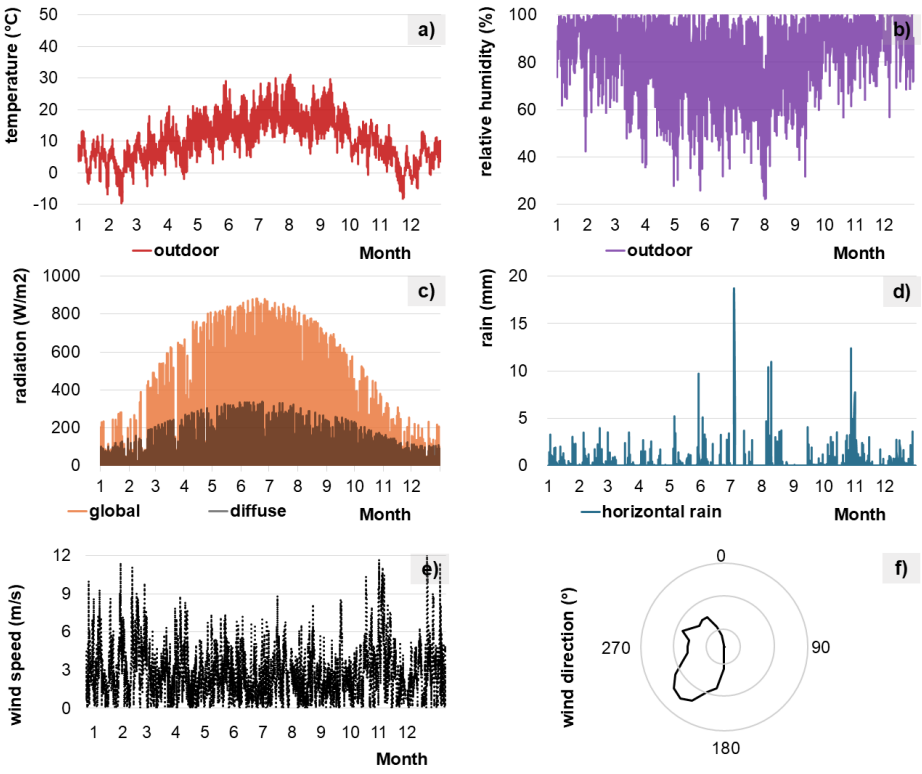


Fig. 9. 3 Weather conditions at MB: a) temperature, b) relative humidity, c) solar radiation, d) horizontal rain, e) wind speed, and f) wind direction.

9.2 Geometric configuration

In phase 2, the geometric configuration of HAMSTAD Benchmark 4 (Hagentoft et al. 2004) is applied (Fig. 7.1a). All inputs except for the boundary conditions remain the same as the benchmark instruction.

Chapter 10 Assessing the implemented semi-empirical methods for WDR calculation in WUFI and DELPHIN

This chapter compares various semi-empirical methods for wind-driven rain (WDR) calculation implemented in WUFI and DELPHIN (Dang et al. 2024a). In phase 1, simulated WDR loads are compared against measured datasets and manual calculation results using the same assignments in the semi-empirical methods. These simulated WDR loads, along with the measured results, are then applied as boundary conditions for the HAMSTAD Benchmark 4 in phase 2, to illustrate the deviations in predicted hygrothermal responses.

10.1 Impact on WDR loads

Table 2.1 outlines five approaches to quantify WDR loads in WUFI and DELPHIN. In phase 1, the measured datasets at VL and MB (see Figs. 7.3 & 9.3) serve as boundary conditions for three semi-empirical methods, hereafter denoted as "W1" (WUFI 1, Eq. 2.24), "W2" (WUFI 2, Eq. 2.25) and "D1" (DELPHIN 1, Eq. 2.23). The other two methods, WUFI 3 and DELPHIN 2, are not considered since they impose WDR loads directly. For reference, manual calculations using identical parameter assignments are performed in Excel. WUFI 1 aligns with ASHRAE 160, except for the orientations of the walls that can only be selected from eight typical choices (North, Northeast, East, etc.) instead of arbitrary angles. DELPHIN claims ISO compliance but uses fixed parameter values (C_R = 1.007, C_T = 1.0, O = 0.8, and W = 0.4) for all scenarios (Fechner 2020a) which may introduce bias. Rain absorption is treated via an adhering fraction in WUFI (default: 0.7 for walls) and via an exposure coefficient in DELPHIN (default: 1.0), with equivalence achieved through manual adjustment in versions earlier than DELPHIN 6.1.6.

The assignment of WDR-related parameters in phase 1 is shown in Table 10.1. These parameters are (I) "user-defined" (users can enter arbitrary values based on real scenarios or prior insights), sometimes with "default" values, or

(II) "coordinated" (fixed values according to the matched spatial and topographical characteristics in the standards), or (III) "predefined" (integrated into the scripts and unchanged; or automatically calculated based on internal physical/mathematical relations). The simulations reproduce an "engineering" approach, relying on "default" or "coordinated" values, with limited insights on the modeling logics and experimental expertise. Notably, WDR outputs differ: WUFI reports unadjusted "rain (exterior climate)" whereas DELPHIN applies an exposure coefficient. For consistency, WUFI results are manually scaled using the assigned adhering fraction in Table 10.1.

Table 10. 1 Assignments for WDR-related parameters in phase 1.

Cases	Effective fraction of WDR	Spatial and topographical coefficients
W1	Adhering fraction = 0.7 ("default").	F_E = 1.0 (VL) or 1.5 (MB), F_D = 0.5 (VL) or 1.0 (MB) ("coordinated").
W2		R_1= 0 (VL & MB), R_2 = 0.07 (VL) or 0.2 (MB) ("default").
D1	Exposure coefficient = 0.7 ("user-defined").	C_R = 1.007, C_T = 1.0, O = 0.8, W = 0.4 ("predefined").

Fig. 10.1 illustrates violin plots of the ratios between model-based and manual WDR load calculations at each consecutive time step over one year. Overall, both models roughly reproduce the original formula since the mean and medium values of the ratios approximate 1 for both cases. There are more underestimations than overestimations in WUFI, while relatively more overestimations are observed in DELPHIN. Fig. 10.2 compares the modelled and measured WDR loads. The modelled and measured cumulative WDR loads roughly present similar trends (Fig. 10.2a&b), but the deviations are case-specific. For VL, D1 provides the closest match between the modelled and measured cumulative WDR loads, whereas W1 and W2 underestimate the measured cumulative WDR by 36 % and 55 % respectively. For MB, the modelled cumulative WDR loads by the ASHRAE-method and WUFI's alternative method are several times larger than that by the ISO-method, in tune with findings by Zhou et al. (2023), and all methods overestimate the measured cumulative WDR loads. All methods can under- and over-estimate the momentary WDR loads by 2 orders of magnitude (Fig. 10.2c&d).

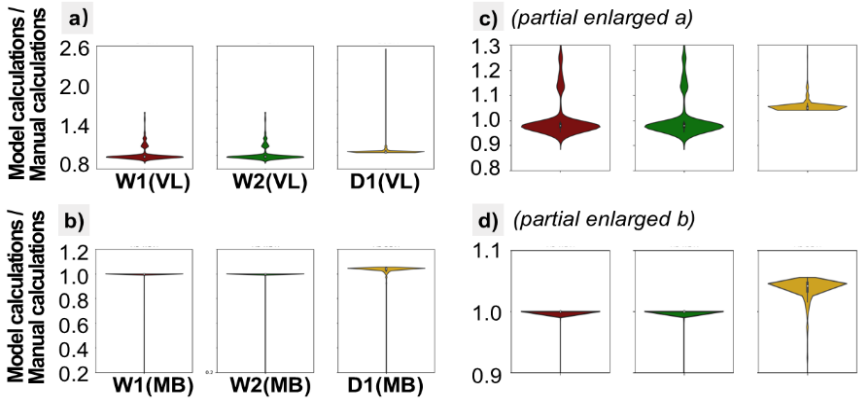


Fig. 10. 1 Ratios of model calculations and manual calculations of WDR loads at a) & c) VL and at b) & d) MB.

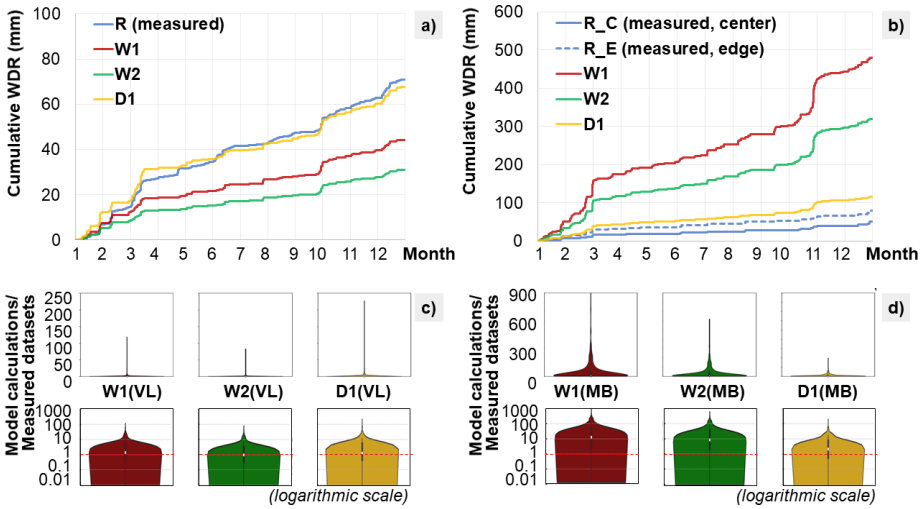


Fig. 10. 2 Measured (R) and simulated (W1, W2 and D1) cumulative WDR loads at a) VL and at b) MB, and the ratios of modelled and measured momentary WDR at c) VL and at d) MB.

10.2 Impact on hygrothermal responses

In phase 2, the geometric configuration (Fig. 7.1), material properties, surface coefficients and initial conditions of HAMSTAD Benchmark 4 (Hagentoft et al. 2004) are employed. The outdoor temperature, relative humidity (RH) and solar radiation as measured at VL and MB (see Figs. 7.3 & 9.3) are implemented as the exterior boundary conditions respectively, in combination with the calculated WDR loads from phase 1 as imposed fluxes in different

scenarios. The measured indoor temperature and RH at VL are also used as boundary conditions for the cases related to MB. The simulated hygrothermal responses of the new reference case R, resulting from the measured WDR loads (for VL: the top rain gauge; for MB: the average of the two rain gauges), are compared with the results from the three phase 1 cases (W1, W2, D1). To avoid any impact of intrinsic differences between WUFI and DELPHIN, all four cases are all simulated in one model. Note that the focus for phase 2 is to evaluate the discrepancy in hygrothermal responses triggered by varied WDR loads calculated by different semi-empirical methods, instead of attributing the deviations in WDR loads to specific implementations in the two models (as addressed in phase 1). DELPHIN is selected primarily because the original material property data is directly compatible with its input format, whereas WUFI requires additional conversion. Despite the recognition that employing WUFI might yield slightly different outcomes, due to inherent differences between the two models (e.g., implementation of material properties), the primary task is to highlight that WDR predictions from different HAM models can influence the hygrothermal responses. Integrated moisture mass and moisture content profiles, cumulated heat loss, mold growth risk and frost damage risk are employed as indicators for analysis. The output time steps for time series data and for profiles are 1 h and 1 day, respectively.

10.2.1 Integrated moisture masses and moisture content profiles

Moisture mass evolution indicates the integrated moisture content over the full width of a certain material layer, while the overlaid (daily) moisture profiles illustrate the overall moisture absorption and penetration for a whole year. Table 10.2 and Fig. 10.3 show the moisture masses of the load-bearing material and the moisture content profiles of the whole structure, using the calculated and measured WDR loads at VL as imposed fluxes. While D1 provides much closer predicted annual WDR loads to the measured datasets than W1 & W2 (Fig. 10.2a), the order is reversed in Figs. 10.3b-e. The moisture profiles of W1 & W2 express similar patterns to that of the reference case, while the penetration in D1 goes deeper and increases the moisture content of the inner structure (Fig. 10.3b-e). This can be presumably explained by the moisture mass peaks of D1 during heavy rain events in spring (see Figs. 10.2a, 10.2c & 10.3a), which drive up the average moisture masses (avg.) of D1 (0.1262 kg/m^2) in contrast to R (0.0928 kg/m^2). Similar increase can be found in the 75 % percentile (P75) of W1's moisture masses (0.1009 kg/m^2), which exceeds that of case R (0.0896 kg/m^2).

Table 10. 2 Data characteristics of the moisture masses of the load-bearing material at VL.

Indicators	R	W1	W2	D1
P25	0.0541	0.0541	0.0537	0.0546
P75	0.0896	0.1009	0.0853	0.1225
Avg.	0.0928	0.0989	0.0818	0.1262

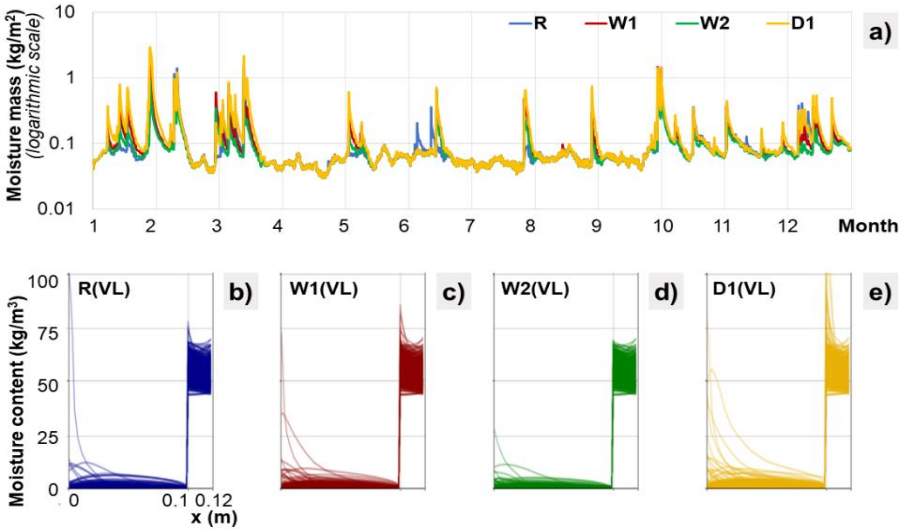


Fig. 10. 3 VL: a) moisture masses of the load-bearing material, and b) – e) moisture content profiles of the whole structure.

Table 10.3 and Fig. 10.4 show the moisture masses of the load-bearing material and moisture content profiles of the whole structure, using predicted and measured WDR loads at MB as imposed fluxes. The significant overestimations of WDR loads in W1 and W2 (see Fig. 10.2b&d) bring about significant moisture absorption and penetration, even leading to complete saturation (see Fig. 10.4c&d). The magnitude sequence of absorbed moisture, W1 > W2 > D1 > R, remains the same order of predicted WDR loads. Since the disparity among predicted WDR loads is overwhelmingly large, the difference among moisture masses behaves similarly. The 75 % percentile of moisture contents in W1 can be even up to 17 times of the reference case R (Table 10.3).

Table 10. 3 Data characteristics of the moisture masses of the load-bearing material at MB.

Indicators	R	W1	W2	D1
P25	0.0618	0.1376	0.1049	0.0661
P75	0.1102	1.9018	0.7552	0.2147
Avg.	0.1194	1.8976	1.1839	0.2493

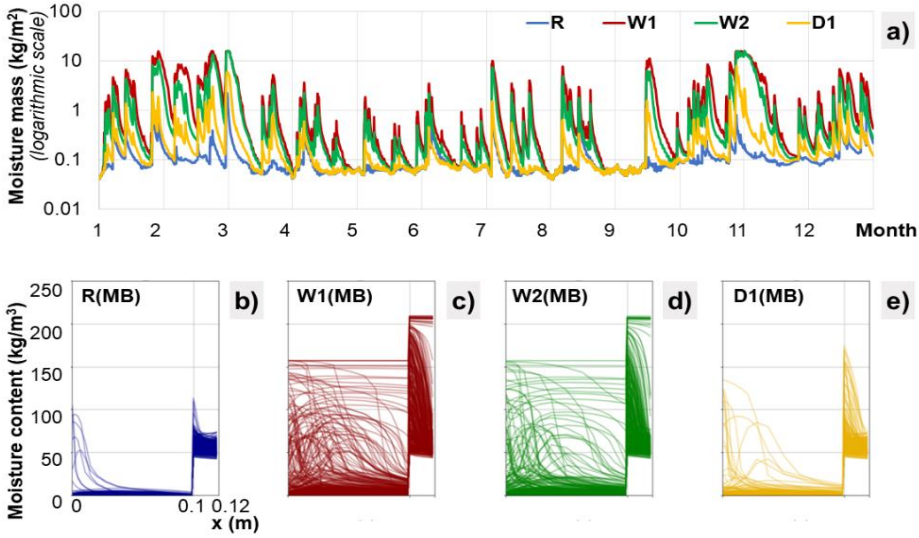


Fig. 10. 4 MB: a) moisture masses of the load-bearing material, and b) – e) moisture content profiles of the whole structure.

10.2.2 Heat losses

Heat loss, as unintentional energy dissipation, is equivalent to the heat compensation (generated by indoor heating system) for the outward heat flow to maintain the indoor temperature. Heat loss increases when the material buffers more moisture and/or has larger thermal conductivity. As Fig. 10.5 shows, the difference among the heat losses in VL cases is limited, while the WDR effect on heat loss is significant in MB cases. D1 provides the closest prediction of annually cumulative heat loss to the reference case, while annual overestimations of 66.3 and 43.8 kW/m^2 are made by W1 and W2 respectively.

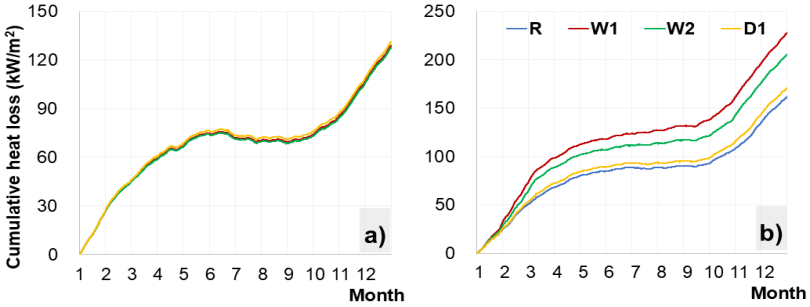


Fig. 10. 5 Cumulative heat losses at a) VL and at b) MB.

10.2.3 Mold growth risks

Mold growth, as an indicator of biological failures, depends on temperature, RH, pH, lighting, etc. (Vereecken and Roels 2012). The mold spore germination isopleths proposed by Sedlbauer (2001) are applied to evaluate the predicted risks on the interior surface in Figs. 10.6 and 10.7. The indications of the critical lines in days are the mold spore germination intervals, and more points lying above these lines indicate more serious biological risks. There is no clear difference in VL cases. In MB cases, D1 gives the closest predictions to case R, while W1 and W2 both provide significant overestimations.

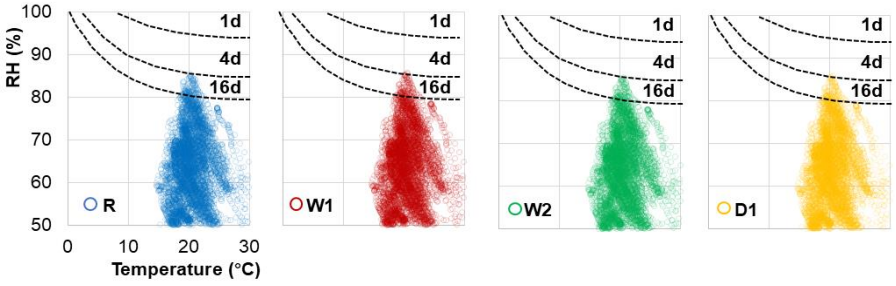


Fig. 10. 6 Mold growth risks on the interior surface at VL.

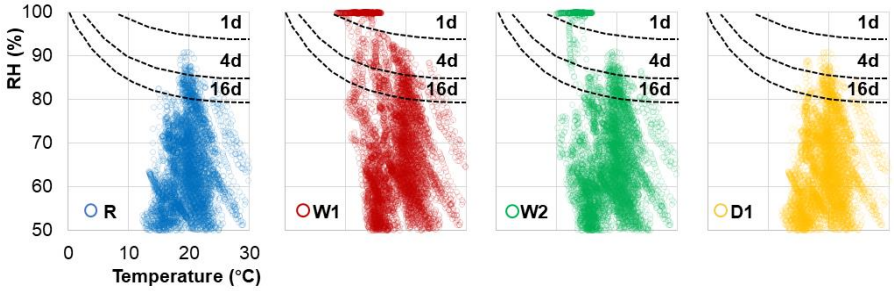


Fig. 10. 7 Mold growth risks on the interior surface at MB.

10.2.4 Frost damage risks

Frost damage, caused by volumetric moisture changes during freeze-thaw cycles in pores, may lead to cracks, flaking and other structural deteriorations (Zhou et al. 2021). To evaluate the frost damage risks, the indicators proposed by Straube and Burnett (2000) are adopted (Tijskens et al. 2019). Two criteria should be met: (I) temperature at 0.5 cm thickness from the exterior surface fluctuates around zero degrees, and (II) the local moisture content at the same depth is larger than 25 % saturation moisture content.

Figs. 10.2a&b indicate that WDR exposure at MB is substantially higher than at VL, providing sufficient liquid moisture supply to meet the second criterion. This explains the absence of risk points in VL and the presence of frost risk at MB, as shown in Fig. 10.8. A large amount of risk points appears in case W1, due to its significant overestimation of WDR loads. The moisture contents at negative temperatures of case W2 are dramatically higher than those in case D1, which remain close to the prediction in the reference case R. It should be noted that this assessment relies on simplified indicators and does not fully capture the complexity of actual frost damage mechanisms; rather, it serves to compare relative risks across scenarios only.

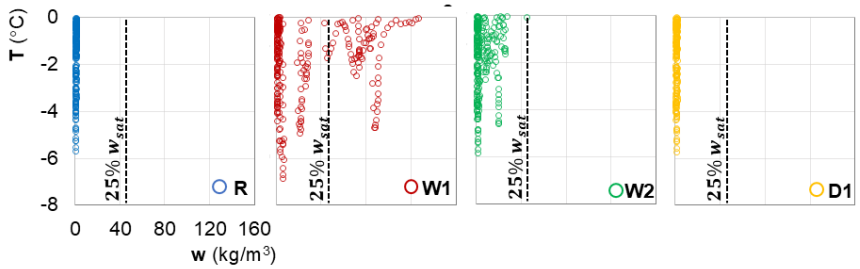


Fig. 10. 8 Frost damage risks at 0.5 cm from the exterior surface at MB.

Chapter 11 Summary

This part expanded HAM model validation by evaluating how different methods for wind-driven rain (WDR) calculation affect hygrothermal predictions. Unlike previous studies that primarily compared WDR loads, this work also examined the impact of these approaches, along with their underlying assumptions and simplifications in WUFI and DELPHIN, on simulation outcomes. The results demonstrated that even when annual WDR loads appear similar across methods, hygrothermal behavior can vary significantly, particularly in moisture-sensitive assemblies or under extreme weather conditions. These discrepancies arise from model-specific parameters and limitations in the modeling simplifications. Moreover, both tools neglect horizontal spatial variability, which further limits prediction accuracy. Two key insights emerge: uncertainties in boundary conditions must be assessed via response-based analysis, and WDR implementation details can critically shape results. By reframing WDR as a modeling issue rather than a meteorological input, this study advocates for more context-aware boundary condition handling in hygrothermal assessments.

Part IV Conclusion

This part first synthesizes the thesis's key contributions in both methodological advancement and practical insight. First, it shows how the quality assessment of heat, air and moisture (HAM) models is enhanced through a multi-phase international validation campaign anchored in a benchmark experimental dataset. Second, it recapitulates critical uncertainties in HAM modeling — such as the sensitivity of simulation outputs to material properties, the reliability of wind-driven rain (WDR) calculations and the influence of algorithmic biases and user decisions — which have been investigated via in-depth comparative simulations. These findings collectively strengthen the scientific foundation of HAM simulations and enhance their practical relevance, offering both conceptual rigor and actionable guidance for model developers and practitioners. At the same time, this part acknowledges several limitations that remain outside the scope of the current investigation, including challenges in representing geometric complexity, defining initial and surface conditions and addressing the numerical trade-offs hidden behind the interfaces. These reflections inform a forward-looking research agenda that advocates for a shared infrastructure to support model refinement, transparency and collaborative benchmarking.

This part is partially based on Dang et al. (2023a, 2023b, 2024a, 2024b, 2025a, 2025b, 2025c, 2025d, 2025e, 2026).

Chapter 12 Key contributions and insights

Heat, air and moisture (HAM) models are essential for simulating the hygrothermal behavior of building components in both research and engineering applications. However, their reliability and robustness are often undermined by assumptions, simplifications and approximations introduced during model development and implementation. Despite their widespread use, a key challenge persists: the lack of a systematic and rigorous work to evaluate whether these models can accurately and reproducibly reflect real-world physical phenomena. This thesis directly addressed that challenge by proposing a stepwise and comprehensive assessment scheme that explicitly considers uncertainties in implementing material properties and boundary conditions, stemming from both intrinsic model limitations and user-induced factors. The preceding chapters have documented the benchmark datasets, the round robin validation process and in-depth simulation results. Building upon these investigations, this chapter synthesizes the key scientific contributions of this work and practical insights for HAM model developers and users.

12.1 Scientific contributions

This thesis resolved three core research questions by: revealing how internal model configurations and inconsistent user practices jointly drive divergence in simulation outcomes; demonstrating that variations in material properties and boundary conditions can significantly influence simulated hygrothermal responses; and proposing concrete improvements to enhance model reliability and robustness. These findings support more informed modeling decisions and lay the groundwork for broader efforts to improve transparency and reproducibility in HAM simulation.

The major contributions of this thesis are twofold: (1) the integration of key assessment approaches into a coherent methodology toolkit for assessing HAM model reliability and robustness, demonstrated through a stepwise and comprehensive evaluation process; and (2) the development and open release of benchmark experimental datasets, showcased in an international round-

robin validation campaign and designed to support further model assessment and sensitivity analysis.

12.1.1 Methodological synthesis and assessment showcase

This thesis first synthesized the previously fragmented approaches for HAM model assessment (verification, validation, inter-model comparison and sensitivity analysis) into a unified, interpretable sequence of evaluation tasks. It extended the traditional notion of validation beyond empirical reproduction to encompass comparative and diagnostic elements that clarify both model performance and user impact. Building on this synthesis, the thesis examined existing assessment practices in component-scale HAM modeling, identifying limitations such as restricted configuration scales, insufficient material diversity, simple hygrothermal process and incomplete documentation.

To address these issues, this research proposed and demonstrated a stepwise and comprehensive approach that operationalizes the methodological synthesis in practice. The approach combines experimental validation, inter-model comparison and input–output attribution analysis (interpretable as a form of sensitivity assessment) across progressively complex boundary conditions and modeling scenarios from controlled laboratory tests to real-climate field exposures. By systematically increasing environmental and modeling complexity, this progression allowed the isolation and quantification of uncertainties in implementing material properties and boundary conditions. Comparative analyses involving multiple models, users and implementation strategies demonstrated that even formally standardized formulations may lead to divergent results, due to inherent model constraints and variability in input interpretation. The thesis not only exposed critical limitations in current HAM modeling practices but also demonstrated the practical value of a transparent, replicable and interpretable assessment protocol: one capable of guiding future model development, supporting benchmarking and enhancing confidence in simulation-based decision-making.

12.1.2 Benchmark datasets and round robin validation efforts

A second major contribution of this thesis is the development and open release of high-quality benchmark experimental datasets for empirical HAM model validation and inter-model comparison.

The primary dataset, derived from the dedicated Hot Box–Cold Box (HB–CB) experiment, includes measured hygrothermal material properties, surface transport coefficients and boundary conditions. It addresses long-standing

limitations of earlier datasets and demonstrates its scientific value through its central role in the most extensive international round-robin validation campaign to date, titled "*Empirical Validation of HAM Models Based on a Dedicated HB–CB Experiment*". This initiative unprecedently engaged 38 research groups from 19 countries, yielding over 70 simulation contributions and significantly surpassing previous efforts such as the EU HAMSTAD project. This campaign enabled consistent evaluation of different HAM models under identical conditions. Participants reproduced the measured hygrothermal behavior using their respective models and parameter interpretations, allowing systematic identification of model-specific discrepancies and user-induced variability. The assessment combined experimental validation, inter-model comparison and correlation analysis, resulting in a comprehensive diagnosis of uncertainties in current HAM modeling practices.

The second set of dedicated benchmark datasets was developed to address unresolved uncertainties, particularly those related to wind-driven rain (WDR). This subsequent set not only broadened the validation scope to include real climatic exposures, but also enabled a targeted assessment of how different WDR calculation methods affect hygrothermal simulation outcomes.

Collectively, these efforts establish a precedent for international benchmarking and collaborative model assessment. By providing open, high-fidelity datasets with thoroughly documented simulation results, this thesis offers a replicable template for future assessment.

12.2 Practical insights

This section distills practical guidance for both the model developers and users regarding the uncertainties in (1) implementing material properties, (2) implementing WDR and (3) biases inherent to specific models.

12.2.1 Uncertainties in implementing material properties

Understanding and mitigating uncertainties in determining hygric properties is critical for HAM modeling. These uncertainties not only arise from intra-operator repeatability, inter-operator reproducibility and material heterogeneity, but also stem from limitations in experimental instrumentation and the inherent difficulty of characterizing certain materials (e.g., fiber-based materials with complex moisture transport behavior). While these influences are often unavoidable, their potential impact warrants careful consideration

and mitigation through rigorous methodological design. Inconsistencies arising from manufacturing variations or intrinsic variability further complicate the process. These challenges are especially evident in commercial HAM models, where reliance on built-in databases and flexible user assignments often amplifies discrepancies in outcomes. However, the sensitivity of simulation outcomes to how these properties are defined has often been overlooked.

Table 12.1 addresses this gap by cross-referencing material types with moisture exposure scenarios, highlighting the hygric properties most crucial to simulation outcomes. It clarifies when hygroscopic versus over-hygroscopic storage functions require precise characterization, when vapor transport property alone is largely sufficient, when liquid transport must be supplemented and where measurement-based derivations are preferable to empirical formulas. The moisture exposure scenarios are classified into: (1) **hygroscopic sorption** (in most "service" conditions, e.g., 30 % - 90 % RH), and (2) **mixed** (hygroscopic and over-hygroscopic) **sorption** with occasional condensation (e.g., 70 % - 100 % RH) or with intense liquid exposure like WDR. In terms of hygric properties, building materials are generally categorized into four types according to their vapor openness ("V"), capillarity ("C") and hygroscopicity ("H"). **Type 1** (hygroscopic, vapor-permeable and capillary-active) is represented by moisture buffering materials such as calcium silicate (CS) and autoclaved aerated concrete (AAC), and other porous mineral substances. **Type 2** (hygroscopic, vapor-permeable and with limited capillarity) is commonly associated with porous organic composites like wood fiber board (WF) and similar bio-based products. **Type 3** (non-hygroscopic, vapor-permeable and with limited/no capillarity) can be exemplified by moisture resistant insulation materials like mineral wool (MW). **Type 4** (non-hygroscopic, vapor-tight and with limited/no capillarity) mainly involves vapor retarder/barrier materials like aluminum foil, polyethylene (PE) film, extruded polystyrene (XPS) and polyvinyl chloride (PVC) membranes. This categorization reflects the materials examined in this thesis and the author's experience. As hygric properties may vary considerably within the same category of materials, the classification should be regarded as indicative rather than definitive. For instance, clay bricks may range from nearly non-hygroscopic to clearly hygroscopic. Yet, regardless of such variability, desiccator tests remain advisable whenever available, as they provide reliable sorption data. Expanded polystyrene (EPS), by contrast, is generally regarded as "vapor-permeable" though may exhibit high vapor diffusion resistance (Marincioni et al. 2025). Even in such cases, the cup test remains a practical solution, since it produces values regardless of magnitude.

Table 12. 1 Sensitivity matrix of HAM simulation.

Material types	V	C	H	Moisture exposures	Highlights
Type 1	√	√	√	Hygroscopic sorption	• Moisture storage functions $w(\varphi)$ or $w(P_c)$ should be precisely characterized in the hygroscopic range, while those in the over-hygroscopic range are not that sensitive (linear extrapolation to the saturation moisture content may be applied). [Sections 5.2, 6.3, 7.4] • A dependent vapor transport function $\mu(\varphi)$ or $K_v(w)$ is often enough without implementing a supplementary liquid transport function. [Sections 5.2, 6.3, 7.1, 7.3]
				Mixed sorption	• Moisture storage functions $w(\varphi)$ or $w(P_c)$ should be precisely characterized both in the hygroscopic and the over-hygroscopic range (the three-point formula may be applied). [Sections 5.2, 7.4] • A dependent vapor transport function $\mu(\varphi)$ or $K_v(w)$ should be accompanied with a supplementary liquid transport function $D_w(w)$ or $K_l(w)$. Wherever possible, results derived from measurements (X-ray + Boltzmann transformation; or the ruler method) are more advisable than Kunzel's formula for the dual diffusivity functions. [Sections 5.2, 7.1, 7.2, 7.3]
Type 2	√	×	√	Hygroscopic sorption	• Moisture storage functions $w(\varphi)$ or $w(P_c)$ should be precisely characterized in the hygroscopic range, while those in the over-hygroscopic range are not that sensitive (linear extrapolation to the saturation moisture content may be applied). [Sections 5.2, 6.3, 7.4] • A dependent vapor transport function $\mu(\varphi)$ or $K_v(w)$ is often enough without implementing supplementary liquid transport function. [Section 5.2, 6.3]
				Mixed sorption	• Moisture storage functions $w(\varphi)$ or $w(P_c)$ should be precisely characterized both in the hygroscopic and the over-hygroscopic range. [Section 5.2, 6.3] • A dependent vapor transport function $\mu(\varphi)$ or $K_v(w)$ should be accompanied with a supplementary liquid transport function $D_w(w)$ or $K_l(w)$. [Sections 5.2, 6.3]

Type 3	√	×	×	All scenarios	• Moisture storage in the hygroscopic range is negligible so the functions $w(\varphi)$ or $w(P_c)$ may be linearly interpolated, with a simple linear connection with saturation moisture content. [Section 5.2] • A vapor transport property derived from the dry cup test μ_{dry} or equivalent $K_{v,dry}$ is often enough without implementing supplementary liquid transport function [Section 5.2]
Type 4	×	×	×		

Admittedly, the matrix provides only general guidance, since the moisture exposure scenarios and material classifications by hygric properties are inherently not strict and context dependent. Sensitivity of hygrothermal predictions to hygric properties is also influenced by geometric configurations and coupled processes such as heat transfer. Consequently, the strategies outlined in the matrix should be applied cautiously rather than regarded as absolute rules. Nevertheless, one certainty remains: while simplified formulations may improve computational efficiency, they risk obscuring nuanced hygrothermal behavior. The transition between hygroscopic and over-hygroscopic regimes therefore warrants particular attention, as it represents the critical threshold between vapor-phase and liquid-phase transport and strongly influences the accuracy of long-term performance predictions.

Where feasible, the use of extensive measurement data is encouraged over reliance on simplified equations. Both model developers and users are advised to consult the methodologies and recommendations presented in this thesis to enhance model assessment and optimize material property implementation. Two additional recommendations are worth reiterating. First, moisture mass should be prioritized as a validation indicator, as it more accurately captures the model's capacity to reproduce dynamic moisture behavior and more clearly reveals the influence of implemented material properties than temperature or relative humidity. Second, the "equivalent permeability" K_{v+l} [s] (Dang et al. 2025b) is advised to unify input parameters across varying driving potentials and modeling approaches, particularly when comparing simulation strategies or conducting sensitivity analyses of material properties. Ultimately, HAM modeling involves complex, coupled heat and moisture transport processes, with underlying physical mechanisms that remain only partially understood. Given this complexity, it is neither feasible to exhaustively explore all exposure scenarios nor to precisely quantify the influence of every implementation strategy. These constraints can lead to discrepancies in

model outputs that are difficult to interpret — making transparency in data transformation essential for ensuring traceability and scientific credibility.

12.2.2 Uncertainties in implementing WDR

This thesis extended its scope to WDR implementation under real-world climate conditions. While previous research has focused on calculating WDR loads using various semi-empirical methods, limited attention has been paid to how embedded assumptions and simplifications within these methods propagate through simulations and influence hygrothermal predictions. Modeling practices such as discretized orientation schemes, fixed exposure coefficients and idealized aerodynamic factors contribute to this uncertainty.

This thesis argues that the annual cumulative WDR metric is inadequate for capturing the complexity of short-term hygrothermal behavior. Transient wetting cycles, often critical to localized moisture distribution and capillary transport behavior, are obscured by long-term averages. To address this, it is essential to zoom in high-resolution temporal profiles that reveal "critical" events and evaluate their impact on hygrothermal responses. This perspective calls for a reconceptualization of WDR in HAM modeling: not merely as a static external input, but as a dynamic driver of moisture behavior. Shifting from input-based to response-based evaluation emphasizes the importance of tracking moisture accumulation and drying processes over time.

Additionally, due to WDR's stochastic nature, semi-empirical methods tend to produce context-sensitive inaccuracies, leading to potential over- or underestimations. These limitations become particularly pronounced when involving complex geometries or localized exposure conditions, where simplified assumptions may fail to capture critical moisture dynamics. Given the scarcity of field measurements, comparisons across semi-empirical models and/or with computational fluid dynamics (CFD) results are recommended.

12.2.3 Uncertainties related to model biases

Beyond assessments related to specific parameters, this study also identified limitations embedded within WUFI and DELPHIN. They often function as "black box" systems, with hidden assumptions and internal mechanisms that are neither fully documented nor clearly communicated to users.

For WUFI, simplifications intended to enhance user-friendliness may come at the cost of precision. In addition to the limitations of Künzel's formula for dual-mode liquid diffusivity, this thesis found that user-defined moisture

storage curves require high-resolution input data to be effective; otherwise, the integrated two-point formula with overly simplified fitting, which limits the accuracy representation of material behavior. For WDR modeling, WUFI discretizes building orientation into eight fixed directions, adding another layer of simplification to an already empirical approach.

DELPHIN, while more detailed in some respects, also imposes structural constraints. A notable issue is the enforcement of monotonicity across all physical functions, which, although numerically convenient, may not align with physical evidence. The internal handling of vapor and liquid transport processes remains insufficiently transparent, making it difficult to evaluate how coupled moisture mechanisms are represented. Furthermore, DELPHIN often applies fixed values for WDR-related parameters, regardless of context-specific factors, limiting its adaptability to real-world conditions.

The study also raised concerns about deeper, systemic risks. Even well-established HAM models embed algorithmic decisions that shape simulation behavior in ways users cannot easily detect or control. This lack of transparency undermines the assumption of model neutrality and complicates efforts to compare results across models or replicate published findings.

12.2.5 Summary reflection

HAM model users bring varied expertise to the modeling process — ranging from practitioners relying on databases to researchers conducting their own measurements and data processing. Meanwhile, the embedded assumptions, simplifications and approximations in the model formulation are not consistently documented by developers. This lack of consistency and transparency complicates the pursuit of desired simulation outcomes: users may struggle to recognize and address sources of uncertainty, while developers may find it difficult to anticipate how models will be interpreted or applied. To mitigate these challenges, this study proposes a pragmatic baseline strategy. Modeling should begin with identifying the dominant sorption processes relevant to the application context and prioritizing which properties require precise characterization. Reference data must be handled cautiously due to batch variability and limited reproducibility. Experimental validation and sensitivity analysis are recommended. For boundary conditions such as WDR, where direct measurement is rarely feasible, surrogate strategies like inter-model comparison can offer practical input estimates, though their impact on simulation outcomes requires close examination.

Chapter 13 Limitations and outlook

Despite the comprehensive scope of this thesis, several limitations remain. These limitations not only delineate the boundaries of the current work but also point toward promising avenues for future research. This chapter outlines key areas where further investigation is warranted.

13.1 Geometry and material heterogeneity

This thesis focused primarily on simulations involving homogeneous materials and regular geometries, which are common in laboratory settings and simplified modeling scenarios. However, real-world applications, particularly in the context of historical or deteriorated structures, often involve complex geometries and heterogeneous material properties (Vereecken and Roels 2013; Bottino-Leone et al. 2021). Features such as corners, edges, cracks and material degradation introduce spatial variability that challenges the assumptions of material homogenization and dimensional reduction. In addition, masonry walls are frequently modeled as one-dimensional assemblies using a single representative material, thereby neglecting the influence of mortar joints and interfacial capillary effects. Even in two-dimensional models, the hydraulic interactions between bricks and mortar, such as interface permeability and contact angle variations, are difficult to capture accurately. These complexities introduce uncertainties that are not addressed in this thesis but merit dedicated investigation. Future research should explore how geometric discontinuities and material heterogeneity affect moisture transport and thermal behavior, and how these effects can be realistically incorporated.

13.2 Initial and surface conditions

Initial conditions critically influence the accuracy of hygrothermal simulations (Reuge et al. 2020), especially in short-term or transient scenarios such as rainfall or rapid temperature fluctuations. While long-term simulations may

gradually dampen initialization effects, transient phenomena remain highly sensitive to initial distribution of moisture and temperature. In this thesis, initial conditions were carefully controlled or estimated from monitored data and refined through pre-runs to minimize their impact. However, such precision is not always feasible in practice. Similarly, surface heat and moisture transport coefficients represent another important source of uncertainty in HAM modeling (Steskens et al. 2009). These coefficients are often influenced by environmental factors such as wind speed, surface roughness and ambient conditions. Inaccurate or overly simplified assumptions may lead to significant deviations in predicted surface fluxes, particularly under dynamic boundary conditions. In this study, surface coefficients were addressed through measurements, but simplifications were still applied, most notably the use of the Lewis relation. While this approach might be suitable under the controlled and idealized boundary conditions of the present research, many real-world scenarios involve far greater variability and complexity. Transient surface exchanges may exhibit nonlinear and time-dependent behavior that warrants further investigation. Given the limitations of controlled boundary conditions and simplified assumptions adopted in this study, future work should focus on advancing both the estimation of initial conditions and the dynamic modeling of surface transport processes, particularly in transient contexts.

13.3 Algorithmic trade-offs behind the interfaces

Another area not explicitly addressed in this thesis concerns the numerical uncertainties embedded in algorithms. These include grid discretization, time step selection and convergence criteria — factors that can significantly influence simulation accuracy but are often overlooked by users. While finer spatial and temporal resolutions generally improve numerical precision, they also increase computational cost, necessitating trade-offs between accuracy and efficiency. Moreover, many users may be unaware of the mathematical approximations and simplifications embedded in commercial software or custom codes. These “hidden” uncertainties can lead to divergent results even when input parameters are nominally identical. Future research should investigate how numerical settings affect simulation outcomes and develop guidelines for balancing computational performance with predictive fidelity.

13.4 Towards a shared infrastructure for HAM model advancement

This thesis presents a thorough assessment of HAM models, recognizing that it is not feasible to address all sources of uncertainty within a single study. The round robin validation primarily targets uncertainties in material property implementation, while subsequent chapters extend the analysis to boundary conditions such as wind-driven rain (WDR). Other influential factors — including air leakage, radiation exchange and construction defects — remain beyond the current scope. In addition, the diversity of modeling approaches, user interpretations and simulation objectives complicate the development of universally applicable assessment protocols. More fundamentally, the complexity of heat and moisture transfer makes comprehensive model assessment inherently difficult. Each benchmark dataset can only isolate a limited set of factors — such as material properties or boundary conditions — while simplifying others. Although this thesis offers a detailed and well-structured validation showcase, many uncertainties remain unresolved. Addressing these challenges will require stronger international collaboration and open access to benchmark experiments that reflect real-world complexity. Additionally, transparent documentation of modeling assumptions and numerical methods will enable deeper insights into the interactions between physical processes, computational algorithms and user decisions. Establishing a shared infrastructure is essential to unlocking the full potential of HAM simulations in promoting energy efficiency, moisture safety and climate resilience in the built environment.

Bibliography

Abuku, M. (2009). Moisture Stress of Wind-Driven Rain on Building Enclosures, PhD Thesis, KU Leuven, Belgium.

Adan, O., Brocken, H., Carmeliet, J., Hens, H., Roels, S., & Hagentoft, C. E. (2004). Determination of liquid water transfer properties of porous building, materials and development of numerical assessment methods: introduction to the EC HAMSTAD project. Journal of Building Physics, 27(4), 253-260.

Aït Oumeziane, Y., Pierre, A., El Mankibi, F., Lepiller, V., Gasnier, M., & Désévaux, P. (2021). Hygrothermal properties of an early 20th century clay brick from eastern France: Experimental characterization and numerical modelling. Construction and Building Materials, 273, 121763.

Alioua, T., Agoudjil, B., & Boudenne, A. (2019). Numerical study of heat and moisture transfers for validation on bio-based building materials and walls. In: Proceedings of the 1st International Conference on Numerical Modelling in Engineering: Volume 1 Numerical Modelling in Civil Engineering, NME 2018, 28-29 August 2018, Ghent University, Belgium, pp. 81-89.

Amorim, M., de Freitas, V. P., & Torres, I. (2024). Influence of moisture on the energy performance of retrofitted walls-experimental assessment and validation of an hygrothermal model. International Journal of Architectural Heritage, 18(3), 477-491.

ANSI/ASHRAE. (2002). Guideline 14-2002 Measurement of Energy and Demand Savings.

ASHRAE 160. (2016). Criteria for Moisture-Control Design Analysis in Buildings.

ASHRAE. (2013). Chapter 26: Heat, air, and moisture control in building assemblies— material properties. In: ASHRAE (ed.) ASHRAE Handbook of Fundamentals. Atlanta, GA: ASHRAE, pp. 26.2–26.20.

Asli, M., Sassine, E., Brachelet, F., & Antczak, E. (2021). Hygrothermal behavior of wood fiber insulation, numerical and experimental approach. Heat and Mass Transfer, 57, 1069-1085.

Aude, P., Tabary, L., & Depecker, P. (2000). Sensitivity analysis and validation of buildings' thermal models using adjoint-code method. Energy and buildings, 31(3), 267-283.

Berger, J., Gasparin, S., Dutykh, D., & Mendes, N. (2017). Accurate numerical simulation of moisture front in porous material. Building and Environment, 118, 211-224.

Bianchi Janetti, M. (2018). Moisture absorption in capillary active materials: analytical solution for a multiple step diffusivity function. Transport in Porous Media, 125(3), 633-645.

Blocken, B., & Carmeliet, J. (2002). Spatial and temporal distribution of driving rain on a low-rise building. Wind & structures, 5(5), 441-462.

Blocken, B., & Carmeliet, J. (2004). A review of wind-driven rain research in building science. Journal of wind engineering and industrial aerodynamics, 92(13), 1079-1130.

Blocken, B., & Carmeliet, J. (2006). On the validity of the cosine projection in wind-driven rain calculations on buildings. Building and Environment, 41(9), 1182-1189.

Blocken, B., & Carmeliet, J. (2007). Validation of CFD simulations of wind-driven rain on a low-rise building facade. Building and Environment, 42(7), 2530-2548.

Blocken, B., Dezsö, G., van Beeck, J. P. A. J., & Carmeliet, J. (2009). The mutual influence of two buildings on their wind-driven rain exposure and comments on the obstruction factor. Journal of Wind Engineering and Industrial Aerodynamics, 97(5-6), 180-196.

Blocken, B., & Carmeliet, J. (2010a). Overview of three state-of-the-art wind-driven rain assessment models and comparison based on model theory. Building and Environment, 45(3), 691-703.

Blocken, B., Dezsö, G., van Beeck, J. P. A. J., & Carmeliet, J. (2010b). Comparison of calculation models for wind-driven rain deposition on building facades. Atmospheric environment, 44(14), 1714-1725.

Bottino-Leone, D., Larcher, M., Troi, A., & Grunewald, J. (2021). Hygrothermal characterization of a fictitious homogenized porous material to describe multiphase heat and moisture transport in massive historic walls. Construction and Building Materials, 266, 121497.

Brambilla, A., Sangiorgio, A. (2021). Moisture and Buildings: Durability Issues, Health Implications and Strategies to Mitigate the Risks. Cambridge, UK: Woodhead Publishing.

Budaiwi, I., El-Diasty, R., & Abdou, A. (1999). Modelling of moisture and thermal transient behaviour of multi-layer non-cavity walls. Building and Environment, 34(5), 537-551.

Burch, D. M., Tsongas, G. A., Thornton, B. A., & Walton, G. N. (1996). Computer Analysis of the Moisture Performance of Roof Constructions in the US DOE Moisture Control Handbook.

Busser, T., Berger, J., Piot, A., Pailha, M., & Woloszyn, M. (2018). Comparison of model numerical predictions of heat and moisture transfer in porous media with experimental observations at material and wall scales: an analysis of recent trends. Drying Technology.

Canadian Mortgage and Housing Corporation. (2003). Review of hygrothermal models for building envelope retrofit analysis. Research Highlights. Technical Series 03-128. Ottawa: Canadian Mortgage and Housing Corporation.

Carbonez, K., Van Den Bossche, N., Ge, H., & Janssens, A. (2015). Comparison between uniform rain loads and point sources to simulate rainwater leakage with commercial HAM-models. In: Proceedings of the International Symposium on Building Pathology, Porto, Portugal, pp: 1-8.

Carmeliet, J., Hens, H., Roels, S., Adan, O., Brocken, H., Cerny, R., Pavlik, Z., Hall, C., Kumaran, K. and Pel, L. (2004). Determination of the liquid water diffusivity from transient moisture transfer experiments. Journal of Thermal Envelope and Building Science, 27(4), 277-305.

Caurie, M. (1970). A new model equation for predicting safe storage moisture levels for optimum stability of dehydrated foods. International Journal of Food Science & Technology, 5(3), 301-307.

Chakraborty, D., & Elzarka, H. (2018). Performance testing of energy models: are we using the right statistical metrics? Journal of Building Performance Simulation, 11(4), 433-448.

Chang, W. J., & Weng, C. I. (2002). Heat and mass transfer in porous material. In Transport phenomena in porous media II (pp. 257-275). Pergamon.

Chen, C., Zhang, H., Feng, C., Xuan, Y., Qian, T., & Xie, J. (2022). Analysis of wind-driven rain characteristics acting on building surfaces in Shanghai

based on long-term measurements. Journal of Building Engineering, 45, 103572.

Chung, D., & Wen, J. (2019). Building envelope moisture transport in the context of assembly aging and uncertainty. Technology| Architecture+ Design, 3(2), 221-233.

Chung, D., Wen, J., & James Lo, L. (2020). Development and verification of the open source platform, HAM-tools, for hygrothermal performance simulation of buildings using a stochastic approach. Build Simulation, 13 (3): 497–514.

Colinart, T., Lelièvre, D., & Glouannec, P. (2016). Experimental and numerical analysis of the transient hygrothermal behavior of multilayered hemp concrete wall. Energy and Buildings, 112, 1-11.

Colinart, T., & Glouannec, P. (2016). Accounting for the temperature dependence in the sorption isotherms in the prediction of hygrothermal behavior of hemp concrete. In: Proceedings of Central European Symposium on Building Physics, Dresden, Germany.

Cook, R. A., & Hover, K. C. (1993). Mercury porosimetry of cement-based materials and associated correction factors. Construction and Building Materials, 7(4), 231-240.

Corcoran, L., Duffy, A., & Rouholamin, S. (2013). A hygrothermal analysis of international timber frame wall assemblies tested under temperate maritime climatic conditions. In: Proceedings of Central European Symposium for Building Physics 2013, Vienna, Austria, pp: 1-8.

Cornick, S., Maref, W., & Tariku, F. (2009). Verification and validation: establishing confidence in hygrothermal tools.

Dang, X.*, Janssen, H., & Roels, S. (2023a). Hygrothermal Modelling of one-dimensional Wall Assemblies: inter-model Validation between WUFI and DELPHIN. Journal of Physics: Conference Series. 2654(1), 012040.

Dang, X.*, Janssen, H., & Roels, S. (2023b). Comparative simulations on hygrothermal performance of calcium silicate and wood fiber as capillary active internal insulation materials. In: 2nd International Conference on Moisture in Buildings 2023. ScienceOpen.

* The bolded references highlight the author's scientific contributions pertinent to the scope of this PhD research (*: corresponding author).

Dang, X.*, Vereecken, E., Janssen, H., & Roels, S. (2024a). Impact of semi-empirical methods implemented in heat, air, and moisture (HAM) models on predicted wind-driven rain (WDR) loads and hygrothermal responses. Building and Environment, 262, 111770.

Dang, X.*, Janssen, H., & Roels, S. (2024b). A comprehensive benchmark dataset for the validation of building component heat, air, and moisture (HAM) models. Building Simulation. 17(11), 1893–1907.

Dang, X.*, Janssen, H., & Roels, S. (2024c). Empirical validation of HAM-models based on a dedicated HB-CB experiment_datasets [Data set]. Zenodo. https://doi.org/10.5281/zenodo.10998834.

Dang, X.*, Janssen, H., & Roels, S. (2025a). User preferences, biases and/or mistakes as uncertainties in hygrothermal simulations: insights from a round robin test. In: Berardi, U. (eds) Multiphysics and Multiscale Building Physics. IABP 2024. Lecture Notes in Civil Engineering, vol 552: pp. 68-75. Springer, Singapore.

Dang, X.*, Guimarães, A. S., Sarkany, A., Laukkarinen, A., Xu, B., Vanderschelden, B., Rode, C., Xia, C., Feng, C., Whitman, C., Deckers, D., Yang, H., Fechner, H., Sharma, H., Ge, H., Xie, H., Zhang, H., Vandemeulebroucke, I., Mazura, J., Xie, J., Madera, J., Grunewald, J., Vinha, J., Janssens, K., Fukui, K., Mourkos, K., Wang, L., Bart, M., Morelli, M., Tenpierik, M., Abuku, M., Defo, M., Janetti, M. B., Klõšeiko, P., Sekki, P., Kopecký, P., Matiasovsky, P., Paolini, R., Slávik, R., Cerny, R., Akhavan Shams, S., Moissette, S., Kalamees, T., Freitas, T. S., Colinart, T., Bednar, T., Bunch-Nielsen, T., Koci, V., Marincioni, V., Kukk, V., Gan, W., Chen, X., Hu, X., Plantec, Y., Xie, Y., Huijbregts, Z., Janssen, H., Roels, S. (2025b). A state-of-the-art empirical round robin validation of heat, air and moisture (HAM) models. Building and Environment, 276, 112867.

Dang, X.*, Janssen, H., & Roels, S. (2025c). Impact of implementation approaches for moisture transfer properties in the hygroscopic range. Presented at: CESBP2025. (Accepted).

Dang, X.*, Janssen, H., & Roels, S. (2025d). Implementation strategies and uncertainties of moisture transport properties in heat, air and moisture (HAM) models: Comparative insights from WUFI and DELPHIN. Journal of Building Physics. (Under review).

Dang, X.*, Vereecken, E., Janssen, H. & Roels, S. (2025e). Hygrothermal response of masonry facades with vapor-tight or capillary-active internal insulation under current and future climate scenarios. Built Heritage. 9, 23.

Dang, X.*, Janssen, H., & Roels, S. (2026). Assessing Simplified Modelling Strategies for Sorption Isotherms in WUFI. Presented at: NSB2026. (Under review).

Darcy, H. (1856). Les Fontaines Publiques de la Ville de Dijon, Dalmont, Paris. (In French).

Defo, M. (2018). hygIRC: review of the implementation of a hygrothermal simulation model. National Research Council Canada. Construction, Ottawa, Canada.

Defo M., Lacasse M. A., Sahyoun S., Moore T. V. (2019). Impacts of wind-driven rain calculation methods on the moisture performance of wood-frame walls. In ASHRAE Topical Conference Proceedings, 573-581.

Defo, M., Lacasse, M., & Laouadi, A. (2022). A comparison of hygrothermal simulation results derived from four simulation tools. Journal of Building Physics, 45(4), 432-456.

Defraeye, T., Blocken, B., & Carmeliet, J. (2013). Influence of uncertainty in heat–moisture transport properties on convective drying of porous materials by numerical modelling. Chemical Engineering Research and Design, 91(1), 36-42.

DELPHIN. https://bauklimatik-dresden.de.

Delgado, J. M. P. Q., Ramos, N. M., Barreira, E., & De Freitas, V. P. (2010). A critical review of hygrothermal models used in porous building materials. Journal of Porous Media, 13(3).

Delgado, J. M., Barreira, E., Ramos, N. M., & De Freitas, V. P. (2012). Hygrothermal numerical simulation tools applied to building physics. Springer.

Desta, T. Z., Langmans, J., & Roels, S. (2011). Experimental data set for validation of heat, air and moisture transport models of building envelopes. Building & Environment, 46(5), 1038-1046.

Diamond, S. (2000). Mercury porosimetry: an inappropriate method for the measurement of pore size distributions in cement-based materials. Cement and concrete research, 30(10), 1517-1525.

Dieckmann, J. H., & Heinrich, H. (2008). Energiespeicherbeton–ein Beton mit integriertem Latentwärmespeichermaterial. Bauphysik, 30(3), 137-142.

DIN 4108. (2013). Wärmeschutz und Energie-Einsparung in Gebäuden. (In German).

Dos Santos, G. H., & Mendes, N. (2009). Heat, air and moisture transfer through hollow porous blocks. International Journal of Heat and Mass Transfer, 52(9-10), 2390-2398.

Doutreloup, Sébastien, Xavier Fettweis, Ramin Rahif, Essam Elnagar, Mohsen S. Pourkiaei, Deepak Amaripadath, and Shady Attia. Historical and future weather data for dynamic building simulations in Belgium using the regional climate model MAR: typical and extreme meteorological year and heatwaves. Earth System Science Data 14, no. 7 (2022): 3039-3051.

EN 15026. (2004). Hygrothermal performance of building components and building elements - Assessment of moisture transfer by numerical simulation.

EQUA. https://www.equa.se/en/ida-ice.

Evangelides, C., Arampatzis, G., & Tzimopoulos, C. (2010). Estimation of soil moisture profile and diffusivity using simple laboratory procedures. Soil science, 175(3), 118-127.

Evangelides, C., Arampatzis, G., Tsambali, A. A., et al. (2018). Moisture estimation in building materials with a simple procedure. Construction and Building Materials, 164: 830–836.

Fechner, H. (2020a). Numerical simulation of coupled heat and mass transfer in porous building materials - Basics of simulation software DELPHIN Interfaces and boundary conditions. (Internal document).

Fechner, H. (2020b). Material Editor – Manual. https://bauklimatik-dresden.de/delphin/2nd/doc/DELPHIN6_1_MaterialEditor_en.pdf.

Feng, C., Meng, Q., Janssen, H., & Feng, Y. (2013). Effect of temperature on the sorption isotherm and vapor permeability. In: 2nd central European symposium on building physics.

Feng, C., Janssen, H., Feng, Y., & Meng, Q. (2015). Hygric properties of porous building materials: Analysis of measurement repeatability and reproducibility. Building and Environment, 85, 160-172.

Feng, C., & Janssen, H. (2016). Hygric properties of porous building materials (II): Analysis of temperature influence. Building and Environment, 99, 107-118.

Feng, C., Guimares, A. S., Ramos, N., Sun, L., & Janssen, H. (2020). Hygric properties of porous building materials (VI): a round robin campaign. Building and Environment, 185, 107242.

Feng, C., & Janssen, H. (2021). Hygric properties of porous building materials (VII): Full-range benchmark characterizations of three materials. Building and Environment, 195, 107727.

Ferroukhi, M. Y., Abahri, K., Belarbi, R., Limam, K., & Nouviaire, A. (2016). Experimental validation of coupled heat, air and moisture transfer modeling in multilayer building components. Heat and mass transfer, 52(10), 2257-2269.

Fick, A. (1995). On Liquid Diffusion (Reprinted from the London, Edinburgh, and Dublin Philosophical Magazine and Journal of Science, Vol 10, Pg 30, 1855). Journal of Membrane Science, 100(1), 33-38.

Fourier, J. B. J. (1878). The analytical theory of heat. The University Press.

Franzoni, E. (2014). Rising damp removal from historical masonries: a still open challenge. Construction and Building Materials, 54, 123-136.

Freiesleben-Hansen P. (1985). Coupled moisture/heat transport in cross-sections of structures, Denmark: Beton og Konstruktionsinstituttet (BKI). (In Danish).

Fukui, K., & Takada, S. (2024). Impact of air entrapment on capillary absorption in porous building materials. Journal of Building Physics, 48(3), 318-339.

Funk, M., & Wakili, K. G. (2008). Driving potentials of heat and mass transport in porous building materials: a comparison between general linear, thermodynamic and micromechanical derivation schemes. Transport in porous media, 72(3), 273-294.

Furmaniak, S., Gauden, P. A., Terzyk, A. P., Wesołowski, R. P., & Rychlicki, G. (2005). Improving fundamental ideas of Dubinin, Serpinsky and Barton–Further insights into theoretical description of water adsorption on carbons. Annales UMCS (Sectio AA, Chemia), 60, 151-182.

Galbraith, G. H. (1992). Heat and mass transfer within porous building materials. PhD Thesis, University of Strathclyde, Glasgow, UK.

Gan, W., Li, X., Fang, J. & Feng, C. (2025). Influence of input uncertainty on the 1-D hygrothermal simulation of composite walls in China. Building Simulation, 18, 19-32.

Geving, S., Karagiozis, A., & Salonvaara, M. (1997). Measurements and two-dimensional computer simulations of the hygrothermal performance of a wood frame wall. Journal of Thermal Insulation and Building Envelopes, 20(4), 301-319.

Gholamalipour, P., Ge, H., & Stathopoulos, T. (2022). Wind-driven rain (WDR) loading on building facades: A state-of-the-art review. Building and Environment, 109314.

Glaser, H. (1958). Temperatur und Dampfdruckverlauf in einer homogenen Wand bei Feuchteausscheiding. Kältetechnik, 174e81. (In German).

Good, R. J., & Mikhail, R. S. (1981). The contact angle in mercury intrusion porosimetry. Powder Technology, 29(1), 53-62.

Grint, N., Marincioni, V., & Elwell, C. A. (2020). Sensitivity and Uncertainty analyses on a DELPHIN model: The impact of material properties on moisture in a solid brick wall. In: E3S Web of Conferences, Vol. 172, pp. 04006.

Grunewald. J. (1997). Diffusiver und konvektiver Stoff- und Energietransport. PhD Thesis, University of Technology Dresden, Germany.

Grunewald, J., Häupl, P., & Bomberg, M. (2003). Towards an engineering model of material characteristics for input to ham transport simulations-Part 1: an approach. Journal of Thermal Envelope and Building Science, 26(4), 343-366.

Guo, X. G., Chen, Y. M., & Deng, Y. Q. (2012). Development and experimental validation of a one-dimensional dynamic hygrothermal modeling based on air humidity ratio. Journal of Central South University, 19(3), 703-708.

Hagentoft, C.E, Blomberg, T. (2000). 1D-HAM Coupled Heat, Air and Moisture Transport in Multi-layered Wall Structures.

Hagentoft, C. E. (2002). HAMSTAD WP2: Reference document basic modelling physics. Gothenburg, Department of Building Physics, Chalmers University of Technology.

Hagentoft, C. E., Kalagasidis, A. S., Adl-Zarrabi, B., Roels, S., Carmeliet, J., Hens, H., Grunewald, J. Funk, M. Becker, R. Shamir, D. Adan, O. Brocken, H. Kumaran, K. Djebbar, R. (2004). Assessment method of numerical prediction models for combined heat, air and moisture transfer in building components: benchmarks for one-dimensional cases. Journal of thermal envelope and building science, 27(4), 327-352.

Hamdaoui, M. A., Benzaama, M. H., El Mendili, Y., & Chateigner, D. (2021). A review on physical and data-driven modeling of buildings hygrothermal behavior: Models, approaches and simulation tools. Energy and Buildings, 251, 111343.

Häupl P., Stopp. H. (1987). Feuchtetransport in Baustoffen und Bauwerksteilen. PhD Thesis, University of Technology Dresden, Germany. (In Germany).

Hejazi, B., Sakiyama, N. R., Frick, J., & Garrecht, H. (2019). Hygrothermal simulations comparative study: assessment of different materials using WUFI and DELPHIN software. In: Proceedings of the 16th IBPSA International Conference, Rome, Italy, pp: 2-4.

Henderson, S. M. (1952). A basic concept of equilibrium moisture. Agricultural Engineering. 33: 29-32.

Hens, H., (1996). International Energy Agency. Annex 24: Heat, Air and Moisture Transfer in Insulated Envelope Parts. Final report. Task 1: Modelling, Vol. 1, KU Leuven.

Hens, H. (2007). Modeling the heat, air, and moisture response of building envelopes: What material properties are needed, how trustful are the predictions? In: Heat-Air-Moisture Transport: Measurements on Building Materials. ASTM International.

Hens, H. (2009). IEA-ECBCS Annex 41 Whole Building Heat, Air and Moisture. KU Leuven, Belgium.

Hens, H. (2015). Combined heat, air, moisture modelling: a look back, how, of help? Building and Environment, 91, 138-151.

Hofheinz, A., Walker, R., Purcell, C. E., & Kinnane, O. (2025). The hygrothermal properties of historic bricks: Case study of traditional brick construction material in Ireland. Building and Environment, 270, 112491.

Holm, A., Krus, M., & Künzel, H. M. (2002). Approximation der Feuchtespeicherfunktion aus einfach bestimmbaren Kennwerten. Fraunhofer-Institut für Bauphysik. (In German).

Holm, A. H., & Kuenzel, H. M. (2002). Practical application of an uncertainty approach for hygrothermal building simulations—drying of an AAC flat roof. Building and Environment, 37(8-9), 883-889.

Hoppestad, S. (1955). Slagregn i Norge (Driving rain in Norway). NBI Rep, 13.

Huerto-Cardenas, H. E., Leonforte, F., Aste, N., Del Pero, C., Evola, G., Costanzo, V., & Lucchi, E. (2020). Validation of dynamic hygrothermal simulation models for historical buildings: State of the art, research challenges and recommendations. Building and environment, 180, 107081.

Hukka, A., & Viitanen, H. A. (1999). A mathematical model of mould growth on wooden material. Wood science and technology, 33(6), 475-485.

Islahuddin, M., & Janssen, H. (2019). Pore-structure-based determination of unsaturated hygric properties of porous materials. Transport in Porous Media, 130(3), 675-698.

Issaadi, N., Nouviaire, A., Belarbi, R., & AiT-Mokhtar, A. (2015). Moisture characterization of cementitious material properties: assessment of water vapor sorption isotherm and permeability variation with ages. Construction and Building Materials, 83, 237-247.

ISO 10545-3. (2018). Part 3: Determination of Water Absorption, Apparent Porosity, Apparent Relative Density and Bulk Density.

ISO 11274. (1998). Soil quality - determination of the water retention characteristic — laboratory methods.

ISO 12571. (2021). Hygrothermal performance of building materials and products — determination of hygroscopic sorption properties.

ISO 12572. (2016). Hygrothermal performance of building materials and products — Determination of water vapour transmission properties — Cup method.

ISO 13788. (2012). Hygrothermal performance of building components and building elements — Internal surface temperature to avoid critical surface humidity and interstitial condensation — Calculation methods.

ISO 15148. (2002). Hygrothermal Performance of Building Materials and Products — Determination of Water Absorption Coefficient by Partial Immersion.

ISO 15901-1. (2016). Evaluation of Pore Size Distribution and Porosity of Solid Materials by Mercury Porosimetry and Gas Adsorption — Part 1, Mercury porosimetry.

ISO 15927-3. (2009). Hygrothermal performance of buildings-calculation and presentation of climatic data-Part 3: Calculation of a driving rain index for vertical surfaces from hourly wind and rain data.

ISO 5725-1. (2023). Accuracy (trueness and precision) of measurement methods and results — Part 1: General principles and definitions.

ISO 6946. (2017). Building components and building elements - Thermal resistance and thermal transmittance - Calculation methods.

ISO 8301. (1991). Thermal insulation - Determination of steady-state thermal resistance and related properties - Heat flow meter apparatus.

James, C., Simonson, C. J., Talukdar, P., & Roels, S. (2010). Numerical and experimental data set for benchmarking hygroscopic buffering models. International Journal of Heat and Mass Transfer, 53(19-20), 3638-3654.

Janssen, H., Blocken, B., & Carmeliet, J. (2007). Conservative modelling of the moisture and heat transfer in building components under atmospheric excitation. International Journal of Heat and Mass Transfer, 50(5-6), 1128-1140.

Janssen, H. (2011). Thermal diffusion of water vapour in porous materials: Fact or fiction? International Journal of Heat and Mass Transfer, 54(7-8), 1548-1562.

Janssen, H. and Carmeliet, J., (2015). Simulation of moisture and heat transfer in building components under atmospheric excitation: conservative modelling and numerical optimization. International Journal of Heat and Mass Transfer, 50, 1128–114.

Janssens, K., Feng, C., Marincioni, V., & Van Den Bossche, N. (2024). Comparison of different frost models with hygrothermal simulations to better understand frost damage in porous building materials. Building and Environment, 255, 111399.

Jerman, M., Palomar, I., Koci, V., & Cerny, R. (2019). Thermal and hygric properties of biomaterials suitable for interior thermal insulation systems in historical and traditional buildings. Building and Environment, 154, 81-88.

Kalamees, T. & Vinha, J. (2003). Hygrothermal calculations and laboratory tests on timber-framed wall structures. Building and Environment, 38(5), 689-697.

Karagiozis, A. (1993). Overview of the 2-D hygrothermal heat-moisture transport model LATENITE. Internal IRC/BPL Report.

Karagiozis, A., Hadjisophocleous, G., & Cao, S. (1997). Wind-driven rain distributions on two buildings. Journal of Wind Engineering and Industrial Aerodynamics, 67, 559-572.

Karagiozis, A. N. (2001). Advanced hygrothermal modeling of building materials using MOISTURE-EXPERT 1.0, In: Proceedings of the International Particleboard/Composite Materials Symposium, pp. 39-47.

Karagiozis, A. N., & Salonvaara, M. (1995). Influence of material properties on the hygrothermal performance of a high-rise residential wall (No. CONF-950104-). American Society of Heating, Refrigerating and Air-Conditioning Engineers, Inc., Atlanta, GA (United States).

Kennedy, H. E., & Owen, M. S. (2009). ASHRAE handbook: fundamentals. American Society of Heating, Refrigeration, and Air-Conditioning Engineers.

Kießl, K. (1983). Kapillarer und Dampfformiger Feuchtetransport in Mehrschichtigen Bauteilen, PhD Thesis, Universitat-Gesamthochschule Essen, 1983. (In German).

Kumaran, M. K., Mitalas, G. P., & Bomberg, M. T. (1994). Fundamentals of transport and storage of moisture in building materials and components. Moisture Control in Buildings, 18, 3-17.

Kumaran, K. (1996). Heat, air and moisture transfer through new and retrofitted insulated envelope parts. Final report volume 3 task 3: Material properties. IEA-Annex 24 HAMTIE.

Künzel, H. M. (1995). Simultaneous heat and moisture transport in building components: one and two-dimensional calculation using simple parameters, PhD Thesis, Institute of Building Physics, Germany.

Künzel, H.M., & Kiessl K. (1996). Drying of brick walls after impregnation. Bauinstandsetzen, 2, 87-100. (In German).

Künzel, H. M. (2000). Moisture risk assessment of roof constructions by computer simulation in comparison to the standard Glaser-method, International Building Physics Conference, Eindhoven, the Netherlands.

Künzel, H. M., & Karagiozis, A. (2010). Hygrothermal behaviour and simulation in buildings. In Materials for energy efficiency and thermal comfort in buildings. Woodhead Publishing. 54-76.

Langmans, J., Klein, R., & Roels, S. (2012). Hygrothermal risks of using exterior air barrier systems for highly insulated light weight walls: A laboratory investigation. Building and Environment, 56, 192-202.

Lelievre, D., Colinart, T., & Glouannec, P. (2014). Hygrothermal behavior of bio-based building materials including hysteresis effects: experimental and numerical analyses. Energy and Buildings, 84, 617-627.

Lewis, W. K. (1922). The evaporation of a liquid into a gas. Journal of Fluids Engineering, 44, 325-332.

López, O., Torres, I., Guimarães, A. S., Delgado, J. M. P. Q., & de Freitas, V. P. (2017). Inter-laboratory variability results of porous building materials hygrothermal properties. Construction and Building Materials, 156, 412-423.

Lu, B., Fang, J., Li, Y., Zhang, H., Gao, Y., & Feng, C. (2023). Accuracy of semi-empirical models for wind-driven rain using different data processing methods for wind velocity and direction. Building and Environment, 237, 110300.

Luikov, A. V. (1964). Heat and mass transfer in capillary-porous bodies. Advances in Heat Transfer, 1(1), 123-184.

Marincioni, V., Marra, G., & Altamirano-Medina, H. (2018). Development of predictive models for the probabilistic moisture risk assessment of internal wall insulation. Building and Environment, 137, 257-267.

Marincioni, V., Janssens, K., & Cambray, T. (2025). Moisture properties of insulation materials and their applicability to traditional construction. Sustainable Traditional Building Alliance.

Materialdatensammlung für die energetische Altbausanierung. https://www.masea-ensan.de. (In German).

Matsumoto, M. (1978). Simultaneous Heat and Moisture Transfer and Moisture Accumulation in Buildings, PhD Thesis, Kyoto University. (In Japanese).

McClung, R., Ge, H., Straube, J., & Wang, J. (2014). Hygrothermal performance of cross-laminated timber wall assemblies with built-in moisture: field measurements and simulations. Building and Environment, 71, 95-110.

Mendes N., Oliveira R., Henrique dos Santos G., (2003), Domus 2.0: a whole-building simulation program, in: Proceedings of the Eighth International IBPSA Conference, 863–870.

Mendes, N., Ridley, I., Lamberts, R., Philippi, P. C., & Budag, K. (1999). UMIDUS: a PC program for the prediction of heat and moisture transfer in porous building elements. In Building Simulation Conference–IBPSA, Vol. 99, 277-283.

Nicolai, A. & Grunewald, J. (2006). User Manual and Program Reference – DELPHIN 5. https://bauklimatik-dresden.de/delphin/2nd/doc/DELPHIN5-Tutorial_1_en.pdf.

Nicolai, A, Grunewald, J., & Zhang, J. S. (2007). Recent improvements in HAM simulation tools: Delphin 5 / CHAMPS-BES. In: Conference Proceedings of 12th Symposium of Building Physics.

Nofal, M., Straver, M., & Kumaran, K. (2001). Comparison of four hygrothermal models in terms of long-term performance assessment of wood-frame constructions. In: Proceedings of the 8th conference of Canadian building science solutions to moisture problems in building enclosures, Toronto, Canada, pp. 118-138.

Oswin, C. R. (1946). The kinetics of package life. III. The isotherm. Journal of the Society of Chemical Industry, 65(12), 419-421.

Outputs in DELPHIN 6.1. https://www.bauklimatik-dresden.de/delphin/2nd/doc/DELPHIN6_Outputs/Tutorial_4_D6_Outputs_en.html.

Panico, S., Larcher, M., Marincioni, V., Troi, A., Baglivo, C., & Congedo, P. M. (2023). Identifying key parameters through a sensitivity analysis for realistic hygrothermal simulations at wall level supported by monitored data. Building and Environment, 229, 109969.

Pedersen, C.R. (1990). Combined Heat and Moisture Transfer in Building Constructions, PhD Thesis, Technical University of Denmark, Denmark.

Pedersen, C. R. (1992). Prediction of moisture transfer in building constructions. Building and Environment, 27(3), 387-397.

Peleg, M. (1993). Assessment of a semi-empirical four parameter general model for sigmoid moisture sorption isotherms 1. Journal of Food Process Engineering, 16(1), 21-37.

Philip, J. R., & Devries, D. A. (1957). Moisture movement in porous materials under temperature gradient. Eos Transactions American Geophysical Union, 38(2), 222-232.

Panico, S., Larcher, M., Marincioni, V., Troi, A., Baglivo, C., & Congedo, P. M. (2023). Identifying key parameters through a sensitivity analysis for realistic hygrothermal simulations at wall level supported by monitored data. Building and Environment, 229, 109969.

Paolo, B., Roberta, P., & Alessandro, P. (2013). Simulazione energetica degli edifici esistenti: guida alla definizione di modelli calibrati. EPC srl. https://www.epc.it/Prodotto/Editoria/Libri/libro-Simulazione-energetica-degli-edifici-esistenti/2003. (In Italian).

Qin, M., Belarbi, R., Aït-Mokhtar, A., & Nilsson, L. O. (2009). Coupled heat and moisture transfer in multi-layer building materials. Construction and building materials, 23(2), 967-975.

Qin, M., Aït-Mokhtar, A., & Belarbi, R. (2010). Two-dimensional hygrothermal transfer in porous building materials. Applied Thermal Engineering, 30(16), 2555-2562.

Ramos, N. M, João Quesado Delgado, Barreira, E., & Freitas, V. P. D. (2009). Hygrothermal properties applied in numerical simulation: interstitial condensation analysis. Journal of Building Appraisal, 5(2), 161-170.

Rafidiarison, H., Remond, R., & Mougel, E. (2015). Dataset for validating 1-D heat and mass transfer models within building walls with hygroscopic materials. Building and Environment, 89, 356-368.

Ren, P., Feng, C., & Janssen, H. (2019). Hygric properties of porous building materials (V): Comparison of different methods to determine moisture diffusivity. Building and Environment, 164, 106344.

Reuge, N., Collet, F., Pretot, S., Moisette, S., Bart, M., Style, O., Shea, A. & Lanos, C. (2020). Hygrothermal effects and moisture kinetics in a bio-based multilayered wall: Experimental and numerical studies. Construction and Building Materials, 240, 117928.

Rode, C., Stang, B. D., & Hansen, M. H. (2006). Model for multidimensional heat, air and moisture conditions in building envelope components. Project description, Department of Civil Engineering, Technical University of Denmark, Denmark.

Roels, S., Depraetere, W., Carmeliet, J., & Hens, H. (1999). Simulating non-isothermal water vapour transfer: an experimental validation on multi-layered building components. Journal of Thermal Envelope and Building Science, 23(1), 17-40.

Roels, S. (2000). Modelling unsaturated moisture transport in heterogeneous limestone, PhD Thesis, KU Leuven.

Roels, S., Carmeliet, J., & Hens, H. (2003). HAMSTAD WP1: Final report–Moisture transfer properties and materials characterization. Laboratory of Building Physics, KU Leuven.

Roels, S., Carmeliet, J., Hens, H., Adan, O., Brocken, H., Cerny, R., Pavlik, Z., Hall, C., Kumaran, K., Pel, L., & Plagge, R. (2004). Interlaboratory comparison of hygric properties of porous building materials. Journal of thermal envelope and building science, 27(4), 307-325.

Roels, S., & Carmeliet, J. (2006). Analysis of moisture flow in porous materials using microfocus X-ray radiography. International Journal of Heat and Mass Transfer, 49(25-26), 4762-4772.

Roels, S., Talukdar, P., James, C., Simonson, C. J. (2010). Reliability of material data measurements for hygroscopic buffering. International Journal of Heat and Mass Transfer, 53 (23-24), 5355-5363.

Rouquerol, J., Rouquerol, F., & Sing, K. S. (1998). Adsorption by Powders and Porous Solids: Principles, Methodology and Applications. Elsevier.

Salonvaara, M., & Karagiozis, A. (1994). Moisture transport in building envelopes using an approximate factorization solution method. CFD Society of Canada, Toronto, June 1-3.

Salonvaara, M., Karagiozis, A., & Holm, A. (2001). Stochastic building envelope modeling—the influence of material properties. Thermal Performance of Exterior Envelopes of Whole Buildings VIII, 2-8.

Salonvaara, M., Boudreaux, P., Desjarlais, A., Antretter, F., & Werling, E. (2020). Validation of Hygrothermal Simulations with Wall Performance Experiments in an Environmental Chamber. In: E3S Web of Conferences, Vol. 172, p. 04010.

Sassi, S., Ge H., & Horvat M. (2013). Validating of wind-driven rain modules for HAM Tools. Proceedings of Thermal Performance of the Exterior Envelopes of Buildings XII, ASHRAE, Florida, pp. 1-9.

Schroderus, S., Lähteenmäki, V. M., Haapala, A., & Fedorik, F. (2022). Validation of Hygrothermal Numerical Simulation with Experiment for Future Climate Control. Scandinavian Simulation Society, 156-162.

Sedlbauer K. (2001). Prediction of mould fungus formation on the surface of/and inside building components, PhD Thesis, University Stuttgart.

Sontag, L., Nicolai, A., & Vogelsang, S. (2013). Validierung der Solverimplementierung des hygrothermischen Simulationsprogramms DELPHIN. Available at http://nbn-resolving.de/urn:nbn:de:bsz:14-qucosa-128968. (In German).

Souri, F., Ge, H., & Stathopoulos, T. (2021). Wind-driven rain on buildings: Accuracy of the ISO semi-empirical model. Journal of Wind Engineering and Industrial Aerodynamics, 212, 104606.

Steeman, M., Van Belleghem, M., De Paepe, M., & Janssens, A. (2010). Experimental validation and sensitivity analysis of a coupled BES–HAM model. Building and Environment, 45(10), 2202-2217.

Steskens, P. W., Janssen, H., & Rode, C. (2009). Influence of the convective surface transfer coefficients on the heat, air, and moisture (HAM) building performance. Indoor and Built Environment, 18(3), 245-256.

Straube, J., & Burnett, E. (1999). Review of modeling methods for building enclosure design. University of Waterloo.

Straube, J. F., & Burnett, E. F. P. (2000). Simplified prediction of driving rain on buildings. In: Proceedings of the international building physics conference, Eindhoven University of Technology Eindhoven, the Netherlands, Vol. 18, No. 21.09.

Straube, J., & Burnett, E. (2001). Overview of hygrothermal (HAM) analysis methods. Moisture analysis and condensation control in building envelopes, 81-89.

Talukdar, P., Olutmayin, S. O., Osanyintola, O. F., & Simonson, C. J. (2007a). An experimental data set for benchmarking 1-D, transient heat and moisture transfer models of hygroscopic building materials. Part I: Experimental facility and material property data. International journal of heat and mass transfer, 50(23-24), 4527-4539.

Talukdar, P., Olutmayin, S. O., Osanyintola, O. F., & Simonson, C. J. (2007b). An experimental data set for benchmarking 1-D, transient heat and moisture transfer models of porous building materials – Part II: experimental, numerical and analytical data. International Journal of Heat and Mass Transfer, 50(23-24), 4915–4926.

Tijskens, A., Roels, S., & Janssen, H. (2019). Neural networks for metamodelling the hygrothermal behaviour of building components. Building and Environment, 162, 106282.

Vandemeulebroucke, I., Kotova, L., Caluwaerts, S., & Van Den Bossche, N. (2023). Degradation of brick masonry walls in Europe and the Mediterranean: Advantages of a response-based analysis to study climate change. Building and Environment, 230, 109963.

Vandemeulebroucke, I., Kotova, L., Caluwaerts, S., & Van Den Bossche, N. (2024). Impact of climate change on degradation risks in solid masonry walls: Uncertainty assessment using a multi-model ensemble. Building and Environment, 264, 111910.

Van Belleghem, M., Steeman, M., Willockx, A., Janssens, A., & De Paepe, M. (2011). Benchmark experiments for moisture transfer modelling in air and porous materials. Building and Environment, 46(4), 884-898.

Van den Berg, C., & Bruin, S. (1978). Water activity and its estimation in food systems. In Proceedings Int. Symp. Properties of Water in Relation to Food Quality and Stability, Osaka, 1978.

Van De Walle, W. (2019). Prediction of the effective thermal conductivity of porous building blocks based on their pore structure, PhD Thesis, KU Leuven, Belgium.

Van Genuchten, M. T. (1980). A closed-form equation for predicting the hydraulic conductivity of unsaturated soils. Soil science society of America journal, 44(5), 892-898.

Van Marcke, P., Verleye, B., Carmeliet, J., Roose, D., & Swennen, R. (2010). An improved pore network model for the computation of the saturated permeability of porous rock. Transport in Porous Media, 85, 451-476.

Van Mook, F. J. (1999). Full-scale measurements and numeric simulations of driving rain on a building. In Proceeding 10th International Conference on Wind Engineering, 1145-1152.

Van Mook, F. J. (2002). Research on wind, rain and driving rain at the TUE site, during 1996-2000, http://fabien.galerio.org/drivingrain.

Van Mook, F. J. (2003). Driving rain on building envelopes. PhD Thesis, Technische Universiteit Eindhoven, the Netherlands.

Van Schijndel, J., Goesten, S., & Schellen, H. L. (2016). HAMSTAD Benchmarks using Comsol revisited. Presented at the 2016 COMSOL Conference in Munich, Munich, Germany.

Van Schijndel, A. W. M., Goesten, S., & Schellen, H. L. (2017). Simulating the complete HAMSTAD benchmark using a single model implemented in Comsol. Energy Procedia, 132, 429-434.

VDI Guideline 3789. (1999). Part 2: Environmental Meteorology - Interactions between Atmosphere and Surfaces. Beuth, Berlin.

Vereecken, E., & Roels, S. (2012). Review of mould prediction models and their influence on mould risk evaluation. Building and Environment, 51, 296-310.

Vereecken, E., & Roels, S. (2013). Hygric performance of a massive masonry wall: How do the mortar joints influence the moisture flux? Construction and Building Materials, 41, 697-707.

Vereecken, E., & Roels, S. (2019). Wooden beam ends in combination with interior insulation: An experimental study on the impact of convective moisture transport. Building and Environment, 148, 524-534.

Vereecken, E., Deckers, D., Janssen, H., & Roels, S. (2020). Field study on hydrophobised internally insulated masonry walls. DBMC 2020, Barcelona, 1-8.

Vereecken, E., & Roels, S. (2021a). Internally insulated walls with embedded wooden beams: how does hydrophobisation change the hygric performance? In: 1st International Conference on Moisture in Buildings 2021, Online.

Vereecken, E., & Roels, S. (2021b). Hygrothermal performance of internally insulated masonry walls with embedded wooden beam heads: A field study on the impact of hydrophobisation. Journal of Physics: Conference Series, 2069(1), 012019.

Visual crossing. https://www.visualcrossing.com/weather-data.

Vogelsang, S., Fechner, H., & Nicolai, A. (2013). Delphin 6 Material File Specification: Version 6.0; Technical Report. Technische Universität Dresden, Fakultät Architektur, Institut für Bauklimatik, Professur für Bauphysik.

Wolter, B., & Krus, M. (2005). Moisture measuring with nuclear magnetic resonance (NMR). In Electromagnetic Aquametry: Electromagnetic Wave Interaction with Water and Moist Substances (pp. 491-515). Berlin, Heidelberg: Springer Berlin Heidelberg.

WUFI. https://wufi.de/en/software/wufi-pro.

WUFI. (2015). Benchmark test of EN 15026. WUFI passes benchmark test of EN 15026. Available at https://wufi.de/en/wp-content/uploads/sites/11/2015/04/WUFI-Pro-Benchmarktest-EN15026_en.pdf.

WUFI forum1. Liquid transport coefficient. https://www.wufi-forum.com/viewtopic.php?f=32&t=1923&p=5654&hilit=resistance+factor#p5654.

WUFI forum2. Moisture Storage Function - 3 point formula. https://www.wufi-forum.com/viewtopic.php?t=1980.

Wufi-Wiki1. Details: Liquid Transport Coefficients. https://www.wufi-wiki.com/mediawiki/index.php/Details:LiquidTransportCoefficients.

Wufi-Wiki2. Details: Short Wave. https://www.wufi-wiki.com/mediawiki/index.php/Details:ShortWave.

Xu, B., Cambray, T., Marincioni, V., & Mavrogianni, A. (2023). Exploring the variability of hygrothermal material properties in historic bricks in London. Journal of Physics: Conference, 2654(1), 012085.

Yamamoto, H., & Takada, S. (2022). Influence of variability in hygrothermal properties on analytical results of simultaneous heat and moisture transfer in porous materials. Journal of building physics, 45(6), 757-773.

Zhang, X., Zillig, W., Künzel, Hartwig M., Mitterer, C., & Zhang, X. (2016). Combined effects of sorption hysteresis and its temperature dependency on wood materials and building enclosures – part Ⅰ: measurements for model validation. Building and Environment, 106, 143-154.

Zhao, J., Plagge, R., Nicolai, A., Grunewald, J., & Zhang, J. S. (2011). Stochastic study of hygrothermal performance of a wall assembly—The influence of material properties and boundary coefficients. HVAC&R Research, 17(4), 591-601.

Zhou, X., Carmeliet, J., & Derome, D. (2021). Assessment of moisture risk of wooden beam embedded in internally insulated masonry walls with 2D and 3D models. Building and Environment, 193, 107460.

Zhou, X., Desmarais, G., Carl, S., Mannes, D., Derome, D., & Carmeliet, J. (2022). Investigation of coupled vapor and heat transport in hygroscopic material during adsorption and desorption. Building and Environment, 214.

Zhou, X., Kubilay, A., Derome, D., & Carmeliet, J. (2023). Comparison of wind-driven rain load on building facades in the urban environment and open field: A case study on two buildings in Zurich, Switzerland. Building and Environment, 233, 110038.

Zhu, Z., Li, Y., Hu, P., Janssen, H., & Feng, C. (2025). Hygric properties of porous building materials (IX): Experimental evaluation of two hysteresis models. Building and Environment, 272, 112695.

Acknowledgement

My doctoral journey has flown by, marked by challenges and progress. Throughout this deeply rewarding experience, many people and moments deserve my greatest appreciation.

I am deeply grateful to my supervisor, Prof. Staf Roels, for his valuable guidance and support throughout my PhD journey. *Our first meeting at the CESBP2019 sparked my interest in hygrothermal modeling and heritage conservation. Your pragmatic advice shaped my initial ideas into a coherent research proposal. Your optimism, especially during the COVID-19 lockdown, offered both reassurance and motivation, while our online discussions ultimately opened the door to this PhD opportunity. When welcoming me into the lab to introducing me to colleagues, your mentorship has been marked by patience, clarity and generosity. Rather than providing ready-made answers, you encouraged me to think critically, understand logic and grasp fundamental principles. Your continuous, timely guidance and ability to connect me with the right people and resources were crucial in overcoming challenges and refining my research direction. I also greatly admire your capability to integrate the roles of researcher, architect, engineer and artist, excelling in each*.

I am profoundly grateful to my co-supervisor, Prof. Hans Janssen for his essential guidance in the past four years. *Our first meeting also at the CESBP2019 left a lasting impression: your sharp intellect, rapid speech and insightful perspectives immediately caught my attention. You can always explain complex ideas clearly and foresee potential challenges. Your detailed annotations on my manuscripts, whether concerning research content, narrative structure or language expression, have been instrumental in shaping my academic work. I deeply admire your unwavering commitment to scientific evidence, which have taught me the significance of questioning authority, challenging assumptions and maintaining a critical perspective in research*.

I am truly grateful to Prof. Shuichi Hokoi for his great support throughout my academic journey. *As my master's supervisor, your recommendation was essential to launching my PhD project. As an assessor in my supervisory committee, you have been closely witnessing the evolution of my research. Although we have not been able to meet in person for many years, each email exchange carries a*

familiar warmth, as if we were speaking face to face. Your prompt responses serve as a constant reminder of dedication and mentorship.

I am sincerely grateful to Prof. Evy Vereecken, whose work shaped my academic path even before we met. *Your highly cited review article on mold growth in building components was a key reference for my master's thesis. During my PhD, you have conveyed complex ideas with clarity, whether analyzing monitoring data or explaining research principles. I have also greatly benefited from your insights into career development*.

I would also like to thank all the members of my supervisory and examination committees. Prof. Özlem Cizer offered guidance and encouragement during the annual evaluations, supporting both my research direction and confidence throughout the process. Prof. Martin Tenpierik shared thoughtful advice that helped improve my thesis. Prof. Krista De Jonge kindly coordinated the defense process and ensured that everything ran smoothly.

I am indebted to Prof. Chi Feng for generously sharing his expertise in hygrothermal modeling and experiments. I also thank Jimmy Van Criekingen and Patricia Elsen for their valuable support with experimental and other technical tasks. Their dedication and skills greatly facilitated the acquisition of material properties and hygrothermal responses.

I am immensely grateful to all the contributors from 19 countries who participated in the round robin validation project. Your engagement and feedback made this initiative one of the most collaborative efforts in hygrothermal research and a significant cornerstone of my PhD. I also greatly appreciate the interactions with the UK Centre for Moisture in Buildings (UKCMB), the International Council for Research and Innovation in Building and Construction (CIB) and other global researchers and practitioners passionate about hygrothermal modeling. A special mention goes to Dr. Anssi Laukkarinen, Bruno Vanderschelden, Prof. Carsten Rode, Changchang Xia, Dr. Huarong Xie, Prof. Kazuma Fukui, Dr. Lin Wang, Dr. Michele Bianchi Janetti, Dr. Paul Klõšeiko, Prof. Riccardo Paolini, Prof. Valentina Marincioni and Dr. Villu Kukk, whose insights have greatly contributed to my exploration.

Furthermore, I appreciate my colleagues in the Section of Building Physics and Sustainable Design. Chengnan Shi, Minting Chen, Dr. Daan Deckers and Laura Peeters, working in closely related areas, offered different emphases and methodological perspectives that inspired me. Dr. Arash Erfani Beyzaee and Tohid Jafarinejad provided valuable assistance with building simulation coursework, while Prof. Dirk Saelens attested to my successful completion of this course. Tim Verhetsel contributed to the graphical illustration of our paper,

which was later chosen as the cover image for the Journal of Building Simulation. Thanks to Dr. Marcin Zygmunt, Dr. Katia Ritoša, and Dr. Sara Willems for their helpful advice on doctoral training and postdoc applications. My "roommates", Maria Lackovicova, Lisi Freitas Camboim, Yuanlu Li, Marta Galindo Díaz and Vincent Crevals, kept me motivated with daily greetings. I also acknowledge Prof. Bert Blocken, Prof. Filip Descamps and former colleagues, Prof. Rui Guo, Dr. Jo-Hendrik Thysen, Prof. Jason Zhang, Dr. Geert Bauwens and Dr. Astrid Tijskens, for the insights and inspiration drawn from their work and interactions. Last but not least, I am truly grateful to Christa Devroey for her care and support, making my staying in Leuven significantly smoother.

My appreciation goes to the WUFI team — Dr. Thomas Schmidt, Dr. Christian Bludau, Dr. Daniel Zirkelbach and Dr. Hartwig Künzel — and the DELPHIN team — Dr. Heiko Fechner and Prof. John Grunewald — for indispensable guidance in navigating their software. Heartfelt thanks to Dr. Fabien van Mook for generously sharing wind-driven rain datasets with clear explanations, Dr. Isabeau Vandemeulebroucke and Dr. Kaat Janssens for their expertise in parametric analysis, Dr. Xiangnan Yu for his insightful perspectives on machine learning applications, Dr. Robyn Pender for her practical insights on building pathology, Dr. Guangqi An for her guidance in statistical analysis, and Hao Jiang and Shuangzhuang Li for their insights on artificial intelligence applications, and Yiming Zhang, Prof. Junsheng Huang, Dr. Yiping Zhang and Hang Wang for generously sharing their experiences in academic career development.

I sincerely appreciate the China Scholarship Council (CSC) for funding my PhD scholarship, as well as Fonds Wetenschappelijk Onderzoek (FWO) for the travel grant that enabled me to attend IBPC2024.

I am also deeply grateful to KU Leuven for its valuable academic resources, including the Renovation of Structures course taught by Prof. Koen van Balen and Prof. Els Verstrynge, as well as other lectures, workshops and seminars that broadened my research interests and perspectives. I also benefited from academic activities beyond KU Leuven, particularly NSB2023 organized by Aalborg University, ICMB2023 organized by University College London and UKCMB, IBPC2024 hosted by Toronto Metropolitan University, CESBP25 organized by Budapest University of Technology and Economics, and the Heritage Science Summer School organized by Prof. Tim De Kock. I sincerely thank all those who kindly hosted me during academic visits, including Prof. Chris Whitman at Cardiff University; Binyu Xu at University College London; Robin Hilbrecht and Krista Rowan at Carleton University; Prof. Hua Ge, Jing Li, Sina Akhavan Shams, Himanshu Sharma and Dr. Payam Gholamalipour at

Concordia University; Prof. Shady Attia at the University of Liège; and Ruben Van den Bossche and Xiaolin Chen at Ghent University.

Beyond academia, I will forever cherish the support from my parents and family, whose belief in me has profoundly shaped my resilience throughout my life. To my dearest friends, near or far, your passion, kindness and support have not only inspired me but also reminded me that no challenge is faced alone. Though words may only scratch the surface of my gratitude, my appreciation is boundless. I look forward to expressing my thanks to each of you in person, as no written message can fully convey what I feel.

Lastly, I am grateful to the International Council on Monuments and Sites (ICOMOS), English Heritage, the Dutch Rembrandt Card and the Belgian Museum Pass for granting me access to countless historical sites and built heritage across Europe. These experiences not only deepened my understanding of the practical applications of my research but also enriched my personal well-being throughout my four-year stay.

As my PhD concludes, I return to the iconic words of Steve Jobs —

*Stay hungry, stay foolish***.**

More than a motto, they embody a way of life — one driven by curiosity, courage and resilience to embrace the unknown.

Heat and moisture are fundamental forces shaping both the natural and built environments, yet their interaction remains intricate and nuanced. Standing on the shoulders of giants, my research has taken a small step toward deepening our understanding of this dynamic. Science is never truly complete — assumptions invite reevaluation, mechanisms require refinement, and uncertainties remain worthy of exploration. I will continue questioning, striving and seeking knowledge as I have been doing. Moving forward with the same spirit: to learn as a beginner, to dream without hesitation, and to welcome new challenges with an open heart. Here's to whatever comes next.

Curriculum Vitae



Xinyuan Dang 党新元

Xinyuan is a researcher, architect, engineer and photographer. His academic work focuses on heat, air and moisture (HAM) modeling and hygrothermal behavior of buildings. He situates these technical subjects within a broader interdisciplinary framework, examining their relevance to heritage governance and conservation technologies, while addressing the challenges of environmental resilience. *Bridging building and science & framing the world with wonder* — As a photographer, Xinyuan captures the breath of buildings and the silence of landscapes, transforming physical dynamics into contemplative imagery that evokes the lived experience of space and time.

Basic information

Email: dangxinyuan1994@gmail.com
ORCID: orcid.org/0000-0002-0113-4962
LinkedIn: www.linkedin.com/in/xinyuan-dang-b83327249
Google scholar: scholar.google.com/citations?user=qjqh3dgAAAAJ
ResearchGate: www.researchgate.net/profile/Xinyuan-Dang

Education and work experience

2021-2025 PhD in Civil Engineering (Building Physics and Sustainable Design), KU Leuven, Leuven, Belgium

- **Supervisors**: Staf Roels & Hans Janssen
- **Topic**: Quality assessment of heat, air and moisture (HAM) models to predict the hygrothermal response of building components

2020-2021 Architect, Guangdong Architecture Design & Research Institute Co., Ltd, Guangzhou, China

2017-2020 MSc in Architecture (Building Technology Science), Southeast University, Nanjing, China

- **Supervisor**: Shuichi Hokoi
- **Topic:** Evaluation of mould growth risks due to air leakage through air cavity of building walls

2019-2019 Exchange student in Architecture (Building Environment Engineering), Kyoto University, Kyoto, Japan

- **Supervisor**: Ogura Daisuke

2013-2017 BSc in Civil Engineering, Hohai University, Nanjing, China

Academic and professional engagement

- **Member** of International Council for Research and Innovation in Building and Construction (CIB) and **member** of CIB Working Group 40 (W040): *Heat and Moisture Transfer in Buildings*
- **Member** of International Council on Monuments and Sites (ICOMOS) and **member** of ICOMOS Emerging Professional Working Group (EPWG)
- **Affiliate** of UK Centre for Moisture in Buildings (UKCMB) and **member** of UKCMB Technical Working Group 1 (TWG 1): *Monitoring and Modelling of Moisture in Buildings*
- **Member** of International Association of Building Physics (IABP), Europa Nostra, European Students' Association for Cultural Heritage (ESACH), YOuth in COnservation of CUltural heritage (YOCOCU), Architectural Society of China (ASC)

Research Interests

Heat, Air and Moisture (HAM) Modeling
Heritage Conservation Theories and Technologies
Heritage Governance Criticism
Sustainable and Healthy Built Environment

Selected peer-reviewed journal papers (published by Nov. 2025)

- **Dang, X.***, Hong, Q., Liu, W., & Wang, Y. (2025). China's heritage governance blueprint: Revisiting evolutionary trajectories, reframing institutional priorities and mapping the national registry. Habitat International, 165, 103541. https://doi.org/10.1016/j.habitatint.2025.103541.
- **Dang, X.***, Vereecken E., Janssen, H., Roels, S. (2025). Hygrothermal response of masonry facades with vapor-tight or capillary-active internal insulation under current and future climate scenarios. Built Heritage. 9, 23. https://doi.org/10.1186/s43238-025-00188-x.

- **Dang, X.***, Guimarães, A. S., Sarkany, A., Laukkarinen, A., Xu, B., Vanderschelden, B., Rode, C., Xia, C., Feng, C., Whitman, C., Deckers, D., Yang, H., Fechner, H., Sharma, H., Ge, H., Xie, H., Zhang, H., Vandemeulebroucke, I., Mazura, J., Xie, J., Madera, J., Grunewald, J., Vinha, J., Janssens, K., Fukui, K., Mourkos, K., Wang, L., Bart, M., Morelli, M., Tenpierik, M., Abuku, M., Defo, M., Janetti, M. B., Klõšeiko, P., Sekki, P., Kopecký, P., Matiasovsky, P., Paolini, R., Slávik, R., Cerny, R., Akhavan Shams, S., Moissette, S., Kalamees, T., Freitas, T. S., Colinart, T., Bednar, T., Bunch-Nielsen, T., Koci, V., Marincioni, V., Kukk, V., Gan, W., Chen, X., Hu, X., Plantec, Y., Xie, Y., Huijbregts, Z., Janssen, H., Roels, S. (2025). A state-of-the-art empirical round robin validation of heat, air and moisture (HAM) models. Building and Environment. 276, 112867. https://doi.org/10.1016/j.buildenv.2025.112867.
- **Dang, X.***, Janssen, H., & Roels, S. (2024). A comprehensive benchmark dataset for the validation of building component heat, air, and moisture (HAM) models. Building Simulation, 17, 1893-1907. https://doi.org/10.1007/s12273-024-1176-8.
- **Dang, X.***, Vereecken, E., Janssen, H., & Roels, S. (2024). Impact of semi-empirical methods implemented in heat, air, and moisture (HAM) models on predicted wind-driven rain (WDR) loads and hygrothermal responses. Building and Environment, 262, 111770. https://doi.org/10.1016/j.buildenv.2024.111770.
- **Dang, X.***, Liu, W., Hong, Q., Wang, Y., & Chen, X. (2023). Digital twin applications on cultural world heritage sites in China: A state-of-the-art overview. Journal of Cultural Heritage, 64, 228-243. https://doi.org/10.1016/j.culher.2023.10.005.
- Li, Y., **Dang, X.**, Xia, C., Ma, Y., Ogura, D., & Hokoi, S.* (2020). The effect of air leakage through the air cavities of building walls on mold growth risks. Energies, 13(5), 1177. https://doi.org/10.3390/en13051177.
- Li, Y.*, Wu, R., Xie, H., Zhao, G., **Dang, X.**, & Hokoi, S. (2020). Water film in very high humidity inhibits mold growth on the damp surface of soil ruins. Building and Environment, 181, 107073. https://doi.org/10.1016/j.buildenv.2020.107073.

Selected peer-reviewed conference papers (published by Nov. 2025)

- **Dang, X.***, Janssen, H., Roels, S. (2025). User impact as an uncertainty in hygrothermal simulations: insights from a round robin test. In: Berardi, U. (eds) Multiphysics and Multiscale Building Physics. IABP 2024. Lecture Notes in Civil Engineering, 552 (1), 68-75. Springer, Singapore. https://doi.org/10.1007/978-981-97-8305-2_9. (IBPC2024, Toronto).

- **Dang, X.***, Janssen, H., & Roels, S. (2023). Hygrothermal Modelling of one-dimensional Wall Assemblies: inter-model Validation between WUFI and DELPHIN. Journal of Physics: Conference Series, 2654(1), 012040. https://doi.org/10.1088/1742-6596/2654/1/012040. (NSB2023, Aalborg).
- **Dang, X.***, Janssen, H., Roels, S. (2023). Comparative simulations on hygrothermal performance of calcium silicate and wood fiber as capillary active internal insulation materials. ScienceOpen. https://doi.org/10.14293/ICMB230020. (ICMB 2023, London).
- Li, Y.*, Zhang, W., Wu, R., **Dang, X.**, & Hokoi, S. (2020). High air relative humidity and lighting modes govern mould growths on damp soil ruins' surface in high-humidity regions. E3S Web of Conferences, 172, 23010. EDP Sciences. http://doi.org/10.1051/e3sconf/202017223010. (NSB2020, Tallinn).
- **Dang, X.**, Hokoi, S., Li, Y., Xia, C., & Yan, M. (2019). Evaluation of mould growth risks due to air leakage through air cavity of the building walls. MATEC Web of Conferences, 282, 02060. https://doi.org/10.1051/matecconf/201928202060. (CESBP2019, Prague).

Author Declarations

Declaration of use of generative AI

I did not use generative AI assistance tools during the research/writing process of my thesis, except for mere language assistance. The text/code/ images in this thesis are my own (unless otherwise specified) and generative AI has only been used in accordance with the KU Leuven guidelines and appropriate references have been added. I have reviewed and edited the content as needed and I take full responsibility for the content of the thesis.

Cite this thesis

Dang, X. (2025). Quality Assessment of Heat, Air and Moisture (HAM) Models to Predict the Hygrothermal Response of Building Components, PhD Thesis, Section of Building Physics and Sustainable Design, Department of Civil Engineering, KU Leuven, Belgium.

(*The overall PhD research profile and full text of this thesis is available at: https://www.kuleuven.be/doctoraatsverdediging/fiches/3E21/3E211019.htm*)

Declaration of research data management

The research data supporting this thesis are archived at the Section of Building Physics and Sustainable Design, Department of Civil Engineering, KU Leuven, under the following directory: J:\SET-BWK-BWF-DI0514\Pool-0001\Xinyuan Dang_PhD_Research Package. For access permissions, contact Patricia Elsen (patricia.elsen@kuleuven.be). For dataset content or structure inquiries, contact Xinyuan Dang (dangxinyuan1994@gmail.com).